DISS. ETH NO. 24258

ENGINEERING NONLINEARITY IN LOW-DIMENSIONAL SYSTEMS FOR ENERGY CONVERSION

A thesis submitted to attain the degree of

DOCTOR OF SCIENCES of ETH ZURICH

(Dr. sc. ETH Zurich)

presented by

MARC SERRA GARCIA

Máster Universitario en Nanotecnologia, Universitat Autónoma de Barcelona

born on *27.04.1987*

citizen of Spain

accepted on the recommendation of

Prof. Dr. Chiara Daraio, ETH Zürich
Prof. Dr. Raffaelo D'Andrea, ETH Zurich

2017

2017

Abstract

Energy converting devices are limited by the properties of available constituent materials. For example, the working fluid in a thermal engine determines its range of operational temperatures, or the choice of semiconductor material constrains a photovoltaic panel's efficiency. A recent trend in materials' science seeks to overcome these limitations by developing structured materials that achieve properties exceeding those of conventional materials. This approach has led to the invention of metamaterials, and resulted in devices capable of surpassing fundamental limits, for example focusing waves in a sub-wavelength region. Until now, most of the work in metamaterials has focused on exploiting linear phenomena, for example to open band-gaps, focus or cloak waves. This thesis pursues a fundamental understanding of nonlinear energy conversion processes in artificial lattices. The first part of the work investigates the effect of driven, localized modes on the quasi-static mechanical properties of a material. It demonstrates that an external energy input can be used to tune a material's differential stiffness over an extreme range including negative and infinite values. The thesis proceeds with the investigation of lattices containing multiple interacting modes. These lattices are shown to act as purely mechanical analogs of optomechanical systems. They are capable of converting mechanical energy into a harmonic motion with a tunable frequency and phase. Phase tunability is a particularly relevant for technological applications because it enables devices that combine energy from multiple sources and avoid destructive interference effects. This thesis continues by investigating energy-converting systems under stochastic excitation. In this regime, mechanical quantities have thermodynamic interpretation, and the system under study behaves as a stochastic heat engine *i.e.* a low-dimensional equivalent of a conventional thermal machine. The engine presents exotic phenomena such as negative thermal conductivity and nonpassive states of motion. The last part of the thesis introduces an algorithm to generate metamaterial geometries from discrete mass-spring systems. While this algorithm is currently limited to linear systems, overcoming this limitation will enable the fabrication of energy converting metamaterials such as stochastic heat engines.

Abstract

I dispositivi di conversione dell'energia sono limitati dalle proprietà dei materiali che li costituiscono. Ad esempio, il fluido in un motore termico ne determina l'intervallo di temperature entro cui può operare, o la scelta di un particolare materiale semiconduttore vincola l'efficienza di un pannello fotovoltaico. Una recente tendenza nella scienza dei materiali cerca di superare queste limitazioni sviluppando materiali strutturati che raggiungono proprietà superiori a quelle dei materiali convenzionali. Questo approccio ha portato all'invenzione dei metamateriali e prodotto dispositivi in grado di superare limiti fondamentali, per esempio riuscendo a concentrare onde in un'area significativamente inferiore alla loro lunghezza d'onda. Fino ad ora la maggior parte del lavoro sui metamateriali si è concentrata sull'utilizzo di fenomeni lineari, ad esempio per aprire band-gap, per focalizzare onde o rendere oggetti invisibili a queste. Questa tesi persegue una comprensione di livello fondamentale dei processi non lineari di conversione dell'energia in cristalli artificiali. La prima parte di questo lavoro studia l'effetto dell'eccitazione di modi locali sulle proprietà meccaniche quasi statiche di un materiale. Si dimostra che un apporto di energia esterna può essere usato per regolare la rigidità differenziale di un materiale in una gamma estrema, che include valori negativi ed infiniti. Questa tesi procede con lo studio di cristalli che contengono molteplici modi interagenti. Questi cristalli vengono mostrati agire come analoghi puramente meccanici di sistemi optomeccanici. Essi sono in grado di convertire l'energia meccanica in un moto armonico con frequenza e fase a scelta. La possibilità di scelta della fase è particolarmente rilevante per le applicazioni tecnologiche, perché permette ai dispositivi che combinano energia da fonti multiple di evitare effetti di interferenza distruttiva. Questa tesi prosegue analizzando i sistemi di conversione di energia sotto eccitazione stocastica. In questo regime, le grandezze meccaniche hanno interpretazione termodinamica, e il sistema studiato si comporta come una macchina termica stocastica, equivalente a una macchina termica convenzionale ma con limitati gradi di libertà. La macchina presenta fenomeni esotici come una conducibilità termica negativa e una distribuzione di probabilità della velocità e della posizione che non massimizza l'entropia. L'ultima parte della tesi introduce un algoritmo per ottenere geometrie di metamateriali a partire da sistemi discreti massa-molla. Sebbene questo algoritmo sia attualmente limitato a soli sistemi lineari, superando in futuro questa

limitazione sarà possibile realizzare metamateriali per la conversione di energia che operino come macchine termiche stocastiche.

Acknowledgements

I would like to thank my advisor, Chiara Daraio, for giving me the opportunity to pursue a Ph.D. in one of the best schools in the world, being a student from an unknown university without an impressive publication record. During my time as a Ph.D. student I've had great scientific freedom and the best resources, and I'm immensely grateful for that. I would also like to thank my undergraduate advisor, Alvaro San Paulo, for taking me when I was a clueless undergraduate and teaching me the basics of scientific research; and for then generously supporting me when I left to pursue this opportunity abroad.

I would also like to acknowledge my scientific collaborators. I will never forget the exciting work with Katie Matlack, trying to build our topological insulator before anyone else; or the intense discussions with Joseph Lydon, to whom I feel I owe a lot of my scientific development; and the long afternoons with Miguel Molerón, fighting with the challenges of acousting lensing. I must also thank the staff at ETH Zurich, Ueli Marti, who patiently helped me debug and build my circuits, Jean-Claude Tomasina, who was of great help in designing and building all kinds of mechanical devices, to the people in administration at ETH and Caltech: Carolina, Lynn, Josain, Sarah and Sonya, and more generally to everyone who, in one way or another, makes ETH such an amazing place for scientific research.

I'm also very grateful to the Solitonk and TapTools team, for sharing with me the great learning experience of pursuing a startup company: Damien, Luca, Mythili, Clara and Tom. From doing sales pitches in Paris and Salzburg, industrializing the production of an electronic circuit or learning about patent law, this opportunity has added a completely new dimension to my Ph.D. studies, one that very few people get to experience. I'm also grateful to my Master and Bachelor students: Tom, Sven, David, Matthieu and Ferran. Mentoring them was a great experience, from which I've learned a lot.

I would also like to thank my parents, Francesc and Carme, who supported me unconditionally during my almost 30 years of education. And my roommates, Luca and Wei-Hsun; They have been amazing friends, always supportive, and a lot of fun to live with. To all my friends and

colleagues in the Daraio Lab: Ada, Andrea, Anton, Antonio, Bastian, Carly, Clara, CQ, Damien, Deva, Dominique, Eleftheria, Georgios, Georgios, Isotta, Ivan, Jan, Jinwoong, Katie, Kirsti, Luca, Marianna, Miguel, Mythili, Namiko, Osama, Raffaele, Sebastian, Terry, Tom, Vinnie and Wei-Hsun.

Special thanks must go to my friends in Zurich: to Miguel, for the good moments in the mountains and in the city, to Carly Donahue, for the good conversations and the great times sledding, hiking and travelling. To Luca, for being a great gym partner on top of a good friend and a great cook. To Katie, for bringing me to the best hikes and being a good friend all around, to Dominique, for being so patient and helpful and for the fun moments in Tromso and Rome, to Eleftheria and Stavros, for being great friends, to Ada Amendola, for being an amazing office mate and tour guide, to Wei-Hsun, for safely driving us around Greece, and to Vinnie, for being such a fun guy to be around. And also, my Caltech friends: Anton Toutov, a great Chemist and friend, Jessica “Bailarina” Gimbel, who I’ve met in the most interesting places: New York, Barcelona, Milan, Los Angeles. Kelly Kim, a great scientist and person and Pablo, Bastian, Frank, and Jesse, all amazing people. Finally, I must also thank those back home: Sergi, Sílvia, Emma and Núria, who stayed friends in spite of the distance.

Contents

List of figures

Introduction

Motivation and objectives

Virtually all modern technologies require energy in order to operate. In general, obtaining energy from available sources requires some type of conversion (for example, from light to electricity in a photovoltaic panel, or from heat to work in a heat engine) before the energy can be used. In spite of this ubiquity, energy conversion processes are not well understood in systems far from equilibrium[1], even in relatively simple cases such as sets of nonlinearly-interacting masses and springs. For these systems, an equilibrium or close-to-equilibrium description is available, but most interesting scenarios (e.g. living organisms, heat engines) involve out-of-equilibrium states for which a general theory is lacking. In this thesis, we investigate nonlinear systems with the goal of developing energy converting materials. We limit ourselves to systems using a low number of degrees of freedom. These systems provide a privileged look into the underlying physics: Due to their low dimensionality, they can be simulated in computers, and all of their degrees of freedom can be monitored experimentally in real time. The fact that we are now able to fabricate and simulate this class of systems has led to the emergence of stochastic thermodynamics. A novel field exploring the thermodynamics of highly fluctuating systems. This is in contrast with conventional thermodynamics, where systems contain an extremely large number of degrees of freedom, on the order of Avogadro's number, and therefore individual trajectories can neither be simulated nor measured experimentally.

The desire to understand energy conversion processes is motivated by pure scientific curiosity, but is also driven by practical applications: Energy converting devices are limited by the properties of the constituent materials. Following with the previous examples, a heat engine that exploits a phase transition will be limited to operate in the temperature region where the phase transition occurs, and a photovoltaic panel's absorption wavelength will be constrained by the bandgap of the semiconductor used. In conventional materials, these properties are typically bound in pre-defined intervals. For example, a material's density is

positive and finite, and so is its bulk modulus. Recently, a new approach has emerged which seeks to overcome these limitations by using a microscopic structure, resulting in so-called metamaterials. This microscopic structure allows the material to achieve extreme properties (e.g. negative effective mass[2]) or properties that do not appear together in conventional materials (e.g. simultaneously high stiffness and damping[3]). These novel properties arise from resonances and interactions in the internal structure, and can be used to realize high-performance devices such as lenses that are not limited by diffraction effects[4]. The metamaterial approach has found considerable successes in various applications, including focusing[4-7], cloaking[8-11] and stopping waves[2]. Metamaterials hold great promise for energy technologies, due to their ability to respond at frequencies not accessible to conventional materials[12] and due to metamaterial's ability to localize energy[13]. Inspired by these results, the low-dimensional models discussed in this thesis focus on energy conversion phenomena that arise due to the nonlinear interaction between a low number of modes of vibration inside a lattice.

Outline

The work in this thesis proceeds from simpler systems to more complex cases, starting with a single degree of freedom system subject to a harmonic drive and proceeding to a three degrees of freedom system under stochastic excitation. Here I provide a brief outline that highlights the logical progress connecting the papers that compose this cumulative thesis.

Chapter 2 starts by investigating the dynamics of an extended system, a granular chain, in which only a single mode of vibration is excited. The granular chain, a one-dimensional lattice of steel particles interacting though nonlinear Hertzian contacts, is chosen for its rich nonlinear dynamics (see[14] for an overview of granular phenomena), arising from the asymmetric Hertzian interaction, and the vast body of knowledge describing its properties. We explore, theoretically and experimentally, the system under quasi-static deformations, and determine the effect of the excitation on the mechanical properties of the lattice such as the stiffness and damping. As main conclusions, we determine that the excitation of a localized mode can result in changes in the force-displacement relation, including negative or

even infinite stiffness. When we subject the lattice to increasing levels of excitation, we observe a hysteretic force-displacement response. As a consequence of the hysteretic response in this regime, subjecting the lattice to a quasistatic deformation cycle requires the addition of external energy. The required energy can be controlled by modifying the lattice excitation, and for this reason we refer to this phenomenon as tunable damping.

Chapter 3's objective is to utilize the response of an excited lattice to transfer energy between two frequencies. This requires a phenomenon similar to the tunable damping described in Chapter 2, but with opposite sign (i.e. where a cyclic lattice deformation results in positive work done on the external force causing the deformation). Using the theoretical model devised in Chapter 2, the requisite property for such behavior is a dynamically hardening nonlinearity, i.e. one that satisfies ($d^3F/dx^3 < 0$). For this purpose, we select a magnet chain as the experimental system for Chapter 3. Due to differences between the magnetic force and the Hertzian contact law, the magnetic system exhibits the required type of nonlinear interaction. We experimentally demonstrate that this system is capable of converting energy between two frequencies, and build a reduced-order model capable of explaining the frequency conversion dynamics using two degrees of freedom. We identify a combination resonance as the energy converting mechanism, rather than a hysteretic force-displacement loop as found in Chapter 2. The combination resonance arises due to a feedback delay between the motion of the extended mode and the amplitude of the localized mode. We show that this system is a mechanical analog of an optomechanical system, and that is capable of producing signals with a tunable output frequency and phase, and to harvest energy from multiple frequency components and integrate it into a single output.

Chapter 4 seeks to investigate the dynamics of the reduced-order system from Chapter 3 under stochastic excitation. Stochastic excitations describe situations where the excitation function is not known. They represent most relevant applications of energy converting technology: Thermal agitation, the random vibrations of a machine or the electric field coming from a black-body source (such as the sun) are described by stochastic processes. We explore this phenomenon in a "toy-model" experimental system consisting of a set of strings and a cantilever, which presents the same type of nonlinear dynamics that describes the interaction between lattice modes in Chapter 3 (See Equation 6 and 7 in Chapter 3 and Eq.

1a-c in Chapter 4). The choice of a different experimental system is driven by the requirement of low mechanical loss, which is not met by the magnets setup of Chapter 3, which has a quality factor of approximately 10, but is met by the cantilever system (Which has a quality factor around 1000). Due to the use of a stochastic excitation, the physical magnitudes of the system have a thermodynamic interpretation. For example, the friction force can be interpreted as a heat flow out of the system. Using the definitions of heat and work from stochastic thermodynamics, we characterize the performance of the system and compare it to thermodynamic limits. We also show that the system presents exotic phenomena such as negative thermal conductivity[15] and nonpassive states of motion[16-18], states where the probability distribution of the system's variables (position and momentum) does not maximize the entropy for the given expected value of the energy.

Chapter 5 presents an algorithm to extract discrete mass-spring models from metamaterial designs, and to obtain metamaterial geometries that fit desired arbitrary discrete models. This represents a departure from previous chapters that focused on the energy conversion dynamics of low-dimensional models for discrete lattices. However, being able to obtain geometries from discrete models is an essential step towards the vision of creating materials with novel energy converting performances, since most studies on energy converting phenomena (including those in Chapters 2-4 of this thesis) are done in discrete models. The approach presented utilizes ideas from condensed-matter physics (Such as effective tight-binding models and the Schrieffer-Wolff transformation[19]). The design method is based in dividing the model into sub-spaces describing various aspects of the model (For example, the coupling stiffness between a unit cell and each neighbor are treated as belonging to different subspaces). This division, which is not exact but an approximation, allows us to perform an exhaustive search on each sub-space. The result from this approximate optimization is used as an initial guess for a gradient search that takes into account interferences between the different sub-spaces and produces an exact geometry. The potential of this approach is demonstrated by obtaining designs for acoustic lenses, zero group velocity materials and topological insulators. While the algorithm is currently limited to linear systems, the same design philosophy can be extended to nonlinear systems and should enable the design of novel energy converting metamaterials.

Significance of the work

This work discusses energy converting phenomena in low dimensional nonlinear systems. It shows that relatively simple mechanical systems can present nontrivial energy converting phenomena including tunable damping, frequency conversion, negative thermal conductivity and heat engine operation. The work also describes a method to translate discrete systems into metamaterial designs. Here I briefly discuss the significance of each publication in this thesis.

Chapter 2 demonstrates that driven nonlinear lattices can present highly tunable stiffness, reaching negative and infinite damping, in addition to zero frequency band gaps and tunable damping. In addition, it allows to selectively tune individual regions of the force-displacement relation of a material, by utilizing the two degrees of freedom provided by the excitation force's amplitude and frequency. Tuning a material's stiffness is a long-standing problem with various proposed solutions[20-22], and our work is, to the best of our knowledge, the first published mechanism that allows the introduction of stiffness changes at selectable points of the force-displacement relation. This can be used to create tunable devices that are able operate under different loads (for example, tunable vibration-mitigating materials that can block vibrations while holding arbitrary loads, which is not the case in alternative technologies such as those based on buckling[23]). The presence of zero-frequency band gaps is significant because it provides a means to block extremely low-frequency vibrations, which requires large masses when other technologies are used[24].

Chapter 3 demonstrates energy conversion in lattices with a tunable output frequency and phase. It is significant for two reasons: First, it provides a mechanism to generate signals with a selectable output phase, which can be used to create tunable phased arrays or to obtain energy from multiple sources while avoiding destructive interference. Second, it demonstrates a purely-mechanical analog of optomechanical systems[25, 26]. This is significant because it enables the translation of the vast knowledge regarding optomechanical interactions (For example, how to build optomechanical transistors[27] or heat engines[28]) into the mechanical domain.

Chapter 4 provides the first experimental demonstration of a mechanical autonomous stochastic heat engine. Stochastic heat engines have their origin in the classical problems of the Maxwell demon and the Feynman ratchet, but had only been demonstrated experimentally using non-autonomous systems that rely on external control loops to prescribe a thermodynamic cycle[29, 30]. This work shows, theoretically and experimentally, that autonomous heat engine operation can arise naturally in the presence of nonlinearly-interacting degrees of freedom in contact with thermal baths at different temperatures. From a fundamental point of view, having an experimental model of an autonomous stochastic heat engine is significant because it provides a test system for stochastic thermodynamics (Non-autonomous engines are not satisfactory models because the external control signal prescribes the output motion and therefore trivializes the calculation of the work). From an applied point of view, autonomous operation is a requirement. While stochastic heat engines produce extremely small power and therefore would not be usable unless they operate at extreme frequencies or are tightly integrated, any hypothetical future application must be autonomous, since non-autonomous engines consume vast amounts of power to operate the computers and lasers that prescribe the thermodynamic cycle, thereby consuming more energy than they produce.

Chapter 5, which presents a method to generate metamaterial geometries that conform to arbitrary mass-spring models, is significant for two reasons: First, it is, to the best of our knowledge, the most versatile metamaterial design technique available. It enables the efficient design of complex functionalities such as topologically protected wave propagation[31], which would be impossible to engineer using alternative approaches such as transformation optics. Second, it enforces a metamaterial design approach where the desired behavior is engineered using a discrete model description, and the actual geometry is then generated by an automated software. Working with reduced-order models has the advantage of greatly simplifying the design process, by abstracting away implementation details. In addition, once a satisfactory discrete model has been found, the same functionality can be implemented in vastly different types of systems (mechanical, thermal, electromagnetic). This approach has been extremely successful in electrical engineering, where circuits are always designed in terms of lumped elements (capacitors, inductors, resistors, etc.) without regarding the actual implementation details of the elements, and are

then physically implemented using off-the-shelf parts or specific software to generate integrated circuit blueprints.

Besides the impact of this work in the specialized fields of mechanical metamaterials and stochastic thermodynamics, this work has a broader significance because its conclusions involve simple nonlinear interaction potentials. Even though some of the publications that compose this thesis are concerned with complex and specialized interaction laws (e.g. the Hertzian contact law or interactions between permanent magnets), all publications include Taylor expanded models that demonstrate how the described phenomena apply to a much broader class of systems, requiring only quadratic or cubic nonlinearities, and therefore extensible even outside the mechanical domain.

Background and state of the art

This thesis lies at the intersection between metamaterials, nonlinear lattices and stochastic thermodynamics. Here I provide a brief introduction to each of these fields, highlighting the open questions that are addressed in this work.

Metamaterials

Metamaterials are typically defined as inhomogeneous materials having a microscopic structure that is significantly smaller than the expected wavelength of operation (but still larger than conventional atoms or molecules) and presenting one or multiple properties beyond those of conventional materials. One of the first of such unconventional properties to be proposed was the negative index of refraction, an idea that, while considered as early as in 1904[32], is typically traced back to the work of Victor Vesselago[33]. Vesselago's work rose to prominence with the work of John Pendry[4], who demonstrated in 2000 that such material could be used to build lenses not bound by diffraction limits, and suggested that these properties were attainable with the use of microscopic resonating structures such as thin slabs, wires, or rings[4]. Almost simultaneously with Pendry's work, Liu et al.[2] demonstrated that, in acoustics, microscopic resonating structures could be used to

introduce negative effective elastic properties. In Liu's work, the negative properties resulted in acoustic band-gaps, thereby enabling ultra-efficient soundproofing materials.

Since the field's beginnings with Pendry's work 17 years ago, metamaterials have been the object of numerous works, involving an ever-increasing set of phenomena and applications. Now metamaterials are used as antennas inside commercial devices, and are known to present band-gaps, act as invisibility cloaks around objects[8-11] (albeit on a limited frequency range), have sensing applications[34-36], and can be used for wireless energy transfer[37-39] or to simulate exotic physical objects such as wormholes[40, 41]. While the initial work on metamaterials was concerned with electromagnetic properties, mechanical equivalents soon followed. In the present, the field of metamaterials includes electromagnetic[8, 42-44], optical[45-47], acoustic[11, 48-52], bulk[53, 54] and plate[55, 56] (Lamb) waves in solids and thermal[57-60] systems (A somewhat arbitrary distinction, based mostly on frequency, is typically made between electromagnetic/optical and acoustic/thermal metamaterials).

In spite of the massive progress in the field of metamaterials, techniques for engineering functionality are scarce, and metamaterials designs typically involve a certain degree of intuition or heuristic reasoning about required symmetry properties[61]. This is due to the immense size of the space of possible unit cell designs, and the non-convex nature of the optimization problem. Current approaches include computationally-expensive topological optimization, combining finite element simulations with generic optimization schemes such as simulated annealing[62, 63] or genetic algorithms[63-65]. Other design techniques involve the use of a discrete set of basic building materials (labeled 0 and 1 in reference to digital electronics), which can greatly reduce the dimension of the search space during optimization[66-68]. But perhaps the most successful of such approaches is transformation optics[42, 69, 70]. Transformation optics takes advantage of Maxwell's equations invariance to coordinate transformations[71]: If the equations are expressed in a different coordinate system, they take the same form –albeit with different material parameters. With the availability of metamaterials covering the broad range of required properties, this technique has enabled the design of advanced devices such as cloaks[8-10], lenses[5-7] or electromagnetic wormholes[40, 41]. In spite of transformation optics' power to design

materials that bend waves in arbitrary ways, it is unclear that it is of any use when, for example designing metamaterials with topological, energy converting or logic capabilities. Another metamaterial design approach, proposed by Enghetta et al.[72-75] uses lumped elements (Capacitors and inductors in the case of electromagnetic metamaterial or masses and springs in a mechanical metamaterial) to describe the physics of the metamaterial building blocks. Lumped element descriptions greatly simplify the metamaterial design process. This has been exploited to engineer novel functionalities such as filters with a complex frequency response[74]. This approach is limited by the fact that there are no generic approaches to find metamaterial geometries that conform to arbitrary lumped element models. This limitation is exemplified in the design of metamaterials with topologically-protected wave propagation capabilities. While straightforward descriptions of topological lattices can be written in terms of mass-spring models[31, 76] , mechanical topological metamaterials reported in the literature have relied in a heuristic engineering of symmetry and modal degeneracy[61]. Chapter 5 of this thesis solves this problem in the regime where the coupling stiffness between unit cells is significantly smaller than the cell's local stiffness, by presenting an algorithm capable of finding geometries conforming to arbitrary mass-spring models and demonstrating it on the paradigmatic example of the topological metamaterial[31].

For the particular goal of energy harvesting and conversion, metamaterials present a diverse set of phenomena with potential for practical applications[12, 77-84]. These include the ability to focus waves on a transducer[13, 79], to localize energy[85] and to present tailored emission and absorption spectra[80, 84]. If the metamaterial incorporates nonlinearity, this functionality can be enhanced to include rectification of waves to produce a DC signal[81], and can extend the frequency of operation over a broader range[86, 87]. The field of metamaterials for energy harvesting is extremely new, with most studies having been published on or after 2013[12, 80, 81, 83]. As a consequence, new metamaterial phenomena relevant for frequency conversion application are still being discovered. In addition to the previously reported ability of metamaterials to localize and rectify energy, Chapter 3 of thesis presents a frequency conversion mechanism with tunable frequency and phase that be used to extract energy from multiple incoherent sources of mechanical energy.

The Fermi-Pasta-Ulam problem and nonlinear lattices

While studies in metamaterials initially focused on linear effects, the importance of including nonlinearity in order to realize advanced functionality (e.g. information processing or energy conversion) was identified as early as 2010 in a review by Zheludev[88]. When engineering structures consisting of nonlinear interacting unit cells, it should be taken into account that the study of nonlinear lattices has a long tradition in the physics community. As a consequence, metamaterial studies can look into prior work in nonlinear lattices to identify phenomena with potential in metamaterial applications, and nonlinear lattice studies in physics can use the design flexibility offered by metamaterials to build novel systems and investigate fundamental nonlinear phenomena such as solitons.

Its beginnings can be found in the work of Fermi, Pasta and Ulam (FPU) on the evolution from coherent motion to thermalized states in a lattice models for the nonlinear vibration of strings[89] – A work that can be seen as anticipating the field of stochastic thermodynamics, as it attempts to answer questions about the transition to thermodynamic equilibrium by explicit calculation of the system's trajectories[90]. Since the publication of FPU's report, works have explored a variety of different systems and models, such as the Klein-Gordon[91-94], Discrete Nonlinear Schrödinger [95, 96], Toda[97], Hertzian[98-101] and magnet[102] chains, spins[103], DNA[104-106] and proteins[107, 108], which differ in the mathematical properties and physical origin of the nonlinear interaction potentials. Nonlinear lattices present very diverse phenomena, which include solitons[99, 101-103, 109-113], breathers[85, 107, 114-117], band-gaps[118-120] , unidirectional wave propagation[121-123], shock waves[124], energy trapping[125-127] and various types of tunability[128-131]. As a consequence of the diverse phenomenology, nonlinear lattices have been proposed for applications in areas such as vibration[24] and impact[125, 132] mitigation, acoustic pulse focusing[133, 134], energy harvesting[135, 136], filtering[120] and mechanical logic[137, 138].

In this work, we use nonlinear lattices as model for nonlinear metamaterials. This decision is motivated by the fact that nonlinear lattices are well characterized in the literature, with proven experimental setups and accurate theoretical models. In particular, we utilize one

dimensional Hertzian and magnet chains containing defects, consisting of a particle with a lower mass. The presence of defects introduces localized states of vibration[139] that can be used as an energy input to the system.

Stochastic thermodynamics

Stochastic thermodynamics[140-143] is concerned with the physics of thermally fluctuating, low dimensional systems, such as particles that experience Brownian motion. It associates a thermodynamical interpretation to mechanical quantities such as the dissipation force or the thermomechanical noise, allowing a discussion in terms of the first law of thermodynamics and the notion of entropy production[144]. The first observation of Brownian motion is attributed to Robert Brown[145], who saw the random motion of pollen particles in the microscope; the first theoretical explanation was provided by Einstein[146], who attributed it to the thermal movement of molecules. This result was extremely ground-breaking, since it provided evidence for the molecular theory of heat, which was controversial at the time. The intersection between molecular mechanics and thermodynamics was, for some time, a contentious issue[147]. Several proposed devices, such as the Maxwell demon[148] or the Feynman ratchet[147, 149], seem to violate the laws of thermodynamics through some clever use of molecular mechanics. Resolving these paradoxes required taking into account the thermodynamic meaning of information[150-154], highlighting its physical nature and its connection to energy[155].

While works concerning the thermodynamics of fluctuating systems have existed for longer than a century, the last 20 years have seen a massive surge of interest in the field[141, 156], beginning with the work of Evans[157] on probabilistic second law violations. This current interest is motivated by recent advances in various fields. In particular, microfabrication allows us to build devices small enough to be significantly affected by Brownian motion[158], and modern computers and algorithms can solve the stochastic equations of motion for complex systems, providing a new tool for the study of out-of-equilibrium thermodynamics (The work of Evans itself was based on computer simulations). Several motivations drive this study: The desire to suppress thermodynamic fluctuations in order to improve the performance of systems such as nanomechanical sensors[158, 159], the desire of obtaining a

better understanding on thermodynamics of out-of-equilibrium systems and the quest for newer, and potentially more efficient forms of energy conversion. Remarkable results of stochastic thermodynamics include Brownian motors, which exploit Brownian motion to assist in the microscopic transport of matter and energy[160] and fluctuation theorems[144, 161-169] which relate probabilities of change for thermodynamic variables like work, heat or entropy. Among these fluctuation theorems, the most well-known are the Jarzynski[162] identity and the Crooks[161] fluctuation relation. These results have powerful applications in a variety of fields. For example, in biology, fluctuation theorems enable the determination of the free energy differences between folded and unfolded molecules of DNA[170, 171], RNA[172, 173] and proteins[174, 175] or to distinguish between different topological variants of biomolecules[176]. In spite of the recent developments, the field of stochastic thermodynamics has significant open questions. Thermodynamic concepts such as work[177] or entropy[178] do not have a universal definition in low-dimensional systems out of equilibrium, and ultimate limits in performance and power[179, 180] of stochastic devices are not known in the most general case.

A particularly active sub-field of research in stochastic thermodynamics, and one that this thesis is concerned with, is the field of stochastic heat engines[29, 30, 181-186]. Stochastic heat engines are low-dimensional systems that generate work by rectifying the thermal motion of particles. The initial concept of the stochastic heat engine originated in the work of Maxwell [148] Smoluchowski[147] and Szilard[187, 188], who proposed microscopic mechanical devices that would, hypothetically, be able to extract work from the thermal agitation of molecules in a gas. These results are of great theoretical interest, because they highlight a tension between the field of thermodynamics, that deals with macroscopic descriptions of systems containing a large number of degrees of freedom, and the field of mechanics, that describes the fundamental laws governing the microscopic dynamics of a system's constituent particles. While the apparent contradictions were later resolved by Feynman and, in a more general way, by Landauer[151], this field has now regained significant interest. This is because, while the work of Maxwell [148], Smoluchovski[147] and Szilard[187, 188] was purely theoretical, the past decade has brought the progress that allow us to build and study these systems experimentally.

Currently, the majority of experimental studies in stochastic heat engines are done on a system consisting of a colloidal particle confined by an electromagnetic or optical trapping potential[29, 168, 182, 183, 189-191], which allows the dynamic manipulation of the particle's trapping stiffness. While initial experiments sought to demonstrate statistical violations of the second law and validate the fluctuation theorems[168, 189-191], this setup allowed for the experimental demonstration of work extraction from Brownian motion. First, by demonstrating that possessing information on the state of a particle enables the extraction of energy from Brownian motion. In a landmark experiment[155], a trapped particle was subject to an electromagnetic potential that was dynamically adjusted to prevent backwards motion, using information on the particle's position obtained with a camera and a microscope. Subsequent experiments on colloidal particles demonstrated full stochastic heat engine operation without the need of active feedback, following driving protocol proposed by Schmiedl and Seifert[192]. In these experiments[29], work was produced from a temperature difference. A laser system was used to heat the colloidal particle at pre-defined time intervals, while a different laser introduced synchronized expansions and contractions of the trapping potential, following a Stirling heat cycle. After this initial demonstration of a stochastic heat engine, a variety of works have appeared that demonstrated a variety of adiabatic processes and thermal cycles using similar setups[182, 183]. Remarkable experiments in this regard have been reported in 2016, including experiments that use a single atom as the Brownian particle[30] and experiments that involve a trapped particle interacting with reservoirs containing bacteria to explore the effect of active matter[186].

A significant issue with heat engines based on trapped colloidal particles is that they are non-autonomous, since they use an external cycle or feedback loop prescribed using computer-controlled electromagnetic or optical fields. This poses two problems: First, the computers and lasers controlling the setup consume much more power than the engine produces. A typical computer's power consumption is on the order of $100W$, while a stochastic heat engine's power output is a fraction of $k_B T/\tau \approx 10^{-18}\ W$ (Here $k_B = 1.38 \cdot 10^{-23}\ J/K$ is the Boltzmann constant, $T = 300K$ is the temperature and $\tau = 1\ ms$ is the cycle duration). A second problem of non-autonomous heat engines is that the external control system prescribes the phase and frequency of the engine. This complicates the task of characterizing the engine's performance, because it limits the states that the engine can access, and because

it provides us with information on the location of the particle, which crucially affects our ability to extract energy from the system, as demonstrated previously[155]. It is possible to overcome these limitations and build autonomous heat engines by using multiple nonlinear-interacting degrees of freedom. A remarkable proposal along these lines is the optomechanical heat engine, proposed by Zhang, Bariani and Meystre[28]. In this engine, a mechanical resonator modulates an optical cavity's resonance wavelength, causing periodic heating and cooling by driving the cavity on and off-resonance with photon and phonon baths. While this approach is conceptually promising, the optomechanical nonlinearity is extremely weak, which has prevented so far the experimental realization of this engine. A different approach, proposed by Strasberg et al. [193] and experimentally realized by Koski et al.[184] utilizes single-electron interactions in quantum systems to introduce a self-sustaining thermal cycle. This approach is, however, limited to extremely small temperatures (Koski's experimental system operates below $100\ mK$) due to fragility of the quantum effects involved. The autonomous stochastic heat engine presented in Chapter 4 of this thesis overcomes the limitation of optomechanical systems by utilizing the geometric nonlinearity of a mechanical resonator, which is much larger than the nonlinear optomechanical coupling. Since the proposed engine is not based on quantum effects, it is also not limited to extremely low temperatures.

Methods

This thesis combines experimental and theoretical work. The theory is used to identify interesting phenomena, to design a suitable experimental setup, and to provide a framework to interpret the results, while the experiments are intended to confirm the theoretical predictions and validate the conclusions. Here I briefly describe the experimental and theoretical methods used.

Experimental methods

This thesis utilizes three experimental setups in Chapters 2-4 (Chapter 5 is purely theoretical). In all three setups, a system under test is subject to a mechanical excitation, and one or

various measurements are simultaneously conducted to determine the forces, displacements or velocities at different points in the system.

The setup in Chapter 2 is designed to measure the force-displacement relation of a granular material in which an internal mode of vibration is simultaneously being excited. The granular chain under test consists of 9 steel spheres (radius of 9.525 mm), held in place using polycarbonate rods. The central particle is a defect (radius 4.763 mm) that creates a localized mode of vibration and acts as the energy input of the system. The particle next to the defect is split in half to accommodate for a piezoelectric transducer (Physik Instrumente PD050.31) used to excite the defect with a high-frequency signal. The defect's motion is measured with a Polytec CLV-2534 Laser Doppler Vibrometer connected to a Zurich Instruments ZI-HF2LI Lock-In amplifier. The quasi-static lattice deformation is prescribed by using a high stroke piezoelectric actuator (Physik Instrumente P-841.60), and the resulting force is measured with an Omega LCMFD-50N strain gauge conditioned with a custom-made differential amplifier.

The experimental setup in Chapter 3 is designed to measure the spatial and frequency distribution of energy in an extended system, when a localized resonance is excited. The setup consists of a chain of magnets (containing 20 or 21 magnets depending on the particular experiment) embedded in small 3D printed cases. The magnets are kept in place by Teflon bars, and the experiments are performed on top of an air table to minimize friction. The magnet position is tracked by digital image correlation, using a Point Grey® GS3-U3-41C6C-C computer vision camera and the Vic-2D® software from Correlated Solutions™. The magnets are excited using a conductive wire perpendicular to the chain. The wire is driven from a Topping TP22 class D audio amplifier fed from Agilent 33220A signal generator.

The setup in Chapter 4 is designed to investigate the response of a nonlinear system under a stochastic excitation that mimics thermomechanical noise. It consists of two brass ribbons (Length 30 cm, thickness 250 μm) and a cantilever (Length 40 cm, see Chapter 4 for details on the geometry). The tension of the ribbons is adjusted using a linear stage. One of the ribbons is placed in a magnetic field, and mechanically excited by passing an electric current through it. The signal driving the ribbon is generated in a laptop running a custom software. The software uses the Apple™ CoreAudio® library to play band-limited white noise obtained by

performing a time-domain simulation of a 4th order low-pass filter driven with a Gaussian noise term (See the Stochastic Differential Equation section in Theoretical methods for details on the algorithm). Velocity measurements are performed in one of the ribbons and in the cantilever using two Polytec Laser Doppler Vibrometers (CLV-2534 and OFV-505). The choice of a different model for each degree of freedom is based on the material available in the lab. The signal from the vibrometers is digitized with a Tektronix DPO-3034 in high-resolution mode.

Theoretical methods

Finite element simulations – Finite element simulations in all chapters have been performed using COMSOL Multiphysics®'s structural mechanics module. COMSOL® built-in solvers have been used in all cases except in Fig. 5.2f, where the mass and stiffness matrices have been exported and solved using a separate dynamic condensation code written in C++ (See the chapter's methods section for details). In a dynamic condensation, a model for a metamaterial's unit cell is built by expressing the boundary forces in terms of the boundary displacements. This method drastically reduces the number of degrees of freedom, while having only a moderate effect on sparsity.

Linear algebra calculations – Linear algebra calculations involving a small number of degrees of freedom (<1000) have been done in MATLAB®. Linear system solutions involving a large number of degrees of freedom have been obtained using the Intel™ Math Kernel Library® PARDISO solver, which provides higher performance and allows to reuse intermediate results (LU factorization) when working with multiple right hand sides.

Compilers – Numerical C++ codes in chapters 2, 4 and 5 have been compiled using the Intel compiler in the ETH Euler cluster. Due to their low computational cost, time domain simulations in Chapter 3 have been compiled and run in a desktop computer using GCC.

Deterministic differential equations – All models based on ordinary differential equations have been simulated using a generic 4th order Runge-Kutta algorithm[194] implemented in C++, using double precision data types, except for figure 4b in Chapter 2, which required

extended precision data types due to the extremely small displacements required to stay in the linear regime. In Chapter 2, periodic steady-state solutions have been found using an accelerated method that involves performing time-domain simulations for a single period, applying small variations on the initial conditions inside a Newton-type root finding scheme, until the periodicity condition is met. This algorithm, which speeds up calculations by a factor of approximately 10, has been implemented in MATLAB®.

Stochastic differential equations – Simulations of Langevin-type dynamics have been done using a custom C++ implementation of a Stochastic Runge-Kutta algorithm[195] with strong order 1.5 (Provided as an appendix). Average quantities such as heat, work or efficiency have been determined by averaging over a certain amount of time (Typically 1000s) and also over a large number of simulations (between 500 and 1000, depending on the particular quantity). Gaussian random numbers are obtained by using Mersenne-Twister uniform random number generator and the Beasley-Springer-Moro inversion formula.

Extreme stiffness tunability through the excitation of nonlinear defect modes.

Marc Serra-Garcia[1*], Joseph Lydon[2], Chiara Daraio[1,2].

*e-mail: sermarc@ethz.ch

This chapter was published in Physical Review E[129].
© 2016 American Physical Society.
Reproduced in accordance with the journal's copyright terms.

Abstract

The incremental stiffness characterizes the variation of a material's force response to a small deformation change. In lattices with non-interacting vibrational modes, the excitation of localized states does not have any effect on material properties such as the incremental stiffness. We report that, in nonlinear lattices, driving a defect mode introduces changes in the static force-displacement relation of the material. By varying the defect excitation frequency and amplitude, the incremental stiffness can be tuned continuously to arbitrarily large positive or negative values. Furthermore, the defect excitation parameters also determine the displacement region at which the force-displacement relation is being tuned. We demonstrate this phenomenon experimentally in a compressed array of spheres tuning its incremental stiffness from a finite, positive value, to zero, and continuously down to negative infinity.

Main text

Defects are ubiquitous in materials. Initially thought to decrease a material's performance, deliberately introducing defects is now key to achieving desirable properties [196]. A characteristic feature of defects is that they allow localized states of vibration to exist in the vicinity of a defect [197]. Previous studies have explored the effect of these defect modes on the electrical [198], thermal [199, 200] and optomechanical [201] properties of materials, but no study so far has attempted the deliberate excitation of localized defect modes as a means to change bulk material properties. Having materials with extreme properties is desirable from a practical point of view, because they enable devices that can focus [4], cloak [202-204] or mitigate vibrations [2] with a performance greater than that allowed by conventional wave mechanics. This desire has motivated the use of resonances [2, 203], buckling elements [20], negative stiffness inclusions [21, 205] or magnetic coupling between particles [22, 206] in order to achieve a stiffness that is negative, zero or higher than that of diamond. These principles result in extreme material properties, but only over a narrow range of displacements [20], frequencies [52] or temperatures [21, 207].

In this letter we demonstrate a physical mechanism that results in extreme values of the incremental stiffness, defined as the change in the material's reaction force when its deformation is changed. The mechanism is based on the nonlinear interaction between lattice particles. A distinctive property of nonlinear lattices is the presence of thermal expansion [208], in which the lattice expands or contracts as a response to an increase or decrease in its vibrational energy. In our system, we drive a defect mode in a lattice with a harmonic signal. As a consequence of anharmonicity in the lattice, an external deformation affects the resonance frequency of the defect. This causes the defect mode to move in and out of resonance when the lattice is deformed. The resulting changes in the vibrational amplitude cause a dynamic expansion or contraction of the defect. This affects the force at the boundary, and therefore alters the incremental stiffness of the lattice. We use this concept to achieve negative stiffness (Fig. 2.1a).

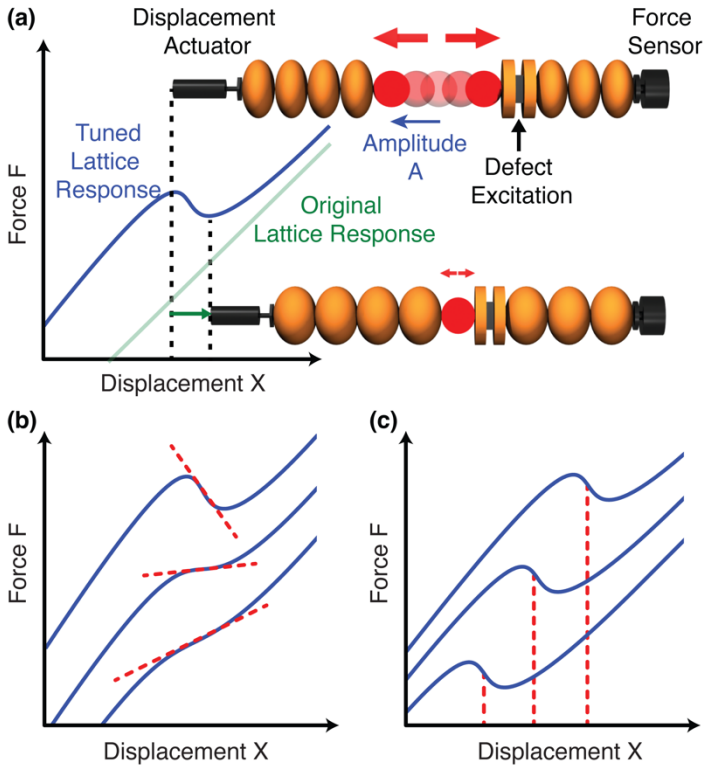

FIG. 2.1: *Tuning the stiffness through dynamic expansion.* **(a)** Schematic diagram of the tunable stiffness mechanism illustrated in a 1-D granular chain. The diagram shows the response of the lattice to a prescribed boundary displacement. During this displacement the defect is subject to a harmonic excitation at fixed frequency and amplitude, as a consequence, it vibrates with an amplitude A. As the lattice is compressed (green arrow), the defect mode is detuned from the excitation signal (red arrows). This results in a negative incremental stiffness due to dynamic contraction of the defect mode. **(b)** Changes of the driving frequency and amplitude of the excitation determine the incremental stiffness, and **(c)** the strain point at which the stiffness is being modified. The curves are offset for clarity.

We demonstrate the concept experimentally in a one-dimensional lattice of 9 coupled steel (Young modulus $E = 210\ GPa$) spheres. The spheres have a radius of $9.525\ mm$ and a mass of $28.4\ g$, except for two particles in the center. (see Fig. 2.1a, and Supplemental Information). The interaction between the spheres is modeled using the Hertzian contact law[139]. The central particle is a defect that allows the existence of a localized vibrational mode[123, 139, 197] The defect is a $4.763\ mm$ sphere. The particle next to the defect consists of a piezoelectric actuator sandwiched between two steel cylinders with $r = 20\ mm$ and $h =$

$4\ mm$. This particle is used to harmonically excite the defect mode. The lattice is kept in place using two polycarbonate rods. We monitor the defect mode vibration using a laser Doppler vibrometer pointing at the particle next to the defect. We acquire the quasi-static force-displacement relation of the lattice, by prescribing an external deformation using a piezoelectric actuator placed at one end of the chain, while simultaneously measuring the force at the opposite boundary. The vibration of the defect mode affects the force-displacement relation. The amplitude and frequency of the defect excitation control the mechanical properties of the material. Using these variables we can select both the incremental stiffness magnitude (Fig. 2.1b and Supplemental Video 1) and the displacement point where the incremental stiffness is being modified (Fig. 2.1c and Supplemental Video 2) This allows tuning the force-displacement response of a lattice at a selectable displacement value, a capability that exists in biological organisms[209], but not in systems that exhibit negative stiffness when subject to an external energy input[210, 211].

Due to the nonlinearity of the lattice, the measured force depends on both the applied displacement and on the amplitude of the mode, $F(X, A)$. Therefore, the incremental stiffness, defined as the total derivative of the force with respect to the displacement, is given by the equation:

$$\frac{dF}{dx} = \left(\frac{\partial F}{\partial X}\right)_A + \left(\frac{\partial F}{\partial A}\right)_X \frac{\partial A}{\partial X} \qquad \text{Eq. 1}$$

The first term on the right side of Eq. 1 gives the stiffness of the lattice neglecting any change in the defect mode's amplitude. The second term describes the effect of the oscillation of the defect mode. The function $(\partial F/\partial A)_X$ is the change in the force due to a change in amplitude of the defect mode and quantifies the intensity of the thermal expansion. From a dynamical point of view, this arises due to an asymmetry of the interaction potential[208] and in our lattice is always positive (see Supplemental Materials). Finally, the effect of the strain on the amplitude of the mode is contained in the quantity $\partial A/\partial X$.

The vibration amplitude's dependence on strain is a consequence of the harmonic excitation and of the nonlinearity present in the chain. The harmonic excitation results in a defect mode resonance, which occurs when the defect mode's frequency F_0 matches the excitation frequency F_d. The nonlinearity relates the mode's frequency, F_0, to the lattice strain, X[139]. In our system the Hertzian contact results in the relationship, $F_0 \propto X^{1/4}$. As a result, straining the lattice causes a change in the mode's frequency (Fig. 2.2a). If the mode's frequency approaches the excitation frequency, the mode gets closer to resonance, and therefore the oscillation amplitude increases. Conversely, if the mode frequency moves away from the excitation frequency, the oscillation amplitude decreases (Fig 2.2b.). This strain controlled resonance results in a dependence of amplitude on strain and therefore, in a non-zero $\partial A/\partial x$.

Different excitation frequencies cause the resonance to happen at different strain values (Figs 2.2a,b). This is due to aforementioned frequency strain relationship, which associates a particular resonance strain to each excitation frequency. By choosing the excitation frequency we are able to set the displacement region where the system is in resonance and the stiffness is being modified (Fig. 2.2b).

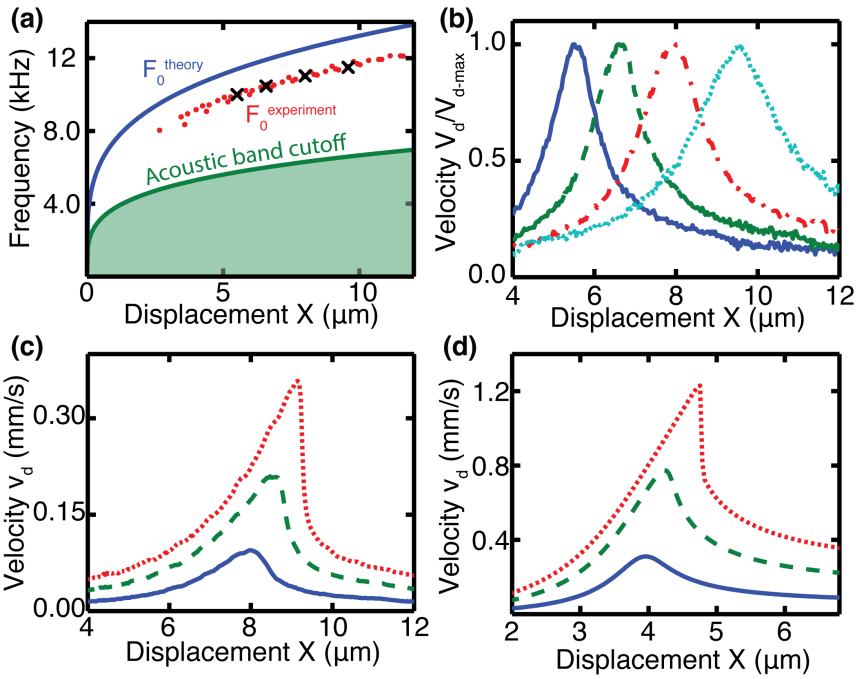

FIG. 2.2: *Response of the nonlinear defect mode*. **(a)** Theoretical defect mode (blue) and acoustic band (green) frequencies dependence on prescribed displacement. Experimental measurements are plotted as red dots with the four curves in panel **(b)** marked with black crosses. **(b)** Normalized experimental velocity of the defect mode as a function of displacement of the lattice. Curves correspond to excitation frequencies of 10(blue, solid), 10.5(green, dashed), 11(red, dashed-dotted) and 11.5 kHz (cyan, dotted). The frequencies in panel **(a)** are obtained by fitting these curves using a Lorentzian function. **(c)** Experimental velocity of the defect mode v_d, measured at the site next to the defect particle, for drive amplitudes of 4.2, (blue, solid), 9.8 (green, dashed) and 15.4 nm (red, dotted) all at 10.5 kHz. **(d)** Numerical results corresponding to c, for defects driven at 20, 50, and 80 nm, respectively. Our discrete particle model (see Methods) qualitatively reproduces the experimental results, but is unable to make precise quantitative predictions, this could be due to the fact that our model neglects experimental factors such as internal particle and actuator resonances, as well as the nonlinear friction between the particles and the rods.

The effect of the excitation amplitude on the defect's vibration is shown in Fig. 2.2c,d. As expected, driving the defect with larger harmonic forces results in larger oscillations. Furthermore, as the excitation amplitude gets larger the resonance response becomes increasingly asymmetric. This is a common property of driven nonlinear oscillators close to a

bifurcation[212]. As nonlinear system's approach bifurcation points, oscillations become extremely sensitive to the strain[213]; in our system the magnitude of $\partial A/\partial x$ approaches minus infinity. This allows us to achieve arbitrarily large negative values of incremental stiffness.

These extreme negative values have been attained experimentally. The measured force-displacement curves at four different drive amplitudes are shown in Fig. 2.3. The incremental stiffness at our selected strain progressively decreases as the defect excitation is increased (Fig. 2.3a-d). For the largest excitation amplitude, the force-displacement curve is discontinuous, indicating that the stiffness is extremely negative (Fig. 2.3d). This indicates that the excitation is very close or above the bifurcation amplitude. In order to validate that this effect is due to the defect's vibration, we simultaneously measure the defect's mode amplitude, presented below each force-displacement curve in Fig. 2.3a-d. The greatest change in the incremental stiffness happens where the slope, $\partial A/\partial x$, is the most negative. This occurs because larger changes in vibrational amplitude are accompanied by larger changes in dynamic expansion. The forces introduced by this dynamic expansion are small, a feature that we attribute to the dimensions of our system and the properties of the Hertzian interaction. It should be noted that the negative stiffness values are stable because our experiment is done under prescribed displacement boundary conditions.

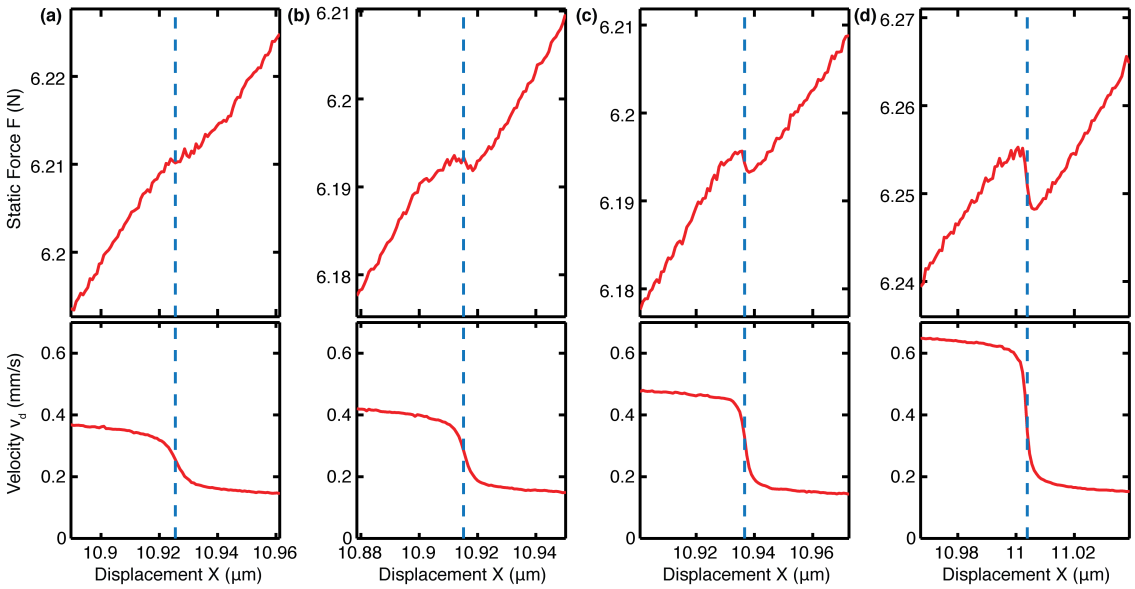

FIG. 2.3: *Experimental tuning of the incremental stiffness.* Force- displacement curves for excitation amplitudes of **(a)** 5.9 nm **(b)** 6.4 nm **(c)** 7.54 nm **(d)** 10.9 nm. Shown below are the defect mode velocities (proportional to the mode amplitude, A(x)) as a function of the overall displacement, x, of the lattice. In panel d, the system discontinuously transitions between two oscillation branches. This introduces a region of completely vertical slope in the force-displacement curve. The curves have been measured at an increasing displacement rate of 0.53 nm/s.

Each pair of drive frequency and amplitude results in a determined incremental stiffness at a particular displacement point. We explore this relationship analytically by constructing a discrete particle model. The model accounts for the nonlinear interaction between particles and for losses due to linear damping. (see Supplemental Information for a complete description) in Fig. 2.4a. The blue lines show contours at the same excitation amplitude and the red lines at the same frequency. To get a particular stiffness at a desired displacement, we select the excitation parameters corresponding to the lines passing through this point. While we only show a finite number of constant lines, all possible values in the shaded region are attainable. In the theoretical model, the stiffness tuning mechanism works to arbitrarily large displacements; in practice, the system will be limited to a smaller range due to the presence of plastic deformation at the contacts.

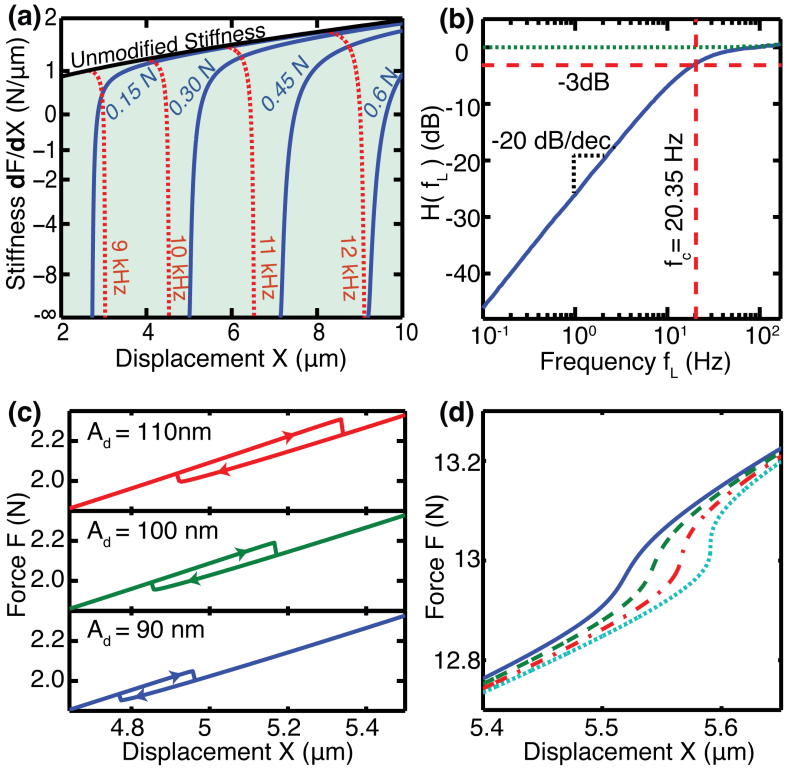

FIG. 2.4: *Theoretical Investigation.* **(a)** Map relating the excitation parameters with the modified incremental stiffness and displacement point. Each point position in the map corresponds to tuning the stiffness to the value in the Y-axis at the displacement point indicated by the X-axis. Each dotted red line defines a set of tuned stiffness states that are accomplished by the same excitation frequency. Solid blue lines represent sets of tuned stiffness that are attained by the same excitation amplitude. The intersection between red lines and blue lines determines the excitation frequency and amplitude required to achieve the stiffness labeled by the Y-axis at the displacement labeled by the X-axis. **(b)** Zero frequency band gap obtained by choosing excitation parameters corresponding to zero stiffness for the lattice. The blue and green line show the force transmitted with the defect drive on and off, respectively. When the defect excitation is turned off, the lattice acts as a linear spring for small deformations around the prescribed displacement value; when the defect excitation is turned on, there is a band-gap centered at zero frequency. The dotted red line shows the band gap edge frequency, f_c. **(c)** Force-displacement relationships of the system when it is driven above the bifurcation amplitude. The presence of a tunable hysteresis allows the system to be used as a tunable damper. **(d)** Analytical force-displacement relation for a lattice of particles with the nonlinear interaction force law $F(\delta) = A\delta^{0.5}$ (See supplemental information for details on the parameters used), with a defect excitation frequency of 13.5 KHz and amplitudes 0.72N (blue, solid), 0.74N (green, dashed), 0.76N (red, dashed-

dotted) and 0.78N (cyan, dotted). For this potential exciting the defect mode results in an arbitrarily large positive stiffness.

A remarkable feature of the mechanism presented in this letter is that it results in a zero incremental stiffness for certain defect excitation parameters. In this region the material will support a load, but it will not transmit any vibration to it, which is of great practical relevance [214]. In the zero stiffness region the lattice will have a zero frequency band gap. Tunable band gaps in mechanical metamaterials can be found in the literature [120, 215]. However, a distinctive feature of our mechanism is that it leads to band-gaps centered at zero frequency. We simulate the band-gap using our numerical model. In the simulation, the lattice is subject to a static compression. We adjust the defect's excitation frequency and amplitude to tune the stiffness to zero at this compression value. We then apply a very small amplitude periodic deformation in one end of the chain. The deformation has a frequency f_L. Simultaneously, we monitor the transmitted force at the other end (Fig 2.4b). We can see that the band gap exists only at low frequencies, and that that high frequency deformations can propagate without attenuation. We quantify the width of the band gap by fitting the transmission to a first order high pass filter, $H(f_L) = (f_L/f_c)/\sqrt{1 + (f_L/f_c)^2}$. This results in a cutoff frequency, $f_c = 20.35\ Hz$. The upper end of the band-gap is a consequence of the fact that the predicted zero stiffness force versus displacement relationship assumes a defect mode oscillating in steady-state. When we change the deformation of the lattice, the steady-state oscillation of the defect is perturbed. The system cannot recover the steady state motion instantaneously. The time it takes for the defect mode to relax back to its steady state limits the upper frequency of the band gap. The speed of the system can be analyzed by using a linear perturbation method (Floquet analysis, see Supplemental Information). It is possible to attain higher cut-off frequencies by using smaller particles (see supplementary information of ref. [21]).

At the point where the stiffness reaches minus infinity, the dynamics undergoes a bifurcation. Bifurcations are known to occur in granular lattices with defects [117]. At this bifurcation point the system goes from having a single solution to having multiple stable solutions[212].

This leads to a hysteretic force-displacement response, with the system following different paths when contracting or expanding (Fig. 2.4c). The area of the hysteresis loop corresponds to the loss of energy incurred as the lattice is driven around a compression cycle. The non-conservative forces in the system, represented by the damping and the defect excitation, will dissipate the lost energy and return the system to its initial state after a cyclic deformation. Since changing the drive amplitude can control the area enclosed in the hysteresis loop, this effect can be used to implement tunable dampers. We present an experimental observation of the tunable damping in the Supplemental Information.

The changes in the stiffness that we present in this letter arise due to the presence of a strain-controlled resonance and due to thermal expansion. These effects are a consequence of the nonlinear interaction between the lattice particles. The nonlinear interaction potential determines the sign of the thermal expansion, as well as the shape and strain-dependence of the defect resonance. Therefore, the inter-particle interaction potential determines whether the lattice's stiffness will become extremely positive or extremely negative when driving the defect mode. We explore the effect of different interaction potentials in the supplemental information. For the case of a force law of the form $F(\delta) = A\delta^{0.5}$ the excitation of the defect mode results in an increase in the stiffness, that can reach arbitrarily high values. Figure 2.4D presents the analytical force-displacement curves for this case.

We have investigated the stiffness of a lattice subject to localized defect state excitations. The nonlinearity couples the motion of the defect mode to the bulk properties of the lattice. This results in a stiffness that can take arbitrarily large positive, zero or negative values. This effect can introduce zero frequency band gaps, and for high excitation forces, the system becomes hysteretic, and can act as a tunable damper. Future studies should elucidate the equivalent phenomenon in 2D and 3D lattices, and explore the effect of engineered interaction potentials in the speed and performance of the system. While our study has focused on the effect of localized excitations on mechanical properties, we expect an analogous phenomenon to exist in electromagnetic systems, such as Varactor Loaded Split Ring Resonator arrays. This is due to the fact that those systems present quadratic[216] and

cubic[217] nonlinearities, as well as a dependence of resonances on an external static bias[218].

Supplementary: Analytical Model

The system considered in this paper consists of a chain of particles coupled through an anharmonic interaction potential (Fig. 2.S1A,B). In order to get exact results, the motion of all particles needs to be accounted for. However, studying the dynamics of a large number of particles analytically is a difficult problem. In our system, we can avoid this complexity by realizing that most of the motion is concentrated around the defect. This is a consequence of the defect mode being highly localized. This localization allows us to capture all of the essential dynamics of the system by considering a single oscillating particle and assuming that other particles in the lattice displace only quasi-statically (Supplemental Fig 2.1C, D). By using this simplification, we can qualitatively reproduce all of the effects that we have observed experimentally, such as the tuned force-displacement relationship of the lattice. In order to accomplish this, we consider the system at a prescribed total displacement, and then proceed to calculate the amplitude of vibration of the defect, as well as the static force at the boundary.

At each fixed compression value, we model the defect as a point mass M, with a dynamic displacement from equilibrium, u_d. The defect is subject to a linear damping $F_d = -b\dot{u}_d$ and a periodic excitation force $F(t) = F_e \cos(\omega t)$. As per our model approximation, we consider the neighboring particles to have a constant displacement from equilibrium denoted by Δ. We also assume that the defect motion happens only at the excitation frequency, and is given by $u_d = A\cos(\omega t + \varphi)$. We replace the particles between the defect neighbors and the walls by a linear spring with a force relation $F(\Delta) = F_0 + K_C\Delta$, where F_0 is the static force at equilibrium and K_C is calculated by linearizing the interaction force of all the particles after the defect's neighbors and lumping them into a single spring.

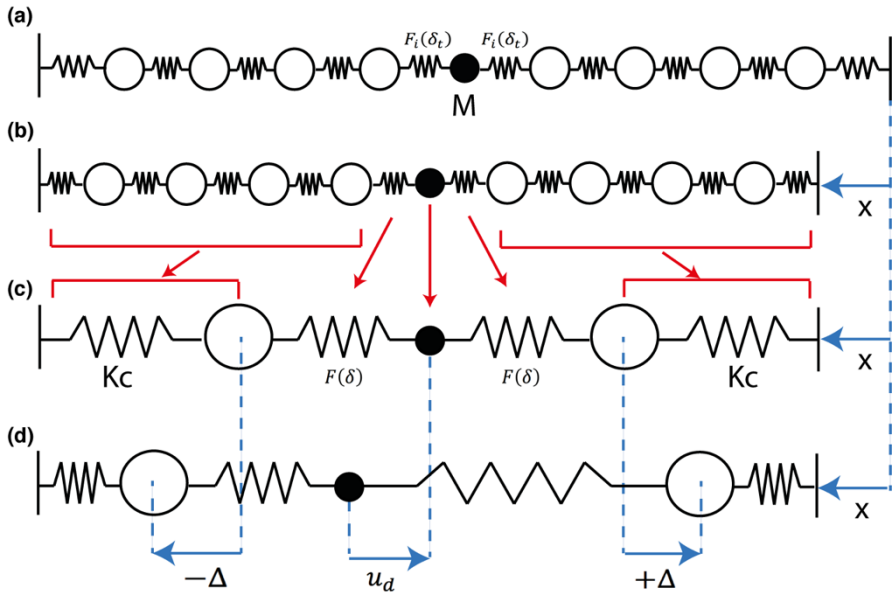

FIG. 2.S1: *Analytical model of the system.* **(a)** Initial lattice with no deformation. The lattice consists of a chain of particles, where the central particle is a defect having a mass *M* smaller than the rest of the particles. The defect interacts with the neighbors through a nonlinear force $F_i(\delta_t)$, where δ_t is the total distance separating the defect and the neighbors. **(b)** Deformed lattice. The lattice boundary has been displaced by an amount x. **(c)** Simplified system used in the analytical approximation. For each fixed displacement value x, the interaction potential between the defect and the neighbors is approximated by a third order polynomial $F(\delta)$, where $\delta = \delta_t - \delta_0$, δ_0 being the equilibrium distance between the defect and the neighbors in the deformed lattice with no defect drive. All the other beads in the chain are approximated by two linear springs K_C, with K_C calculated independently for each deformation value x. **(d)** Simplified system with the defect in motion. The defect is displaced from equilibrium by an amount u_d. The two neighboring beads are statically pushed away from it by an amount Δ due to thermal expansion.

We further simplify the system by performing a Taylor expansion of the nonlinear spring connecting the defect mode with the two half-lattices on each side. We take the Taylor expansion up to third degree, $F(\delta) = F_0 + k\delta + k'\delta^2 + k''\delta^3$. Here, $F_i(\delta_t)$ is approximated by the $F(\delta)$. A force including terms up to third degree is able to capture static equilibrium, linear oscillation, thermal expansion and resonance bending effects. The expansion is calculated around the inter-particle distance at rest, denoted by δ_0. At each deformation value, we calculate the coefficients in the Taylor expansion for the defect-neighbor interaction and the linearized spring constant for the half-lattices.

This model results in an equation of motion for the single defect particle and an equation for the static equilibrium of the defect's neighbors. Note that, due to the symmetry of the system, we only need a single equilibrium equation for the two neighbors.

$$M\ddot{u}_d + b\dot{u}_d - F(-u_d - \Delta) + F(u_d - \Delta) = F_e \cos \omega t \qquad \text{Eq. S1a}$$

$$K_C \Delta + F_0 = F(u_d - \Delta) \qquad \text{Eq. S1b}$$

To solve for the amplitude and static force, we perform a harmonic balance [212] including only components at the excitation frequency, and discarding terms containing powers of A^2 above 3. We neglect higher frequency components because they are significantly lower in the frequency spectrum of the defect's vibration. For the neighbor's equation, we neglect all the harmonic terms and take only the zero-frequency component force. This procedure results in the following condition for the amplitude of the defect:

$$A^2 \left[\left(2k + \frac{3}{4} \left[2k'' - \frac{8}{3} \left(\frac{k'^2}{K_c + k} \right) \right] A^2 - M\,\omega^2 \right)^2 + (b\omega)^2 \right] - F_e^2 = 0 \qquad \text{Eq. S2}$$

The harmonic balance condition allows us to determine the vibration amplitude of the defect, since all other variables are known: The parameters k, k', k'' and K_c depend on the total deformation of the lattice, which is prescribed. F_e and ω describe the defect excitation and are also prescribed. The defect's mass M and damping b are fixed parameters of the system.

We can get further insight on the properties of this system by realizing that the amplitude condition (Eq. S2) is identical to the one that is obtained by performing the same harmonic balance procedure on a Duffing oscillator. A Duffing oscillator is a single degree of freedom dynamical system described by the equation $\ddot{x} + \frac{1}{\tau}\dot{x} + \omega_o^2 x + \alpha x^3 = F_d/M$, and is an extremely well studied system. In order to transform our system into a Duffing oscillator, we use the equations:

$$\omega_0^2 = \frac{2k}{M} \qquad \text{Eq. S3a}$$

$$\alpha = \frac{1}{M}\left(2k'' - \frac{8}{3}\frac{k'^2}{K_c}\right). \qquad \text{Eq. S3b}$$

Knowing the vibration amplitude of the defect, it is possible to determine the thermal expansion, and therefore the force at the boundary. To do so we use the defect neighbor's equilibrium equation, and the fact that the force on the linearized spring K_C, that connects the defect's neighbors to the boundary, is the same on both ends of the spring.

$$F_b = F_0 + \frac{1}{2}\left(\frac{k'}{1+\frac{k}{k_c}}\right) A^2. \qquad \text{Eq. S4}$$

As expected, the force at the boundary is the sum of the force without any defect drive, and a thermal expansion term that increases with increasing defect motion. The thermal expansion is a consequence of the asymmetric terms in the interaction potential. During a period of the defect oscillation around an equilibrium point, symmetric terms result in an equal amount of attractive and repulsive force. In contrast, asymmetric terms introduce different amounts of attractive and repulsive force, and therefore produce a net effect in the force at the boundary.

Since the analytical model allows us to predict the static force at each displacement value, we can differentiate this prediction with respect to the displacement in order to obtain the stiffness (Eq. S5). This equation contains the original stiffness of the lattice, a term relating changes in force at the boundary to changes in the vibration amplitude of the defect, and a term due to the change in the thermal expansion coefficient as the lattice is compressed.

$$k = \frac{dF_b}{dx} = \frac{dF_0}{dx} + \left(\frac{k'}{1+\frac{k}{K_c}}\right) A \frac{dA}{dx} + \frac{1}{2} A^2 \frac{d}{dx}\left(\frac{k'}{1+\frac{k}{K_c}}\right). \qquad \text{Eq. S5}$$

The term dA/dx can be found implicitly from the harmonic balance. This is done by thinking of the balance condition (Eq. S2) as a function of the amplitude and displacement, and noting that the amplitude itself depends on the displacement:

$$\psi(A(x),x) = A^2\left[\left(2k(x) + \frac{3}{4}\left[2k''(d) - \frac{8}{3}\left(\frac{k'(x)^2}{K_c(x)+k(x)}\right)\right]A^2 - M\,\omega^2\right)^2 + (b\omega)^2\right] - F_e^2. \qquad \text{Eq. S6}$$

Since this function must stay constant at zero for all displacements, its total derivative with respect to the displacement must also be zero:

$$\frac{d\psi}{dx} = \frac{\partial\psi}{\partial A}\frac{dA}{dx} + \frac{\partial\psi}{\partial x} = 0 \qquad \text{Eq. S7}$$

From the previous equation, it is possible to obtain a closed expression for dA/dx, provided that the amplitude of oscillation is known:

$$\frac{dA}{dx} = -\frac{\left(\frac{\partial\psi}{\partial x}\right)_A}{\left(\frac{\partial\psi}{\partial A}\right)_x}. \qquad \text{Eq. S8}$$

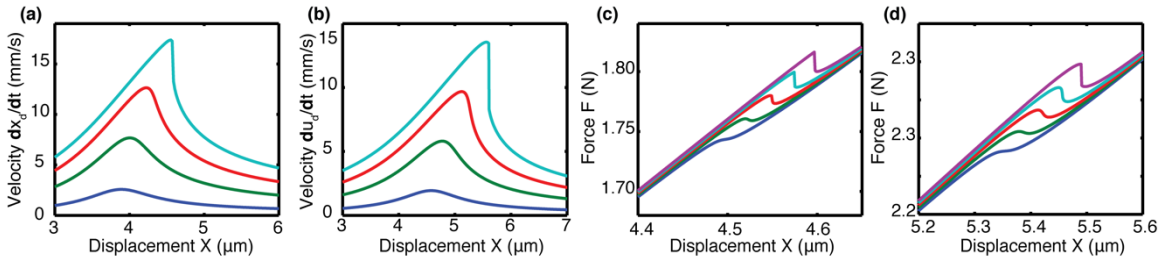

FIG. 2.S2: *Analytical predictions and comparison to numerical results.* **(a)** Defect particle velocity obtained by numerically integrating the equations of motion for the full system. The excitation amplitudes are 10 nm (blue), 30 nm (green), 50 nm (red), and 70 nm (cyan). **(b)** Defect velocity predicted by the analytical model for excitation forces of 25 mN (blue), 75 mN (green), 125 mN (red), 175 mN (cyan). The amplitudes of vibration in panels **(a)** and **(b)** correspond to the defect particle and not the defect neighbor as in Fig 2 of the main paper. **(c)** Force-displacement relation of the material obtained through numerical integration, for excitation amplitudes of 64 nm (blue), 66 nm (green), 68 nm(red) 70 nm (cyan) and 72 nm (purple). **(d)** Force-displacement relation obtained analytically, for defect drive forces of 139 mN (blue), 144 mN (green), 149 mN (red), 154 mN (cyan) and 159 mN (purple). All panels are calculated for an excitation frequency of 10.5 KHz.

We have presented a simplified model that captures the tuning of the incremental stiffness through the excitation of local defect modes. The analytical model qualitatively reproduces the results of the system in spite of the fact that it reduces the nonlinear dynamics of the

system of 9 particles to a single closed polynomial expression. We use the model to engineer the nonlinear interaction potential so it allows us to tune the stiffness to arbitrarily positive values. This is accomplished by looking at the stiffness equation (Eq. S5). When the changes in the stiffness are very large, the term $k'A\,\partial A/\partial x$ is always dominant. This is because $\partial A/\partial x$ can grow arbitrarily large, while the other terms in the equation are bounded. The term's contribution to the stiffness of the chain, K, is given by:

$$\Delta K = -\frac{A}{1+\frac{k}{K_c}}\frac{k'\left(\frac{\partial \psi}{\partial x}\right)_A}{\left(\frac{\partial \psi}{\partial A}\right)_x}. \qquad \text{Eq. S9}$$

This contribution is large when the system approaches a bifurcation. When that happens, $\partial\psi/\partial x$ tends to zero. Depending on the sign of the numerator $-k'(\partial\psi/\partial x)$, the stiffness will grow arbitrarily positive or arbitrarily negative. We study this value for a power law potential, $F = Ax^p$ (Supplemental Fig. 2.S3A). When the exponent p is between 0 and 1, the numerator is positive. In lattices with this kind of interaction force law, the stiffness can be tuned to arbitrarily positive values (Fig. 2.S3B). Recently proposed theoretical work [219], combined with novel microfabrication techniques[220] should enable the design of mechanical lattices with tailored interaction potentials. Therefore, it should be possible to create materials with stiffness that can be tuned over a broad range to positive or negative values.

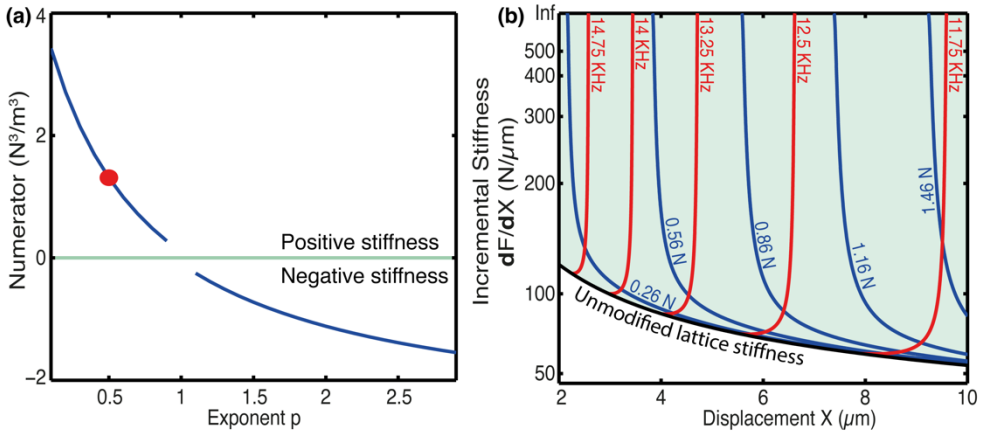

Figure 2.S3: *Stiffness tuning to positive infinity.* **(a)** Stiffness numerator corresponding to a power law potential $F = \frac{1}{p}\delta_t^p$ as a function of the exponent. Calculated for a chain of 9 particles with $\delta_T = 1$. Parameters are $M = 1$ and $b = 0.025$. **(b)** Map relating the applied excitation frequency and amplitude to the stiffness for a 9-particle lattice with a power law interaction force exponent $F =$

$Ap^{0.5}$, $A = 1.5 * 10^5$. The defect mass in the map is 3.552g and the damping τ is 0.275 ms. The force law exponent 0.5 is indicated as a red dot in **(a)**.

Supplementary: Transient Analysis

In this work, we have demonstrated that is possible to modify the force-displacement response of a lattice by applying an excitation to a defect mode. The mechanism underlying the changes in the force-displacement relation requires the defect oscillation to be in the steady state. If the lattice is deformed dynamically at high speed, the defect mode oscillation will not be able to reach the steady state. This will result in a breakdown of the picture we have presented. The goal of this section is to investigate the system's convergence towards the steady state, in order to identify the maximum frequency at which the lattice can operate, as well as its dependence on the system parameters.

Changes in the system as a perturbation of the kinematic variables

We will study the speed of convergence to the steady state by considering a system oscillating in steady-state and treating changes in the deformation of the lattice as perturbations to the steady state oscillation.

The nonlinear dynamical system presented in this letter can be described by a system of equations of the form:

$$\frac{d\vec{x}}{dt} = f^0(\vec{x}) \qquad \text{Eq. S10}$$

Where $\vec{x}$ is a vector with 2n components, n being the number of particles in the system. The first n components describe the particle's displacements from equilibrium, and the second n components describe the time derivatives of said displacements. The steady-state solution to this system will be labeled as $x_0(t)$. The function f^0 can be obtained by considering the equations of motion and the Hertzian interaction law, as described in the numerical methods part of the Materials and Methods section.

The Hertzian interaction force between particles has the form:

$$F(u_i, u_{i+1}) = A(u_i - u_{i+1} + \delta_i)_+^{\frac{3}{2}} \quad \text{Eq. S11}$$

Where A is a Hertzian contact parameter, u_i and u_{i+1} are the positions of two neighboring particles, and δ_i is the overlap between the two particles at equilibrium, computed with no defect excitation. This force law is dependent on the equilibrium overlap between the particles. When the system is compressed, this overlap will be modified and so will the force law. In this case, Eq S10 will no longer describe the dynamics of the system. Instead, we will have a new function:

$$\frac{d\vec{x}}{dt} = f^1(\vec{x}) \quad \text{Eq. S12}$$

In general, the steady-state solution $x_0(t)$ of the system f_0 will not be a steady-state solution of the system f_1. Instead, the system f_1 will have a new steady-state solution described by $x_1(t)$. If the change is small, the new steady-state solution will be close to the old steady-state solution. We will then describe the state of the system as $x(t) = x_1(t) + \Delta x$. Where $x_1(t)$ is the current exact steady state solution, and Δx is a small perturbation that must decay for the system to be in steady state. Provided that Δx is small enough, the equation of motion for the system can be linearized and expressed as:

$$\frac{d\vec{x}_1}{dt} + \frac{d\Delta\vec{x}}{dt} = f^1\left(\vec{x}_1(t)\right) + \left(\frac{\partial f_i^1}{\partial x_j}\right)_{x_1(t)} \Delta x_j \quad \text{Eq. S13}$$

Since $x_1(t)$ is a solution to the system, we know that $\frac{d\vec{x}}{dt} = f^1\left(\vec{x}_1(t)\right)$, so the previous equation can be written as:

$$\frac{d\Delta\vec{x}}{dt} = \left(\frac{\partial f_i^1}{\partial x_j}\right)_{x_1(t)} \Delta x_j = J(t)\Delta x \quad \text{Eq. S14}$$

Where $J_{ij} = \left(\frac{\partial f_i^1}{\partial x_j}\right)$ is the Jacobian of the system. This treatment results in a linear differential equation with periodically varying coefficients. This is a consequence of the fact that $x_1(t)$ is the periodic, steady state solution, and therefore its derivatives are also periodic. If the system is stable, the perturbation Δx will decay over time, and the trajectory $x(t)$ will converge to the limit cycle solution. Linear systems with time-varying, periodic coefficients can be analyzed using Floquet theory. A key result of Floquet theory is that the solution of a linear differential equation with periodic coefficients is of the form[221]:

$$\Delta x(t) = e^{-At}u(t) \qquad \text{Eq. S15}$$

Where A is a matrix quantity and $u(t)$ is a periodic function that satisfies $u(t) = \Delta x(0)$. Since $u(t)$ is periodic and therefore bounded, the rate of decay for each component of the perturbation will be bounded by the largest eigenvalue of e^{-At}. We use τ_0 to refer to the time constant associated with this largest eigenvalue. Figure 2.S4a illustrates the slowest time constant of the system, τ_0, as a function of the displacement of the lattice. This is done for different defect's excitation amplitudes. In contrast with a linear harmonic oscillator, the rate of convergence towards the steady state slows down with increasing defect excitation amplitude. The time constant diverges as the system approaches the amplitude corresponding to minus infinite stiffness, which means that the system will be limited to very slow deformations around this extreme value.

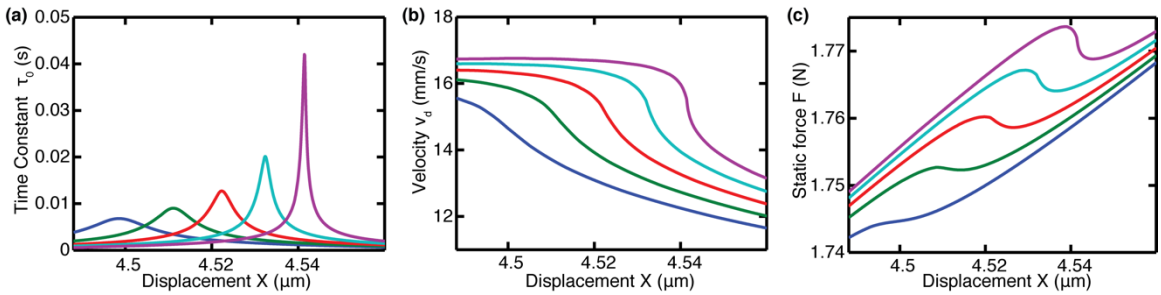

FIG. 2.S4: *Transient analysis.* **(a)** Numerical solution for the largest Floquet time constant. This value determines the speed at which the defect's oscillation relaxes back to steady state. **(b)** As the system approaches a bifurcation, the amplitude response becomes steeper, and **(c)** the stiffness is modified more significantly. This is accompanied by longer relaxation time constants, which limits

the speed of the system. In all figures, the defect's excitation frequency is 10.5 KHz. The excitation amplitudes are 64.52 nm (blue), 65.48 nm (green), 66.32 nm (red), 67.07 nm (cyan) and 67.74 nm (purple).

Among all the stiffness that can be achieved with the method described in this letter, a particular case with significant practical relevance is the zero-stiffness case. A lattice with zero stiffness presents a zero frequency band gap, similar to those that emerge when the particles are subject to a local potential. This type of system is able to block the transmission of low-frequency vibrations. However, the system is only able to block vibrations slow enough for the defect to be able to stay in steady state oscillation. We investigate the particular case of a zero-stiffness lattice using the Floquet analysis method that we have presented. The resulting slowest time constant is $\tau_0 = 7.807\ ms$. This time constant results in a cutoff frequency $f_\tau = 1/(2\pi\tau) = 20.39\ Hz$. We observe a very good agreement with the frequency cutoff $f_c = 20.35\ Hz$ obtained in Fig. 2.4B, which was obtained by numerically simulating the transmission of a vibration through the lattice. This indicates that the bound provided by the largest eigenvalue is tight, suggesting a significant gain between bulk lattice deformations and the perturbation component $u_0(t)$ associated to τ_0.

Supplementary: Materials and methods

Numerical simulations:

The numerical results are obtained by integrating the Newton's second law of motion for each of the nine particles. The interaction between particles is modeled by the Hertzian contact law [100, 222],

$$F_i(\Delta) = C_i\Delta^{3/2}\ if\ \Delta > 0\,, \qquad F_i(\Delta) = 0\ if\ \ \Delta \leq 0 \qquad \text{Eq. S16}$$

,

in which Δ is the overlap of the Hertzian potential, C_i is a contact factor between particles depending on geometry and material. Using this notation the equations of motion are:

$$m_i\ddot{x}_i = F_i(\delta_i + x_{i-1} - x_i) - F_{i+1}(\delta_i + x_{i-1} - x_i) - m_i\dot{x}_i/\tau\ . \qquad \text{Eq. S17}$$

In this equation, the force acting on each particle is given by the interaction between neighbors and a linear damping term. The linear damping, τ, as well as the Hertzian contact factors between the lattice and the setup, C_0 and C_{10}, are fitted experimentally. The equations also contain the masses of each particle, m_i, and the equilibrium static overlap between particles δ_i. The sum of the static overlaps is the total displacement (*x*) applied to the lattice. We implement the prescribed displacement boundary condition by adding two additional variables x_0 and x_{10} and holding them equal to zero. For experimental fitting and the exact numeric values used in simulations see the "Model Parameter" section below.

Experimental Methods

The experiments are carried out on a 1-D lattice of 9 stainless steel 316 beads (McMaster-Carr), with a radius of 9.525 mm. We replace the central bead by a defect bead with a radius of 4.763 mm, and we replace the bead next to the defect by a piezoelectric actuator (Physik Instrumente PD050.31) held between two stainless steel cylinders with a radius of 10 mm and a length of 4 mm. The chain is kept in place using two polycarbonate bars of 6.4 mm radius.

The amplitude of the defect mode vibration is measured using a laser Doppler vibrometer (Polytec CLV-2534) pointing at the particle next to the defect, and the compression force is measured using a static load cell (Omega LCMFD-50N) and amplified with a gain of 100. The electrical outputs from the sensors are measured with a lock-in amplifier (Zurich Instruments ZI-HF2LI). The strain on the lattice is prescribed using a high-stroke piezoelectric actuator (Physik Instrumente P-841.60). The force-displacement curves are obtained at a steady state by waiting 1.5 seconds to ensure quasistatic behavior.

Supplementary: Model Parameters

We obtain the numerical results by simplifying the complex dynamics of the granular chain to a discrete particle model following[100]. The table below lists the values used in the simulations, which are either measured experimentally or fit for. We fit for two parameters in our model.

The first is the lattices' Hertzian contact stiffness at the ends. We found that the experimental support expands slightly as a result of its finite stiffness. We include this by modifying the contact stiffness at the edges of the chain. This does not affect the dynamics at the defect site. Supplemental Figure 2.S5 shows the Hertzian fit used to find the total stiffness of the chain and supporting structure, $C_{fit}^{-2/3} = \sum_i C_i^{-2/3}$.

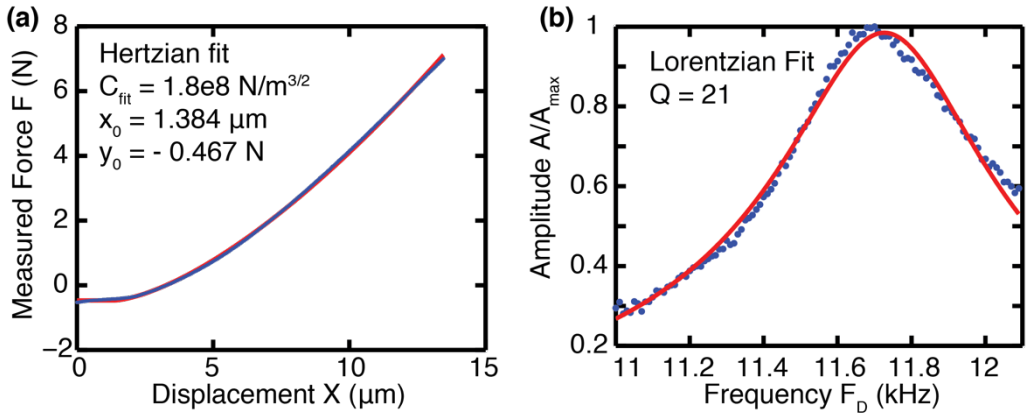

FIG. 2.S5: *Experimental fits to determine numerical parameters.* **(a)** Fit of the static response of the chain to Hertzian Force Law. **(b)** Fit of the linear amplitude response of the defect to a Lorentzian to determine the linear dissipation of the chain.

The second parameter we fit for is the linear dissipation of the particles. To find this, we perform a frequency sweep at low amplitude drive excitations in the experiment and fit the measured amplitude response to a Lorentzian. We measure the quality factor of the mode and then choose a dissipation time constant for the numerical model that results in the same quality factor for the defect mode.

The contacts at the excitation particle are modified to include the sinusoidal expansion of the chain. Because the stiffness of the piezoelectric disk is much larger than the Hertzian contacts, the piezo expands proportional to the voltage applied, and the assembled structure can be assumed to move as a single expanding bead.

$C_i = 9.7576\ N/\mu m^{3/2}, \quad i \neq 1,5,7,10$	Sphere – sphere contact stiffness
$C_1 = C_{10} = 1.7106\ N/\mu m^{3/2}, \quad i = 1,10$	Boundaries contacts stiffness

$C_5 = 7.9670\ N/\mu m^{3/2}$	Defect sphere contact stiffness
$C_7 = 13.799\ N/\mu m^{3/2}$	Excitation particle – sphere contact stiffness
$m_i = 28.4\ g, \quad i \neq 6,7$	Sphere mass
$m_6 = 3.6g, \quad m_7 = 20.2g$	Defect mass, and excitation particle mass
$\delta_i = \left(\frac{F_0}{C_i}\right)^{2/3}, \quad i \neq 6,7$	Equilibrium spatial overlap
$\delta_i = \left(\frac{F_0}{C_i}\right)^{2/3} + \frac{B}{2}\cos(2\pi f_d t), \quad i = 6,7$	Spatial overlap including the harmonic signal applied to the excitation particle
$\tau = 0.275ms$	Dissipation time constant

Table S1: Model Parameters. The values of C_1, C_{10}, m_i, m_6 and τ are experimentally measured. The value of the contacts $C_i, i \neq 1,10$ is obtained from the Hertzian contact law.

Supplementary: Experimental observation of tunable damping

When the defect mode is excited above the bifurcation amplitude, the system has two stable solutions. This results in hysteretic amplitude-displacement and force-displacement responses. Hysteretic force-displacement relations dissipate energy and therefore can be used to implement tunable dampers. Here we include an experimental observation of these hysteretic responses.

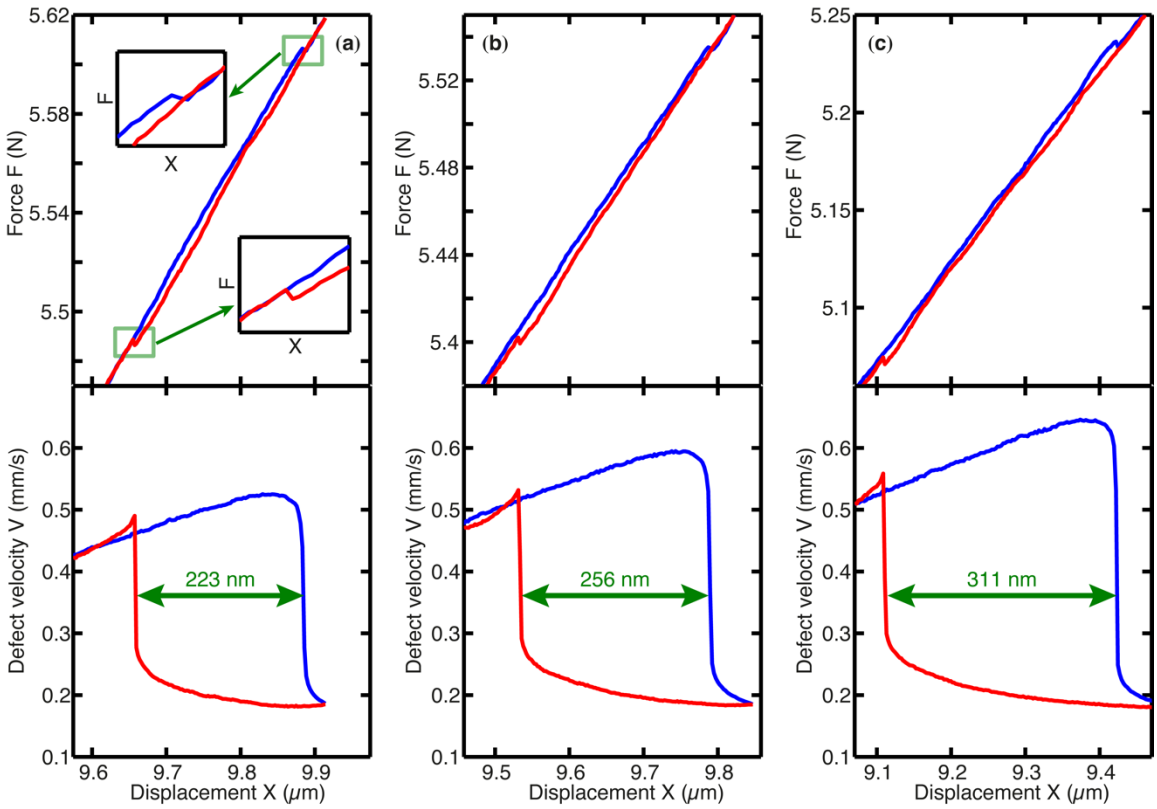

FIG. 2.S6: *Experimental tunable damping.* The upper panels present the Force-Displacement relation for an excitation of **(a)** 7.54 nm **(b)** 8.38 nm and **(c)** 9.22 nm. The lower panels show the Amplitude-Displacement relation for the corresponding excitation amplitude. The insets in **(a)** provide a detail of the Force-Displacement relation at the transition point between high and low amplitude solutions. The transition between amplitudes occurs discontinuously in a single step. The displacements have been corrected for drift at a rate of 119.4 pm/s, 141.8 pm/s and 104.5 pm/s respectively.

Supplementary: Experimental characterization of the lattice's stiffness

The incremental stiffness is defined as the derivative of the boundary force F with respect to the lattice displacement X. Calculating numerical derivatives from experimental data is hard. This is a consequence of the noise and discrete nature of the experimental measurements. Figure 2.S7 provides the numerical derivative of the force as a function of the displacement, at the point of maximally tuned slope, for a set of 25 measurements.

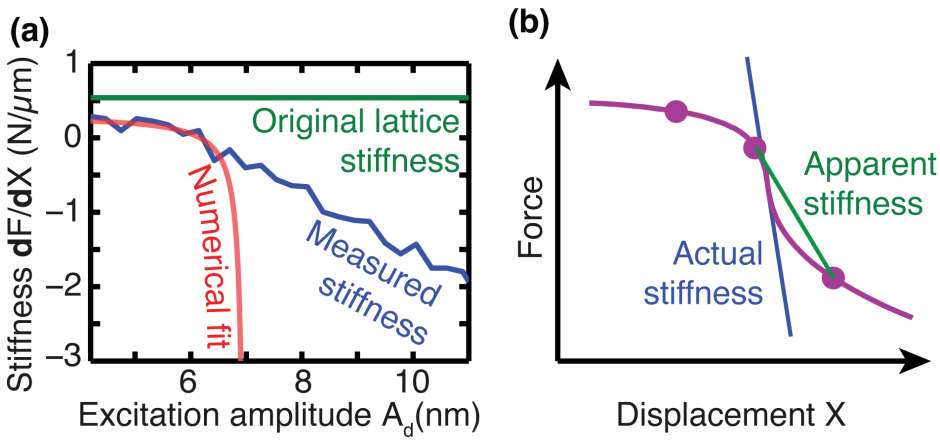

FIG. 2.S7: *Experimental measurement of the incremental stiffness.* **(a)** Comparison between the experimental stiffness (blue), obtained by numerical differentiation of the experimental results and a theoretical fit. The theoretical fit has been obtained by scaling the excitation force in the numerical prediction in order to match the initial part of the curve. **(b)** Differentiation of discretized measurements. The purple line corresponds to a numerical simulation. The dots correspond to the experimental measurements and are spaced at 10 nm to match the resolution of our setup. The green line corresponds to the stiffness obtained by numerical differentiation.

Tunable, synchronized frequency down-conversion in magnet lattices with defects

Marc Serra-Garcia*, Miguel Molerón, Chiara Daraio.

*e-mail: sermarc@ethz.ch

This work will be submitted for publication in Physical Review E.
Copyright will be owned by the publisher upon acceptance.

Abstract

We study frequency conversion in nonlinear mechanical lattices, focusing on a chain of magnets as a model system. We show that by inserting mass defects at suitable locations, we can introduce localized vibrational modes that nonlinearly couple to extended lattice modes. The nonlinear interaction introduces an energy transfer from the high-frequency localized modes to a low-frequency extended mode. This system is capable of autonomously converting energy between highly tunable input and output frequencies, which need not be related by integer harmonic or subharmonic ratios. It is also capable of obtaining energy from multiple sources at different frequencies with a tunable output phase, due to the defect synchronization provided by the extended mode. Our lattice is a purely mechanical analog of an optomechanical system, where the localized modes play the role of the electromagnetic field, and the extended mode plays the role of the mechanical degree of freedom.

Introduction

Frequency converting processes have applications in a variety of problems, for example, in obtaining different wavelengths from a fixed-frequency laser[223], harvesting energy from vibration sources[224] and generating entangled photons[225]. Typically, frequency conversion is accomplished through wave mixing[226] (which requires at least two input signals with a prescribed frequency difference), harmonic generation[223] (which produces an output that is a multiple of the input signal) and subharmonic bifurcations[227] (which produce an output that is an integer fraction of the original signal). In addition, these frequency conversion mechanisms prescribe the output's signal phase, which hinders the process of harvesting energy from multiple sources. Combination resonances[228], processes that arise in the presence of multiple nonlinearly-interacting modes, can achieve frequency down-conversion between arbitrary input and output signals not related by a harmonic or subharmonic ratios. The resulting input and output frequencies can be tuned by adjusting the modes' frequencies. Combinational resonances can be found, for example, in vibrating beams[229], membranes and plates[230].

In this paper, we show that nonlinear lattices have the potential to act as frequency-converting devices, due to the combination resonances arising from the nonlinear interaction between the lattice's normal modes. Chains of nonlinearly interacting elements have been studied for decades, beginning in the FPU problem[89, 231] . They present a wide variety of phenomena, including solitons[232, 233], band-gaps[119], energy trapping[125], breathers[85, 116], unidirectional wave propagation[123], negative or extreme stiffness[129], localized modes with tunable profile[128], shocks and rarefaction waves[124]. These phenomena can be used to realize acoustic rectifiers[123], logic gates[138], lenses[134], filters[118], vibration-attenuation[24] and energy harvesting systems[116]. Nonlinear lattices can be implemented using a broad range of materials[234], geometries[131] and interactions[102], allowing to tune the masses, coupling strengths and damping values of the particles to optimize the performance under the required operating conditions. Because of this tunability, nonlinear metamaterials are a promising candidate for energy converting devices.

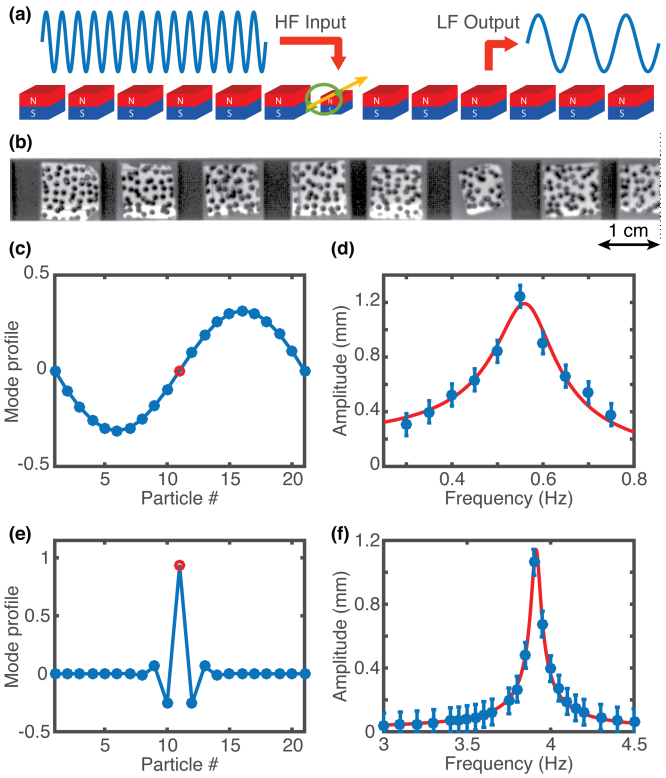

FIG 3.1: *Frequency-converting metamaterial concept.* **(a)** Metamaterial design consisting of a chain of nonlinearly-interacting magnets. The central particle of the chain is a defect, which has a lower mass. This magnet acts as the high-frequency input to the system. The down-converted energy can be extracted far away from the defect. In our experiments, the defect is driven by a wire carrying an electrical current (Yellow arrow). **(b)** Cropped image of the experimental magnet chain, obtained using the same computer vision camera that is also used to track the magnets. Each magnet is enclosed in a 3D printed case, and has a random speckle pattern to facilitate its tracking by digital image correlation. **(c)** Extended mode of vibration. The red hollow circle is the defect particle, while the blue solid dots represent the other particles. **(d)** Experimental frequency response of the extended mode (blue dots) and Lorentzian fit (red solid line). **(e)** Localized mode of vibration. **(d)** Experimental frequency response of the localized mode (blue dots) and Lorentzian fit (red solid line).

Experimental system

Our experimental setup consists of a chain of magnets[102] floating on an air table (Fig 3.1a). Each magnet is embedded in a 3D printed case that adds an additional mass, with different case designs resulting in different particle masses ($m = 0.45g$ for the non-defect particles, $m_{D1} = 0.197g$ for the first defect and $m_{D1} = 0.244g$ for the second defect). The presence of defects introduces localized modes around each defect particle (Fig 3.1b,c). When these modes are excited, the resulting motion is exponentially localized around the defect. In our experimental setup, the defects act as inputs for the frequency-conversion system. We excite them by passing current through a small conductive wire normal to the length of the chain (Fig 3.1a). The wire is driven harmonically from an Agilent 33220A signal generator amplified by a Topping TP22 class D audio amplifier. An extended mode of vibration (Fig 3.1c and d) interacts with the localized mode to introduce frequency conversion. We monitor the motion of the magnets using a Point Grey GS3-U3-41C6C-C computer vision camera, with a frame rate between 40 and 200 fps that allows us to resolve all particles' motion. We use the software VIC-2D from Correlated Solutions to track the particles and determine their trajectory.

Experimental results for the system with a single defect

We start by studying a lattice of 21 magnets containing a singe defect ($m_{D1} = 0.197g$) in the middle position (i=11). The first and last magnets are fixed. We set the excitation frequency to approximately the sum of the defect's frequency (Fig. 3.1f) and the extended mode's frequency (Fig. 3.1d), with the goal of exciting a combinational resonance ($\omega_E + \omega_L$) between the extended and localized modes [228]. We slowly increase the excitation amplitude until a threshold is reached and self-sustaining oscillations develop far away from the defect, indicating the transfer of energy between the localized mode and an extended mode (Fig. 3.2a). In this regime, the defect motion is modulated by the extended mode (Fig. 3.2b). Due to the exponential localization of the defect's motion, the Fourier transformed displacement of a particle situated far away from the defect (Fig 3.2c) does not reveal significant motion at the input frequency, and consists almost exclusively of down-converted energy. The

frequency conversion efficiency, defined as the energy dissipated in the extended mode in comparison with the energy input into the system $\eta = \frac{<b_L u_L^2>}{\sum_{1\leq i\leq n}<b_i u_i^2>}$, equals $10.8 \pm 0.9\%$. This efficiency arises from our particular system parameters and is not an absolute limit.

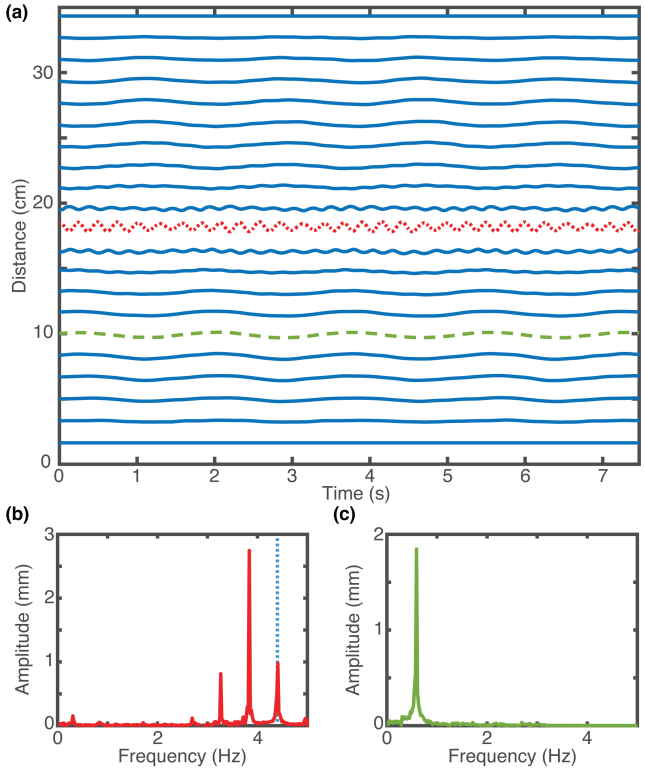

FIG 3.2: *Experimental response of the system under harmonic excitation.* **(a)** Position of the magnets as a function of time. The red dotted line corresponds to the defect magnet, which acts as the input to the frequency-converting system. The green dashed line is taken as the output of the system. **(b)** Fourier transform of the defect magnet's position, which is modulated at the extended mode's frequency. The vertical dotted line represents the excitation frequency. **(c)** Fourier transform of the output magnet's position. This magnet's motion happens primarily at the second extended mode's frequency.

Theoretical model

Our theoretical model describes the magnets as point masses. We model the interaction between particles using an empirical power-law model, $F(d) = Ad^B$, with $A = 3.378 \cdot 10^{-12} Nm^{4.316}$ and $B = -4.316$ determined experimentally (See Supplementary Information for fitted force-displacement curves). This model does not have a straightforward physical justification in terms of the material properties and the geometry of the magnets, but it is chosen because it reproduces the experimental force law with very high precision and low complexity. Using this force-displacement law we can write the equation of motion for the system (The indices in parentheses indicate that no summation is performed over them):

$$m_{(i)}\ddot{x}_{(i)} + b_{(i)}\dot{x}_{(i)} - \sum_{1\le j<i} A\left[d_0(i-j) + x_i - x_j\right]^B + \sum_{i<j\le n} A\left[d_0(j-i) + x_j - x_i\right]^B = F_i(t) \qquad \text{Eq. 1}$$

Where $m_{(i)}$ and $b_{(i)}$ are the mass and damping coefficient of the i-th particle, A and B are the magnetic force law parameters, $F_i(t)$ is the external driving force acting on the i-th particle (which may be zero if the particle is not externally driven), and d_0 is the distance between magnets at rest. When performing the reduced-order analysis, we will assume that d_0 is the same for all magnets. This is an approximation, since magnets that are not in the center of the lattice are subject to asymmetric long-range forces. However, we have found this approximation to yield acceptable results. We emphasize that our theoretical model is not limited to nearest-neighbor interactions and takes into account the magnetic force between all pairs of magnets. All numerical integration in this paper is done using a 4th order Runge-Kutta algorithm with a time step of $1\ ms$.

Reduced modal description and frequency conversion mechanism

The mechanism responsible for the frequency conversion in our lattice becomes much clearer when we look at the evolution of the system in terms of the normal modes of the linearized system. We can obtain this description by approximating the force-displacement relation by a second order Taylor series. When we do this approximation, the system becomes:

$$M_{ij}x_j + B_{ij}x_j + K_{ij}x_j + \Gamma_{ijk}x_j x_k = F_i(t) \qquad \text{Eq. 2}$$

Here the indices j and k are summed over all degrees of freedom, M, B denote the mass and damping matrices defined conventionally, and the terms K and Γ are obtained by Taylor expansion of the force law:

$$K_{ij} = \frac{d}{dx_j}\left(\sum_{1\le m<i} A[d_0(i-m) + x_i - x_m]^B + \sum_{i<m\le n} A[d_0(m-i) + x_m - x_i]^B \right) \qquad \text{Eq. 3}$$

$$\Gamma_{ijk} = \frac{1}{2}\frac{d^2}{dx_j dx_k}\left(\sum_{1\le m<i} A[d_0(i-m) + x_i - x_m]^B + \sum_{i<m\le n} A[d_0(m-i) + x_m - x_i]^B \right) \qquad \text{Eq. 4}$$

Since M is symmetric and positive-definite and K symmetric, we can find an invertible matrix P such that $P^T M P$ and $P^T K P$ are both diagonal. For simplicity we assume that the damping is proportional to the mass matrix and therefore also diagonalizable. In this basis the equations of motion become:

$$P_{im}M_{ij}P_{jn}u_n + P_{im}B_{ij}P_{jn}u_n + P_{im}K_{ij}P_{jn}u_n + \Gamma_{ijk}P_{im}P_{jn}P_{kl}u_n u_l = F_m(t) \qquad \text{Eq. 5}$$

The diagonalized system in Eq. 5 does not provide any significant numerical advantage, since Γ_{ijk} is highly non-local in the modal basis (i.e. modes far apart do interact as strongly as nearby modes). However, we can see the motivation for this approach if we look at the experimental results in the modal basis (Fig. 3.3a). In this basis, most of the motion occurs in the second extended mode and in the localized mode. In fact, these modes hold around 90% of the system's energy (Fig. 3.3b). Therefore, we can restrict our description to these two modes without incurring a significant error. This reduced-order description is:

$$m_L u_L + b_L \dot{u}_L + (k_L - 2\gamma u_E)x_L = F_I \cos(2\pi f_I t) \qquad \text{Eq. 6}$$

$$m_E \ddot{u}_E + b_E \dot{u}_E + k_E u_E - \gamma u_L^2 = 0 \qquad \text{Eq. 7}$$

In this description, u_L and u_E are the displacements of the localized and extended modes respectively, F_I is the input force, f_I is the input frequency, m_L, b_L and k_L are the effective mass, damping and stiffness of the localized defect mode, m_E, b_E and k_E are the effective mass, damping and stiffness of the extended mode. The term $\gamma = \Gamma_{ijk}P_{iE}P_{jL}P_{kL} = \Gamma_{ijk}P_{iL}P_{jE}P_{kL} = \Gamma_{ijk}P_{iL}P_{jL}P_{kE}$ denotes the quadratic interaction between modes. This term can be determined by performing a Taylor expansion of the interaction force, or by analyzing the frequency response of the local and extended modes (See Supplementary Information). We note that the reduced equations of motion present an asymmetry: There is no term proportional to x_E^2 in Eq. 6 and there is no term proportional to $x_E x_L$ in Eq. 7. These terms do not appear in our lattice due to the location of the defect, but they are not generally zero (See Supplementary Information for a study on the relation between nonlinear terms and defect location). The interaction between modes can be understood in the following way: Due to nonlinearity, the vibration of the defect mode pushes against its neighbors, in a way that is analogous to thermal expansion of a crystal[129] or the optical pressure in an optomechanical system (Fig 3.3c). For small amplitudes, this expansion is proportional to the square of the vibration amplitude, resulting in the term γx_L^2 in the extended mode equation. In addition, the motion of the extended mode modulates the distance between the defect particle and its neighbors (Fig 3.3d), thereby affecting the localized mode's effective stiffness and introducing the parametric term $\Delta k_L = \gamma x_E$, analogous to the modulation of the optical cavity wavelength in an optomechanical system. This type of interaction appears in a variety of systems such as phonon modes in superconductors[235] and can result in stochastic heat engine opearation[236]. This reduced-order model is able to reproduce the experimentally-observed behavior (Figs. 3.3e and 3.3f) with remarkable accuracy in spite of the model's simplicity and the presence of non-idealities in the system. We highlight that the only fitting parameter is the excitation amplitude. The particle mass, mode quality factor and inter-particle force law have all been measured experimentally.

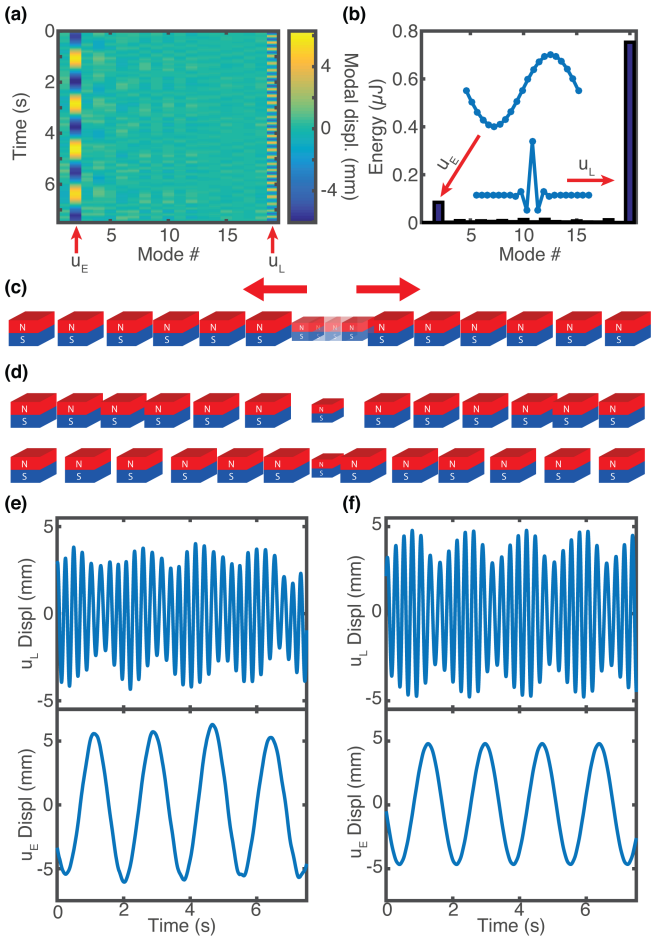

FIG. 3.3: *Reduced-order description of the frequency conversion process* **(a)** Projection of the experimental time evolution (Fig 3.2a) in the linear modal basis. **(b)** Average energy as a function of the mode number. The system's energy is highly concentrated in the second extended mode and the localized defect mode. **(c)** Dynamic expansion of the defect mode. When the defect vibrates, the nonlinear magnetic interaction results in a non-zero average force acting on the defect's neighbors. This effect is analogous to the radiation pressure in an optomechanical system. **(d)** The motion of the second extended mode modulates the distance between the defect particle and its neighbors, dynamically tuning the defect mode frequency. This effect is analogous to the mechanically-induced modulation of the Fabry-Perot resonance in an optomechanical system. **(e)** Detail of the extended mode and localized mode evolution, measured experimentally. **(f)** Theoretical prediction for the extended and localized mode evolution, obtained from a reduced-order model considering only two modes (Eq. 6 and 7). The numerical simulation in panel **f** corresponds to a system with $m_E = 0.45\ g$, $m_L = 0.232\ g$, $f_E = 0.5664\ Hz$, $f_L = 3.913\ Hz$, $f_I = 4.38\ Hz$, $F_I = 45\ \mu N$, $Q_E = 4.518$, $Q_L = 66.62$ and $\gamma = 1.801\ N/m^2$, where $k_X = m_X(2\pi f_X)^2$ and $b_X = m_X 2\pi f_X / Q_X$.

The two-mode system described in Eq. 6 and Eq. 7 is a purely-mechanical analog of an optomechanical system[25, 26, 237]. The extended mode plays the role of the low-frequency mechanical motion, while the localized mode plays the role of the high-frequency electromagnetic field. The term γx_L^2 acting on the extended mode plays the role of the optical pressure, while the term $2\gamma x_E x_L$ acting on the localized mode reproduces the modulation of the Fabry-Perot resonance by the mechanical degree of freedom in an optomechanical system. This analogy can be made explicit by expressing the motion of the defect mode as $u_L(t) = (1/2)[a(t)e^{i\omega t} + a^*(t)e^{-i\omega t}]$ and assuming that $a(t)$ changes slowly and that $1/Q_L \ll 1$. With these assumptions, we arrive at the following equation (A detailed derivation and comparison with the full model are provided in the Supplementary Information):

$$m\ddot{u}_E + b_E\dot{u}_E + k_E u_E = \gamma\frac{|a|^2}{2} \qquad \text{Eq. 8}$$

$$\dot{a} + a\left[\frac{\omega_0}{2Q_L} - i\Delta(u_E)\right] = F_I \qquad \text{Eq. 9}$$

Where ω_0 is the natural frequency of the localized mode and the detuning $\Delta(u_E)$ is the difference between the localized mode's natural frequency and the defect's excitation frequency, as a function of the extended mode's position. All other parameters have the same meaning than they did in Eq. 6 and Eq. 7. While being an approximation, this form has numerical advantages by not containing rapidly changing components at the frequency of the localized mode, and not requiring the evaluation of trigonometric functions for the excitation. Besides numerical reasons, the description provided in Eq. 8 and Eq. 9 is identical to the model of an optomechanical system[25, 237, 238], for which there is extensive analytical literature[25, 239]. This analogy provides a lucid interpretation of the frequency converting mechanism, whereby the self-sustaining oscillations of the extended more are the result of a feedback mechanism between the extended mode's motion and the localized mode amplitude. In this picture, the localized mode amplitude a depends on the extended mode displacement through the term $\Delta(u_E)$. Equation 9 imposes a retardation between a and u_E and, as a consequence, the term $\gamma|a|^2$ has a quadrature component (shifted 90 degrees from $u_E(t)$) that results in negative damping[26]. When this negative damping exceeds the value

of b_E, the system develops self-sustaining oscillations, which saturate at a finite value due to non-linearity[26].

Multiple-defect synchronized frequency conversion

Systems containing multiple defects can present synchronized frequency conversion, where the motion of multiple defects is determined by the same extended mode, thereby synchronizing the defect's modulation envelopes and resulting in the conversion of energy from multiple input frequencies to a single output frequency. The use of an extended mode to synchronize multiple resonant elements appears in the context of Josephson junction arrays[240], and here we use it to extract energy from multiple sources of mechanical vibrations. Our experimental system consists of 20 magnets, with defect particles in positions 7 ($0.244g$) and 14 ($0.197g$). The initial and final particles are fixed. As in the case with a single defect, we set an excitation frequency for each defect equal to the defect's frequency plus an extended mode's frequency. This time we use the third extended mode instead of the second, because it presents two regions of maximum strain at the two defect's positons. As we did in the single defect case, we increase both defect's excitation amplitudes simultaneously, until we observe self-sustaining oscillations far from the defect. Figure 3.4a shows the trajectories of the magnets in the self-sustaining regime. We calculate the energy transfer between both defects and the extended mode, by utilizing the empirical force-displacement relation and the defect's trajectories, and we observe that both defects are contributing energy to the extended mode with a power ($P =< F\dot{x}_E >=< \gamma x_L^2 \dot{x}_E >$) of $16.9 \pm 1.5\, nW$ and $25.8 \pm 4.0\, nW$ respectively, indicating successful extraction of energy from multiple sources. The frequency conversion efficiency is $20.5 \pm 10.4\%$. As in the previous case, the motion of the defects presents sidebands indicating a modulation by the extended mode (Fig. 3.4b). Far from the defect, the motion takes place exclusively at the extended mode's frequency, as required for successful frequency conversion operation.

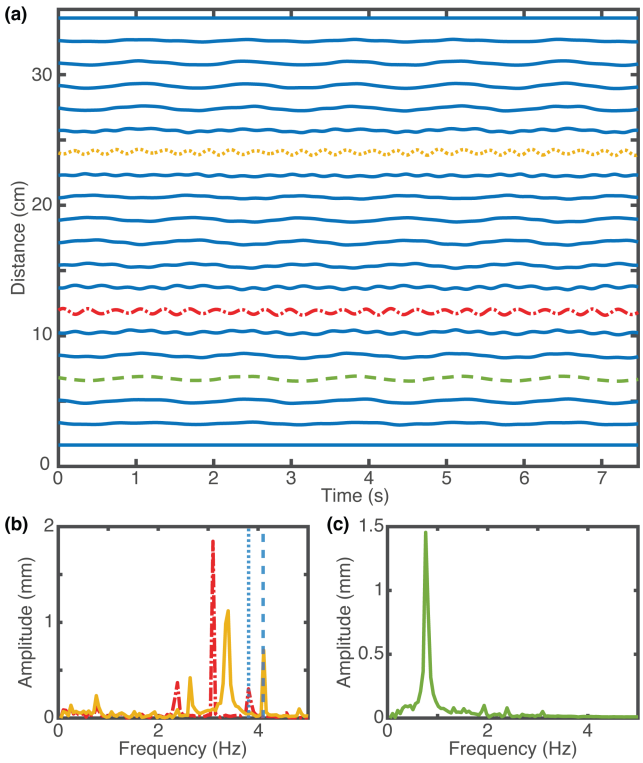

FIG. 3.4: *Synchronized frequency conversion.* **(a)** Position of the magnets as a function of time. The yellow dotted line (particle 7) and the red dotted-dashed line (particle 14) are defect magnets that act as the high-frequency inputs of the system. The green dashed line is the low frequency output. **(b)** Fourier transform of the defects' positions, which are modulated at the extended mode's frequency. The vertical dotted line represents the excitation frequency. **(c)** Fourier transform of the output magnet's position. This magnet's motion happens primarily at the third extended mode's frequency.

As in the case with a single defect, expressing the magnet's trajectories in terms of the lattice's linear normal modes reveals that the motion (Fig. 3.5a) and the energy (Fig. 3.5b) are primarily concentrated in an extended mode (Fig 3.5c, left) and in the two localized modes, the profiles of which are depicted in Fig. 3.5c. This energy concentration allows us to formulate a reduced-order description following the same procedure as in the system with a single defect. The resulting system of equations has the form:

$$m_{L1}\ddot{x}_{L1} + b_{L1}\dot{x}_{L1} + (k_{L1} - 2\gamma_1 x_E)x_{L1} = F_{I1}\cos(2\pi f_{I2}t) \qquad \text{Eq. 10}$$

$$m_{L2}\ddot{x}_{L2} + b_{L2}\dot{x}_{L2} + (k_{L2} - 2\gamma_2 x_E)x_{L2} = F_{I2}\cos(2\pi f_{I2}t) \qquad \text{Eq. 11}$$

$$m_E\ddot{x}_E + b_E\dot{x}_E + k_E x_E - \gamma_1 x_{L1}^2 - \gamma_2 x_{L2}^2 = 0 \qquad \text{Eq. 12}$$

The model in equations 10-12 is capable of qualitatively predicting the evolution of the modes (Fig. 3.5d and 3.5e), but under-estimates the output amplitude relative to the experiments. We attribute this difference to uncertainty in the system's resonance frequencies and quality factors. This is suggested by the difference between theory and experiment in the extended mode's frequencies (See Supplementary Information) and in the phase of the localized mode's vibration.

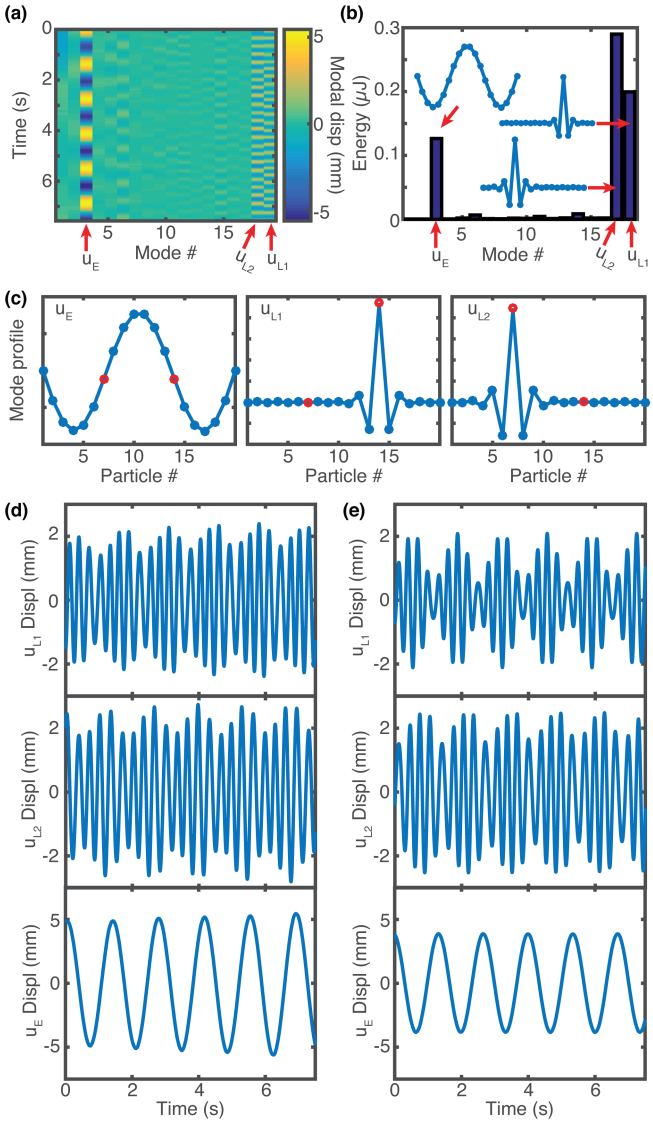

FIG. 3.5: *Reduced-order description of the synchronized frequency conversion.* **(a)** Time evolution of the magnets in terms of the linear eigenmode basis. **(b)** Energy distribution in each normal mode. The energy is concentrated in the third extended mode and in the two localized defect modes. **(c)** Mode profiles of the three most relevant eigenmodes. **(d)** Experimental time evolution of the third extended mode u_E and the two localized modes u_{L1} and u_{L2} as a function of time **(e)** Theoretical prediction for the time evolution of the eigenmodes. The theoretical predictions have been obtained using a 3-DOF

reduced order model. The numerical parameters used in panel **e** are: $m_E = 0.45\ g$, $m_{L1} = 0.2318\ g$, $m_{L2} = 0.2915\ g$, $f_E = 0.7494\ Hz$, $f_{L1} = 3.404\ Hz$, $f_{L2} = 3.063\ Hz$, $f_{I1} = 4.1\ Hz$, $f_{I2} = 3.81\ Hz$, $F_{I1} = F_{I2} = 42\ \mu N$, $Q_E = 12.27$, $Q_{L1} = 39.3$, $Q_{L2} = 60.27$, $\gamma_1 = -2.4293\ N/m^2$, $\gamma_2 = 2.5761\ N/m^2$.

Output phase tunability

In our lattice, the output signal's phase is not prescribed by the inputs and can be dynamically tuned while the system is operating. This offers an opportunity to synchronize multiple devices, create passive and tunable phased arrays or transfer information by modulating the output signal's phase. We theoretically demonstrate this output phase tunability in Fig. 3.6a-c. The phase modulation is accomplished by perturbing the last particle following a Gaussian profile given by $x_n(t) = A_P e^{-\frac{(t-t_0)^2}{2\sigma^2}}$ (Fig. 3.6a), where A_P denotes the maximum perturbation amplitude, t_0 is the moment where the perturbation is applied and σ represents the width of the perturbation. We choose a Gaussian profile because it is highly localized in both time and frequency domains. Applying this perturbation results in a change in the output signal phase, that persists long after the perturbation has vanished. Figure 3.6b shows the extended mode's displacement 1790 seconds after a perturbation, for different perturbation amplitudes (In this calculation, the perturbation width $\sigma = 30s$ is much smaller than the wait time, ensuring that no effect remains by the time the results are obtained). Two remarkable observations shall be made regarding the phase tunability shown in Fig. 3.6c: Firstly, this tunability covers the whole range ($0° - 360°$). Secondly, the perturbation-induced phase shift persists for a period of time that is much longer than any of the system's time constants, since the phase does not change significantly if we wait an additional $1000s$ until $t = 2790s$. In the experimental system, this phase stability would be limited by the presence of external noise sources and Brownian motion.

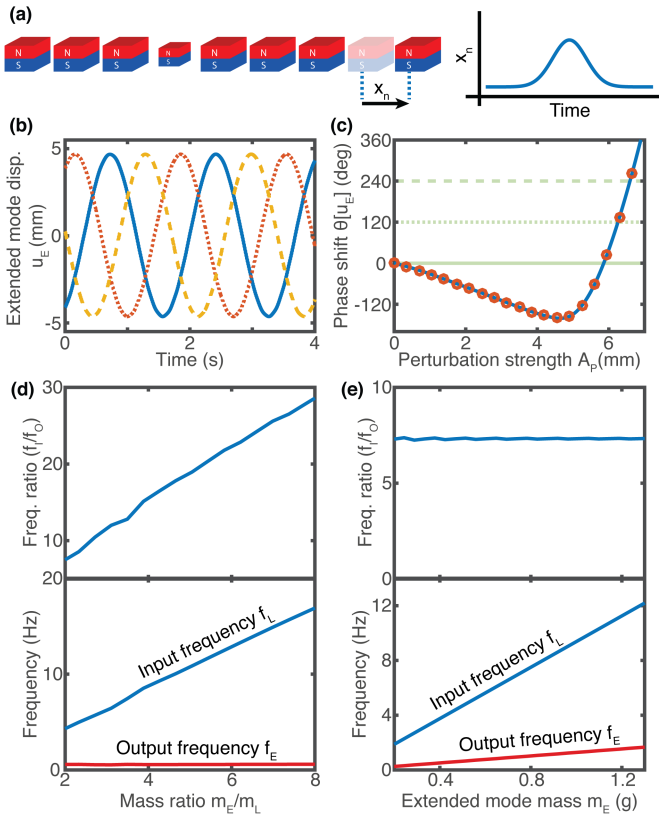

FIG. 3.6. *Theoretical investigation of phase and frequency tunability.* **(a)** Phase tuning scheme. The output signal's phase is tuned by moving the last particle (x_n) following a Gaussian profile. **(b)** Extended mode signal 2790 seconds after the phase-shifting perturbation has been effected. The lines correspond to perturbations with A_0 equal to 0 mm (blue, solid), 6.2562 mm (red, dotted) and 6.5917 mm (yellow, dashed). **(c)** Output phase as a function of the maximum displacement of the phase-adjusting perturbation. The blue solid line is measured 1790 seconds after the perturbation, while the circles are measured 1000 seconds after the first measurement, 2790 seconds after the perturbation's peak. Panels **b** and **c** have been obtained by integrating the full equation of motion (Eq. 1) with $d_0 = 16.3\,mm$, $m_{i,i\neq 11} = 0.45\,g$, $m_{11} = 0.197\,g$, $b_{i,i\neq 11} = 306.83\,\mu Ns/m$, $b_{11} = 42.62\,\mu Ns/m$, $F_{i,i\neq 11} = 0N$, $F_{11} = F_I \sin 2\pi f_i t$, $F_I = 48.45\,\mu N$ and $f_I = 4.38\,Hz$. The force-law parameters are as described in the theoretical model section. **(d)** Frequency down-conversion ratio (top) and input and output frequencies (bottom) as a function of the mass ratio between the defect and extended modes. These plots have been obtained by keeping the extended mode's mass constant and modifying the defect's mass. **(e)** Frequency down-conversion ratio (top) and input and output frequencies (bottom) as a function of the extended mode mass, while keeping the modal mass ratio m_E/m_L constant. In this section, all parameters except the masses are identical to those in Fig. **3.3f**.

Tunability

A remarkable feature of our frequency-converting system is the possibility of tuning the input and output frequencies over a broad range, both during the design phase and dynamically once the system has already been built. Figure 3.6 theoretically explores the relationship between the input and output frequencies and the modal masses. We first explore the effect of the mass ratio by altering the mass of the defect mode without altering that of the extended mode (Fig 3.6a). This results in a change in the optimal input frequency without a significant effect on the output frequency. We then proceed to alter the masses of the localized and extended mode simultaneously (Fig 3.6b). This changes both input and output frequencies, while maintaining the down-conversion ratio constant. In the conversion ratio calculation, we identify the optimal input frequency by sweeping the input between the resonance frequency of the localized mode and the resonance frequency of the localized mode plus twice the resonance frequency of the extended mode, and finding the input frequency that results in the highest energy transfer. In addition to the particle's mass, there are many unexplored avenues for tuning the frequency conversion ratio. Examples include the static compression applied on the chain, the magnet strength and geometry and the application of external magnetic fields[130]. In addition, modern 3D printed materials allow us to engineer nonlinear inter-particle interactions[219] beyond these offered by magnetic systems.

Conclusions and outlook

We have demonstrated that magnet lattices with defects are capable of converting energy from high frequencies to lower frequencies, that need not be related by harmonic/subharmonic relations. This is possible through the nonlinear coupling between extended and localized normal modes. Such frequency-converting lattice, analogous to an optomechanical system, is highly tunable in both frequency and phase, and can extract energy from multiple signals at different frequencies to generate a single-component output. This work may motivate the design of innovative nonlinear metamaterials and devices with tunable energy conversion capabilities.

Supplementary: Force-displacement relation

We experimentally determine the parameters for the interaction force by measuring the force-displacement relation and fitting it using a power law function of the form $F = Ax^B$. The measurements and fitted curve are plotted in Fig. 3.S1. Through this procedure, we obtain values of $A = 3.378 \pm 0.751\ pNm^{4.316}$ and $B = -4.316 \pm\ 0.0460$.

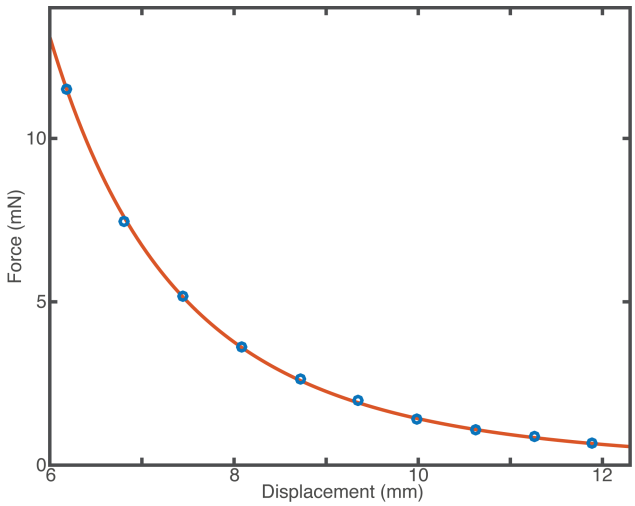

FIG 3.S1: Magnetic *force-displacement relation.* The blue circles are the experimental measurements and the red line represents the power-law fit.

Supplementary: Derivation of the optomechanical equations of motion

Here we show that the equations governing the reduced-order dynamics of the frequency converting lattice (Eq. 6-7 in the main paper) can be approximated by those describing an optomechanical system, under realistic assumptions. The equations that we want to approximate are:

$$m_L\ddot{u}_L + b_L\dot{u}_L + (k_L - 2\gamma u_E)u_L = F_I\cos(\omega t) \qquad \text{Eq. S1}$$

$$m_E\ddot{u}_E + b_E\dot{u}_E + k_E u_E - \gamma u_L^2 = 0 \qquad \text{Eq. S2}$$

We start our approximation by expressing the displacement of the localized mode as a harmonic function, with a slowly-changing amplitude and phase given by the complex function $a(t)$:

$$u_L = \frac{1}{2}\left[a(t)e^{i\omega t} + \bar{a}e^{-i\omega t}\right] \qquad \text{Eq. S3}$$

This allows us to rewrite Eq. S1 as:

$$m_L \frac{d^2}{dt^2}\frac{1}{2}\left[a(t)e^{i\omega t} + \bar{a}(t)e^{-i\omega t}\right] + \frac{m_L\omega_{0L}}{Q_L}\frac{d}{dt}\frac{1}{2}\left[a(t)e^{i\omega t} + \bar{a}(t)e^{-i\omega t}\right] + (k_L - 2\gamma u_E)\frac{1}{2}[a(t)e^{i\omega t} + \bar{a}(t)e^{-i\omega t}] = \frac{1}{2}[F_0 e^{i\omega t} + \bar{F}_0 e^{-i\omega t}] \qquad \text{Eq. S4}$$

For equation S4 to hold, terms multiplied by $e^{i\omega t}$ must be identical on both sides of the equation (Taking terms multiplied by $e^{-i\omega t}$ would yield an identical condition. This identity results in:

$$m_L \frac{d^2}{dt^2}\left[a(t)e^{i\omega t}\right] + \frac{m_L\omega_{0L}}{Q_L}\frac{d}{dt}\left[a(t)e^{i\omega t}\right] + (k_L - 2\gamma u_E)a(t)e^{i\omega t} = F_0 e^{i\omega t} \qquad \text{Eq. S5}$$

By evaluating the derivative and both sides by $e^{i\omega t}$ we obtain:

$$m_L\left[-\omega^2 a(t) + 2i\omega\dot{a}(t) + \ddot{a}(t)\right] + \frac{m_L\omega_{0L}}{Q_L}\left[i\omega a(t) + \dot{a}(t)\right] + (k_L - 2\gamma x_E)a(t) = F_0 \qquad \text{Eq. S6}$$

Now we make our first assumption: That the localized mode amplitude and phase are slowly changing. This allows us to neglect the second derivative of a in Eq. S6, resulting in:

$$m_L\left[-\omega^2 a(t) + 2i\omega\dot{a}(t)\right] + \frac{m_L\omega_{0L}}{Q_L}\left[i\omega a(t) + \dot{a}(t)\right] + (k_L - 2\gamma x_E)a(t) = F_I \qquad \text{Eq. S7}$$

Which can be regrouped as:

$$\left[\frac{\omega_{0L}}{Q_L} + 2i\omega\right]\dot{a}(t) + \left[\frac{k_L - 2\gamma u_E}{m_L} - \omega^2 + \frac{\omega_{0L}}{Q_L}i\omega\right]a(t) = \frac{F_I}{m_L} \quad \text{Eq. S8}$$

Since Q_L is a large value (40-60 in our experimental setup) and ω_{0L} is of the same order than ω, we can neglect the contribution of ω_{0L}/Q_L in the right hand side. This results in:

$$\dot{a}(t) + \left[\frac{-i}{2\omega}\left(\frac{k_L - 2\gamma u_E}{m_L} - \omega^2\right) + \frac{\omega_{0L}}{2Q_L}\right]a(t) = \frac{F_I}{2\omega m_L} \quad \text{Eq. S9}$$

We note that the term $(k_L - 2\gamma x_E)/m_L$ is the square of the localized mode's angular frequency, as a function of the displacement of the extended mode. We call this term $\left(\omega_{0L}(x_E)\right)^2$ to distinguish it from the natural frequency of the localized mode when the extended mode is at rest ($x_E = 0$), which we termed ω_{0L}. By defining the detuning $\Delta(x_E) = \omega_{0L}(x_E) - \omega$ as the difference between the natural frequency $\omega_{0L}(x_E)$ and the excitation frequency, we obtain:

$$\dot{a}(t) + \left[\frac{-i}{2(\omega_{0L}(u_E) - \Delta(u_E))}\left(\left(\omega_{0L}(u_E)\right)^2 - \left(\omega_{0L}(u_E) - \Delta(u_E)\right)^2\right) + \frac{\omega_{0L}}{2Q_L}\right]a(t) = \frac{F_I}{2\omega m_L} \quad \text{Eq. S10}$$

Expanding the squares in the left hand side of Equation 10, we obtain:

$$\dot{a}(t) + \left[\frac{i(\Delta(u_E) - 2\omega_{0L}(u_E))\Delta(u_E)}{2(\omega_{0L}(u_E) - \Delta(u_E))} + \frac{\omega_{0L}}{2Q_L}\right]a(t) = \frac{F_I}{2\omega m_L} \quad \text{Eq. S11}$$

Since $\Delta \ll \omega_{0L}(x_E)$ we can neglect the additive term $\Delta(x_E)$ in the numerator and denominator:

$$\dot{a}(t) + \left[\frac{i(-2\omega_{0L}(u_E))\Delta(u_E)}{2(\omega_{0L}(u_E))} + \frac{\omega_{0L}}{2Q_L}\right]a(t) = \frac{F_I}{2\omega m_L} \quad \text{Eq. S12}$$

Which can be simplified to the equation for a classical optomechancial system:

$$\dot{a}(t) + \left[\frac{\omega_{0L}}{2Q_L} - i\Delta(u_E)\right] a(t) = \frac{F_I}{2\omega m_L} \quad \text{Eq. S13}$$

We now examine the equation for the extended mode, by replacing $u_L(t)$ (Eq. S3) into Eq. S2. :

$$m_E\ddot{u}_E + b_E\dot{u}_E + k_E u_E - \frac{\gamma}{4}\left(a^2 e^{i2\omega t} + \bar{a}e^{-i2\omega t} + 2a\bar{a}\right) = 0 \quad \text{Eq. S14}$$

By neglecting the rapidly varying degrees of freedom at 2ω, we arrive at the equation:

$$m_E\ddot{u}_E + b_E\dot{u}_E + k_E u_E - \frac{\gamma}{2}|a|^2 = 0 \quad \text{Eq. S15}$$

Equations S13 and S15 correspond to the optomechanical model presented in the main paper.

Supplementary: Tuning the nonlinear parameters by modifying the defect's location

We can tune the nonlinear parameters in our reduced-order model by changing the defect location. The most general equation of motion for the system, truncated to contain only second-order terms, is given by:

$$m_L\ddot{u}_L + b_L\dot{u}_L + k_L u_L - \beta_L u_L^2 - 2\gamma_E u_L u_E - \gamma_L u_E^2 = F_I\cos(\omega t) \quad \text{Eq. S16}$$

$$m_E\ddot{u}_E + b_E\dot{u}_E + k_E u_E - \beta_E u_E^2 - 2\gamma_L u_L u_E - \gamma_E u_L^2 = 0 \quad \text{Eq. S17}$$

Figure 3.S2 presents the nonlinear parameters as a function of the defect location. The selected defect locations maximize the γ_E coupling, while ensuring that all other nonlinear parameters are small. The point of maximal γ_E corresponds to the region where the mode's strain $\epsilon_i = x_{i+1} - x_i$ is maximal, resulting in the highest change in the defect-neighbor distance during the motion of the extended mode.

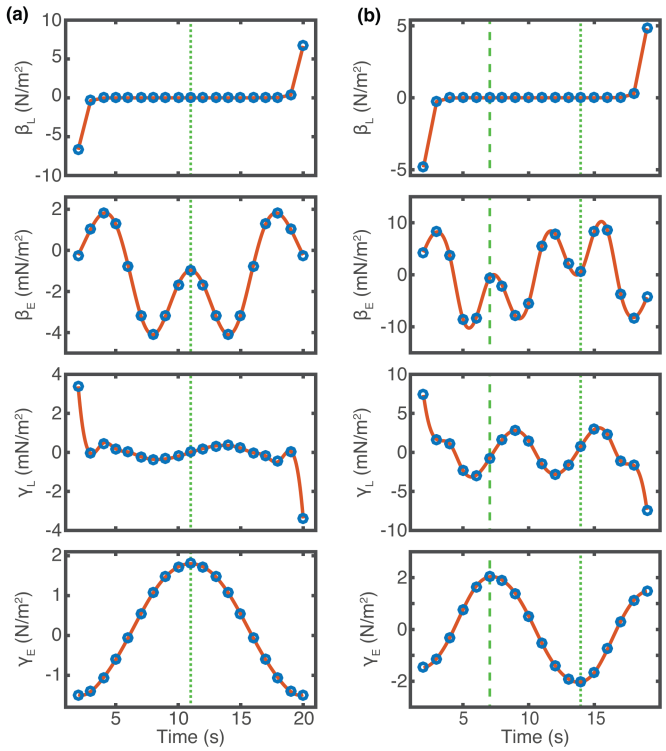

FIG 3.S2: *Nonlinear parameters as a function of the defect location.* **(a)** Here, the extended mode is the second extended mode of the lattice, corresponding to the single-defect system in the main paper. **(b)** The extended mode is the third extended mode of the lattice, corresponding to the two-defects system in the main paper. In both panels, the dotted line represents the experimental light defect location. In panel **b**, the dashed line represents the heavy defect location.

Supplementary: Comparison between full, reduced and optomechanical system

Here (Fig. 3.S3) we present a comparison between the system's evolution predicted by the full model (Eq. 1 in the main paper), the two-mode reduced order model (Eq. 6 and Eq. 7 in the main paper). and the optomechanical model (Eq. 8 and Eq. 9 in the main paper).

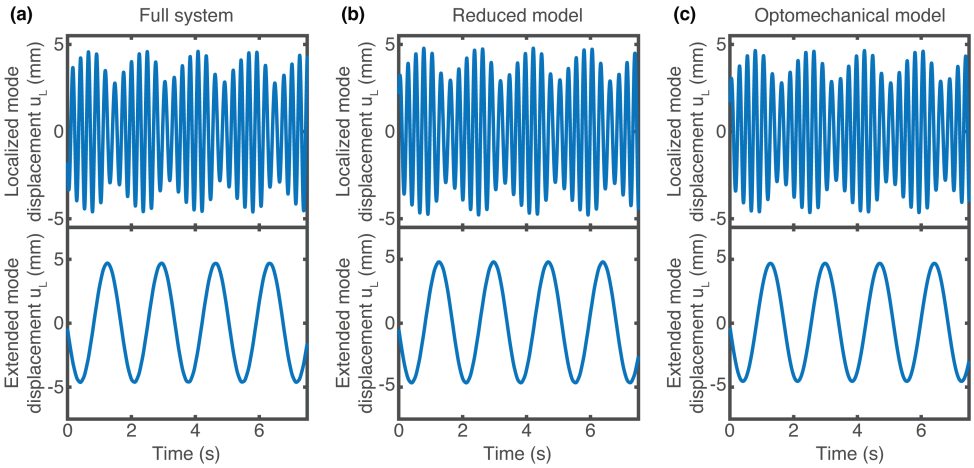

FIG 3.S3: *Comparison of full and reduced models.* **a** Time evolution of the localized and extended modes calculated using the full system simulation. The modal description has been obtained by projecting the trajectories into the modal basis. **b** Modal time evolution calculated using the two-mode reduced order model. **c** Modal time evolution calculated using the optomechanical model. The $t = 0$ point has been selected independently in each simulation, in order to present a consistent phase.

We observe that the three models produce similar predictions. This allows us to conclude that a reduced-order modelling approach provides a good approximation, and that our nonlinear lattice accurately mimics the dynamics of an optomechanical system.

Supplementary: Determination of the natural frequencies in the two-defect system

Here we discuss the determination of the resonance frequencies and quality factors for the third extended mode and the two localized modes, used in the section *Multiple-defect syncronized frequency conversion* of the main paper. The frequency is determined by exciting the modes using a variable frequency signal. We monitor each particle's motion and project it into the theoretically-predicted modal basis. The amplitude is determined by calculating the RMS value of the modal coordinate after subtracting the average. We then fit the frequency response using a Lorentzian function to obtain the mode's frequency and quality factor.

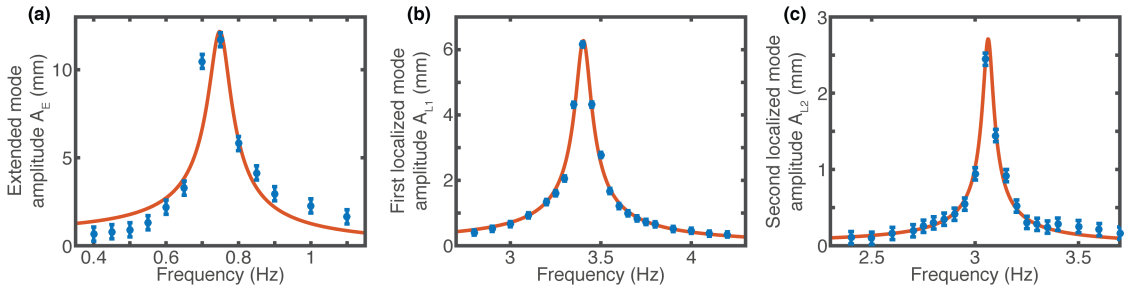

FIG 3.S4: *Fitting of the two-defect system parameters.* **a** Frequency response of the third extended mode. **b** Frequency response of the first localized mode (Centered around the defect with mass $m_{D1} = 0.197\ g$. **c** Frequency response of the second localized mode (Centered around the defect with mass $m_{D1} = 0.244\ g$

Extended mode	Frequency	$0.7494 \pm 0.0197\ Hz$
	Quality factor	12.27 ± 6.24
First Localized mode	Frequency	$3.404 \pm 0.004\ Hz$
	Quality factor	39.30 ± 3.35
Second localized mode	Frequency	$3.063 \pm 0.004\ Hz$
	Quality factor	60.27 ± 10.34

Table 1: *Two-defect system model parameters.*

Supplementary: Determination of the nonlinear constant from the frequency response

In all of our paper's simulations, the nonlinear parameter γ has been determined by performing a Taylor expansion of the magnetic force-displacement relation presented in Fig. 3.S1. In some circumstances (For example, in microscopic systems) it may not be possible to accurately measure the interaction potential. Here we calculate the nonlinear parameter γ from the frequency response curves (Fig. 3.S5a), by simultaneously monitoring the displacement of the extended mode (Fig. 3.S5b) during the frequency response characterization.

The equation of motion for the extended mode is given by:

$$m_E\ddot{u}_E + b_E\dot{u}_E + k_E u_E - \gamma u_L^2 = 0$$ Eq. S18

For excitation amplitudes below the self-oscillation threshold, u_L follows a harmonic motion with constant amplitude. Under these conditions, u_E cannot follow the rapid changes of u_L^2 and reacts only to its average value. Since the displacement of u_E during the frequency response measurement is quasistatic, we can neglect the terms $m_E\ddot{u}_E$ and $b_E\dot{u}_E$. This results in the equation:

$$< u_E >= \left(\frac{\gamma}{k_E}\right) < u_L^2 >$$ Eq. S19

Figure 3.S5c presents the extended mode displacement as a function of the localized mode amplitude. By fitting this relation using a quadratic polynomial, we obtain a nonlinear coefficient $\gamma = 1.79 \pm 0.56\ N/m^2$ which compares extremely well with the value $\gamma = 1.81 \pm 0.42\ N/m^2$ obtained from the experimental force-displacement relation.

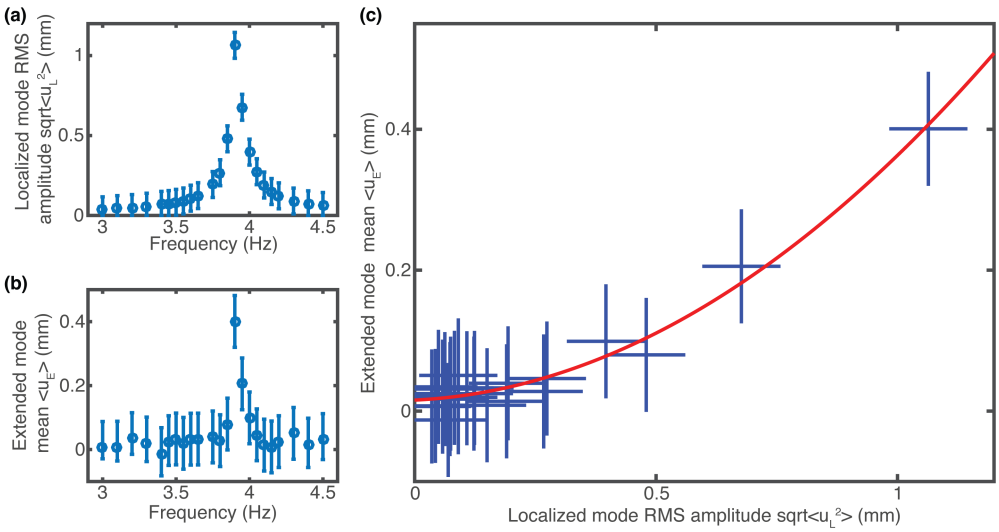

FIG 3.S5: *Experimental determination of the nonlinear parameter γ.* **a** Frequency response of the localized mode. **b** Displacement of the extended mode as a function of the localized mode excitation frequency, measured simultaneously with panel **a**. **c** Experimental relationship between localized mode amplitude and extended mode static displacement (Crosses), and polynomial fit (Red line).

Mechanical autonomous stochastic heat engine

Marc Serra-Garcia*, André Foehr, Miguel Molerón, Joseph Lydon, Christopher Chong, Chiara Daraio.

*e-mail: sermarc@ethz.ch

This work was published in Physical Review Letters[236].
© 2016 American Physical Society.
Reproduced in accordance with the journal's copyright terms.

Abstract

- Stochastic heat engines are devices that generate work from random thermal motion using a small number of highly fluctuating degrees of freedom. Proposals for such devices have existed for more than a century and include the Maxwell demon and the Feynman ratchet. Only recently have they been demonstrated experimentally, using e.g., thermal cycles implemented in optical traps. However, recent experimental demonstrations of classical stochastic heat engines are nonautonomous, since they require an external control system that prescribes a heating and cooling cycle, and consume more energy than they produce. This Letter presents a heat engine consisting of three coupled mechanical resonators (two ribbons and a cantilever) subject to a stochastic drive. The engine uses geometric nonlinearities in the resonating ribbons to autonomously convert a random excitation into a low-entropy, nonpassive oscillation of the cantilever. The engine presents the anomalous heat transport property of negative thermal conductivity, consisting in the ability to passively transfer energy from a cold reservoir to a hot reservoir.

Main text

Thermodynamics in low-dimensional systems far from equilibrium is not well understood, to the point that essential quantities such as work[177] or entropy[241] do not have universally valid definitions in such systems. Formulating a physical theory for thermal processes in low dimensional systems is the subject of stochastic thermodynamics[1], an emergent field that has resulted in the discovery of a variety of microscopic heat engines[29, 155, 183, 184, 193, 242-245], fluctuation theorems[144, 161, 162, 246] and provided new insights on the connection between information and energy[152, 155, 247-249]. A central problem in stochastic thermodynamics is the construction and analysis of stochastic heat engines, the low dimensional analogs of conventional thermal machines. A stochastic heat engine is a low-dimensional device that operates between two thermal baths at different temperatures, and is able to produce work while suppressing the randomness inherent in thermal motion[29, 155, 177, 183, 192, 242, 250, 251]. Thermal engine operation is characterized by the presence of nonpassive states of motion, which have lower entropy (for the same energy) than equilibrium states[16, 17] and therefore allow the extraction of energy without an associated entropy flow[177]. The interest in stochastic heat machines is motivated by the desire to understand energy conversion processes at the fundamental level. This understanding, coupled with modern nanofabrication techniques is expected to result in more efficient and powerful thermal machines.

The concept of the stochastic heat engine dates back to the classical thought experiments of the Maxwell demon[148, 248] and the Feynman ratchet[147, 149]. Only very recently have working experimental realizations of the stochastic heat engine been reported on[29, 155, 183, 184, 242]. The bulk of these experimental realizations is based on the manipulation of a particle in an optical trap, and include the implementation of adiabatic processes[183], feedback loops[155], as well as Stirling[29] and Carnot[242] cycles. These engines are nonautonomous since they operate under externally prescribed cycles. As a consequence, the energy they require to operate is orders of magnitude higher than the work they produce, and the externally prescribed dynamical cycle masks the significant challenges that hinder the description of autonomous physical systems[177]. In this Letter, we describe a classical

mechanical system that realizes autonomous thermal engine operation. Our proposed engine consists of two coupled ribbons and a cantilever beam connected to one of the ribbons. The presence of nonlinearity in the ribbons dynamically and autonomously adjusts the coupling to the hot and cold thermal baths, thus replacing the external control unit in the non-autonomous realizations reported until now. We demonstrate this concept in a macroscopic table-top setup, utilizing two 30 cm long brass ribbons and a 40.6 cm long steel cantilever (see Supplementary Information). Since our system is too large to exhibit sufficient Brownian motion at room temperature, we magnetically excite one of the ribbons using white noise to simulate a high effective temperature, T_H (up to $5 \cdot 10^{18}\, K$). In the Supplementary Information, we numerically demonstrate the engine's scaling to microscopic dimensions, where Brownian motion at experimentally accessible temperatures (150 ºC) is sufficient to induce measurable self-sustained thermal engine operation.

The thermal cycle of our engine is analogous to the classical Stirling cycle (Fig. 4.1a and b), which consists of four steps performed on a working fluid -- heating, expansion, cooling and compression. The ribbon attached to the cantilever (main ribbon, with displacement denoted x_M) plays the role of the working fluid. This ribbon is in contact with a cold thermal bath at temperature T_C (in our experimental setup T_C is the temperature of the ribbon's environment, 293 K). The cantilever, also at room temperature $T_W = 293K$, acts as a piston that introduces cyclic compressions and expansions of the ribbon and extracts work from the fluctuations in the ribbon's tension. Due to geometric nonlinearity, this tension increases proportionally to the ribbon's vibrational energy and is analogous to the pressure of the gas in a conventional engine. A hot thermal bath, at temperature T_H introduces the thermal noise that causes Brownian motion. This heat bath is applied to a secondary ribbon (labeled x_H). The secondary ribbon is weakly coupled to the main ribbon and regulates the coupling between the hot reservoir and the main ribbon (Fig. 4.1c and d)

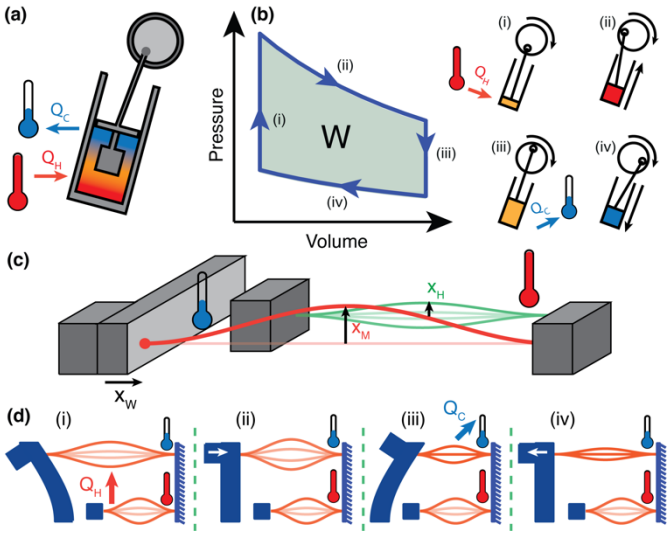

FIG. 4.1: *Cyclic thermal engines.* ***(a)*** Stirling heat engine. The engine uses a piston to cyclically compress and expand a gas. A secondary piston displaces the gas and regulates the coupling to the hot and cold reservoirs. **(b)** Thermal cycle for the Stirling engine. The difference in pressure during expansion and contraction causes the gas to perform net work over a cycle (green shaded area). **(c)** Proposed mechanical autonomous stochastic engine, consisting of two ribbons, main and secondary (displacements x_M and x_H respectively) and a cantilever (displacement x_W). **(d)** Thermal cycle for the proposed engine consisting of 4 steps: (i) x_w is at its leftmost position and energy flows from x_H to x_M (ii) M_w moves to the right ($\dot{x}_w > 0$), while x_M stays in a high energy state (iii) x_w is at its rightmost position, and energy flows from x_M to the cold bath (iv) x_w moves back to the initial position while x_M stays in a low energy state.

Stirling engines require a mechanism to heat and cool the working fluid in synchrony with the motion of the piston. In conventional engines this can be accomplished by a secondary internal piston (Fig. 4.1a) that displaces the fluid, placing it in contact with the hot and cold reservoirs. Prior implementations of the stochastic Stirling cycle used a laser to heat the working particle at pre-determined time intervals[29], making the engine nonautonomous. Our engine attains autonomous operation by utilizing the resonance responses of the two ribbons. Due to geometric nonlinearity, the resonance frequency of the main ribbon (f_M) depends on the position x_W of the cantilever (Fig. 4.2a), while the resonance frequency of the secondary, hot ribbon (f_H) is fixed. As a consequence, the overlap between the respective frequency responses (and therefore the energy transfer[252] between T_H and x_M), is controlled by the cantilever (Fig. 4.2b). By setting the frequency of the main ribbon below the frequency of the secondary ribbon, the maximum energy transfer between the hot bath

and the main ribbon occurs when the cantilever is at its leftmost position, as required by the thermal cycle (Fig 4.2b). Recent theoretical proposals in optomechanics utilize a similar mechanism to control the coupling between an optical resonator and a heat source [28, 253, 254].

This tension-mediated feedback mechanism introduces the synchronous heating and cooling required for thermal engine operation without the need of externally prescribed periodic temperature variations as in prior works[29, 183, 242]. The resulting changes in the main ribbon's vibrational energy can be seen in the probability distribution of its position, which is modulated by the cantilever motion (Fig. 4.2c). The modulation is maximal when the natural frequencies are chosen such that modulation sidebands of the main ribbon's motion coincide with a resonance peak of the coupled system. For weakly coupled ribbons, this condition is approximately $f_H - f_M \approx f_W$. In our experiments, f_M varies between 140 Hz and 190 Hz, f_H is 192.55 Hz and $f_W = 26.87\ Hz$ (see Supplementary Information).

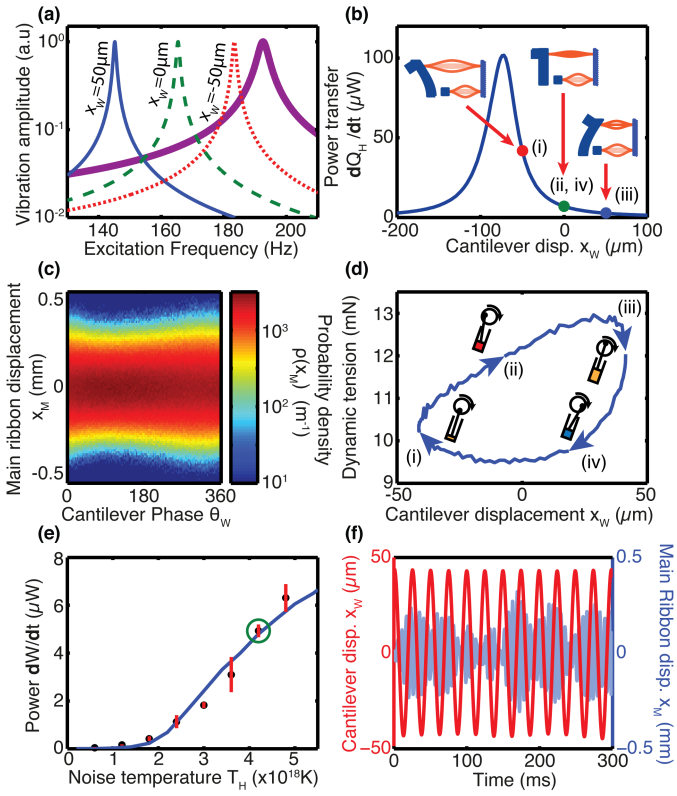

FIG. 4.2: *Thermal engine operation.* **(a)** Theoretical uncoupled frequency response of the main ribbon (x_M), for cantilever displacements x_W of $-50\ \mu m$ (blue, solid), $0\ \mu m$ (green, dashed) and $50\ \mu m$ (red, dotted). The uncoupled frequency response of the secondary ribbon x_H (thick purple) is shown for

comparison. **(b)** Theoretical energy transfer Q_H between the hot bath (applied to the secondary ribbon x_H) and the main ribbon (x_M), as a function of the cantilever displacement. The colored dots correspond to the curves in **(a)**. The roman numerals indicate the step of the thermal cycle associated to each displacement and energy transfer. **(c)** Experimental probability distribution of x_M as a function of the cantilever's oscillation phase, $\theta(\dot{x}_W, x_W)$. **(d)** Experimental force acting on the cantilever, as a function of the cantilever displacement. **(e)** Theoretical (blue line) and experimental (black dots) power transfer from the main ribbon to the cantilever as a function of the effective temperature of x_H. **(f)** Experimental time evolution of the cantilever (dark red) and ribbon (light blue). The green circle indicates the case $T_H = 4.2 \cdot 10^{18} K$, corresponding to the experimental conditions depicted in panels c, d and f.

Figure 4.2d shows the dynamic tension exerted by the main ribbon on the cantilever as a function of the cantilever's position. The dynamic tension was calculated from the measured probability distribution of the ribbon's position x_M using the equation $T = \gamma < x_M^2 >$, where $\gamma = 513\, kN/m^2$ quantifies the nonlinear coupling between the ribbon's tension and its bending stiffness. This quantity is analogous to the pressure-volume relation in a piston engine. The area inside the curve corresponds to the average work transferred to the cantilever per cycle of operation. This area has a value of $179.2 \pm 7.7\ nJ$, in good agreement with the average power dissipated in the cantilever, determined to be $171.2 \pm 7.1\ nJ$ per cycle from the quality factor and average vibrational amplitude. The power output increases nonlinearly with applied noise temperature (Fig 4.2e). At $T_H = 4.2 \cdot 10^{18} K$, its normalized value $P = 0.095 \pm 0.009\ k_b T_H s^{-1}$ is comparable to that of stochastic engines reported in the literature, whose values are around $0.02\ k_b T s^{-1}$[29] and $5\ k_b T s^{-1}$ [242]. The high effective noise temperatures in Fig. 4.2e are a consequence of the macroscopic dimensions of our tabletop setup, which mandate the use of an external noise excitation. In the Supplementary Information, we present simulations on a microscopic engine capable of attaining an output power above $12000\ k_b T s^{-1}$, owing to its high frequency of operation. While our table-top demonstration requires a significant amount of energy to simulate the high effective temperature T_H, the microscopic engine does not use any additional energy source besides the heat extracted from T_H.

During thermal machine operation, the trajectory of the cantilever is approximately a harmonic signal with a slowly varying envelope, while the motion of the ribbon is highly random (Fig 4.2f). We further investigate the properties of the cantilever motion by calculating the phase space probability distribution from the experimental measurements (Fig 4.3a) and theoretical simulations (Fig 4.3b). The cantilever's probability distribution is concentrated around a circular orbit, approximating harmonic motion with some amplitude and phase noise (in pure harmonic motion the probability density would be zero everywhere except in a circular, one-dimensional region). This probability distribution is non-passive: the amount of energy is not minimal given the entropy of the distribution. This allows for work extraction without a corresponding flow of entropy[177]. Additionally, the system presents a region of population inversion, with higher probability density around the circular orbit than close to the origin, where the energy is lowest. This distribution is similar to the theoretically predicted Wigner function for a quantum optomechanical heat engine[254], and contrasts with the passive Gaussian distribution describing harmonic oscillators subject to a white noise excitation[255]. We compare the phase space distribution during thermal machine operation (Figs. 4.3a and 4.3b) with that of a detuned system (i.e. where $f_H < f_M$, see Supplementary Information). In the detuned system, the main ribbon heating is out of sync with the phase of the cantilever oscillation cycle. This prevents thermal machine operation and results in a Gaussian phase space probability distribution for the cantilever, maximizing the entropy for a given mean energy (Figs. 4.3c and d).

We quantify the randomness of the cantilever's motion by calculating the entropy of its phase space probability distribution (Fig. 4.3e). The difference between the cantilever's entropy and the corresponding equilibrium entropy increases at high cantilever vibrational energies. This indicates the coexistence of two energy transfer mechanisms: An incoherent mechanism analogous to heat transfer[256], where fluctuations of the main ribbon introduce fluctuations on the ribbon's tension that cause the cantilever to move randomly, and a coherent mechanism where the motion of the main ribbon is modulated by the vibration of the cantilever. At low amplitudes (Fig. 4.3e and Supplementary Animation 1), or when the main ribbon frequencies are not tuned to result in thermal machine operation (Figs. 4.3c and 4.3d), the incoherent mechanism dominates, resulting in a maximally entropic (passive) probability distribution for the cantilever. At high amplitudes the coherent mechanism becomes

significant and the motion of the cantilever is nonpassive, with entropy below the maximal value (Fig. 4.3e). The Fourier transform of the cantilever velocity (Fig. 4.3f) reveals that its motion occurs mostly at the first mode of resonance. Higher cantilever modes and resonances of the ribbons are below the fundamental component by at least 80 dB. We attribute the presence of small quantities of harmonics to nonlinearities in our measurement system.

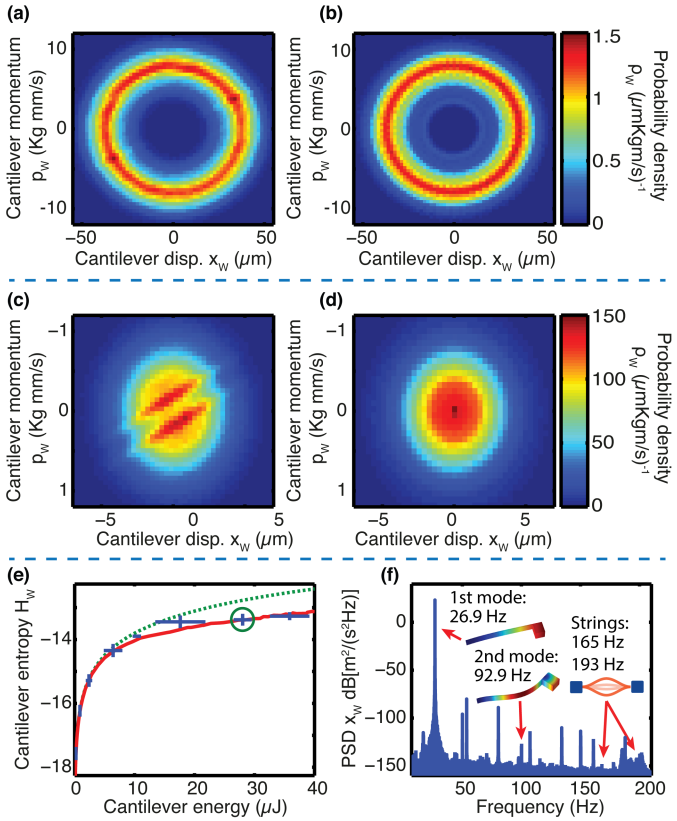

FIG. 4.3: *Properties of the cantilever motion*. **(a)** Experimental phase space probability distribution corresponding to the case when the frequency of the ribbons is tuned to achieve thermal engine operation at $T_H = 4.2 \cdot 10^{18} K$. **(b)** Theoretical phase space probability distribution for the experimental case in **(a)**. **(c)** Phase space probability density function for the cantilever in the detuned system (where $f_M > f_H$, see Supplementary Information for the exact values) at $T_H = 2 \cdot 10^{18} K$. **d** Theoretical prediction for the system in **(c)**. **(e)** Experimental entropy of the cantilever motion as a function of the energy (blue crosses), compared to a theoretical prediction (red line) and to the maximal entropy for the given energy (green dotted line). The green circle indicates the experimental conditions used in panels a, b and f, as well as Fig. 4.2c, d and f. **(f)** Fourier transform of the experimental cantilever motion.

The heat engine presented in this Letter corresponds to the mass-spring model in Fig. 4.4a and is described by the system of underdamped [257] Langevin [258, 259] equations (see supplementary information for derivation and numerical algorithms):

$$\begin{gathered} m_H\ddot{x}_H + b_H\dot{x}_H + k_H x_H + k_{HM}(x_H - x_M) + \mu x_H^3 = \xi_H \\ m_M\ddot{x}_M + b_M\dot{x}_M + (k_M - 2\gamma x_W)x_M + k_{HM}(x_M - x_H) + \mu x_M^3 = \xi_C \\ m_W\ddot{x}_W + b_W\dot{x}_W + k_W x_W - \gamma x_M^2 = \xi_W \end{gathered} \qquad \text{Eq. 1 a-c}$$

Here k_H, k_M and k_W are the stiffness of the hot ribbon, the main ribbon and the cantilever respectively, b_H, b_M and b_W are the corresponding linear damping coefficients and m_H, m_M, and m_W are the corresponding masses. The terms ξ_H, ξ_C and ξ_W represent the thermal noise introduced by the baths acting on each degree of freedom. These terms have a white noise power spectral density of $4K_B T_X b_X$ [142]. This relationship between dissipation, temperature and excitation force is used to determine the experimental effective temperature. In the numerical simulations, the temperature T_H is set to match the excitation used in the experiments, while T_C and T_W are set to zero (except otherwise indicated) since they are negligible in comparison to T_H. The constant k_{HM} represents the linear coupling between the two ribbons, γ is the nonlinear coupling between the main ribbon and the cantilever (also appearing in the ribbon's dynamic tension equation), and μ is the cubic nonlinear stiffness of the ribbons. Experimentally measured values for the all parameters are provided in the Supplementary Information. Coupled degrees of freedom subject to Brownian motion have been studied in electronic systems[256], and the asymmetric coupling between x_M and x_W appears in the description of phonon modes in superconductors[235].

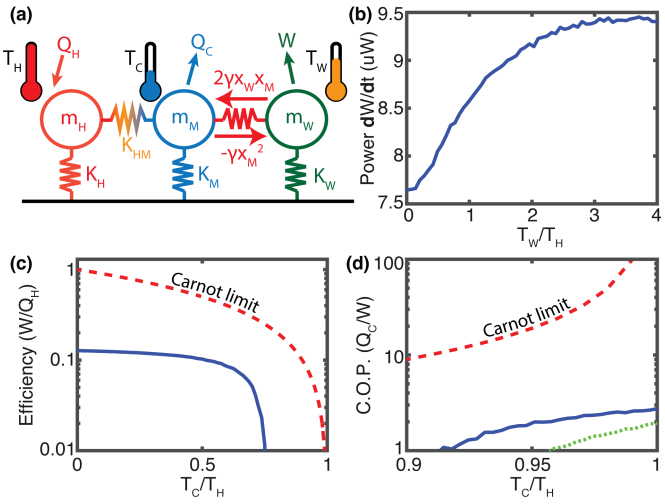

FIG. 4.4: *Theoretical investigation.* **(a)** Mass-spring model for the system. **(b)** Energy transfer as a function of the cantilever temperature T_W. **(c)** Efficiency of the thermal machine (blue, solid) and comparison with the Carnot efficiency (red, dashed). Here, the cantilever motion has been prescribed to be $x_W = (50\ \mu m)\cos(\omega_W t)$ to prevent incoherent energy transfer between the ribbons and the cantilever. **(d)** Refrigerator Coefficient Of Performance ($C.O.P. = Q_C/W$) when the cantilever is forced to oscillate at $A_W = 50\ \mu m$ (blue, solid) and when driven by noise at $T_W = k_W A_W^2/k_B$ (green, dotted). The red dashed line is the Carnot maximal C.O.P.

As demonstrated in Fig. 4.3, the theoretical model predictions are in good agreement with the experiments. Thus, we use the model to determine quantities that are not directly measurable in our experimental setup, such as the energy transfer between ribbons. We highlight the most relevant theoretical findings in Fig. 4.4. We define the power transfer between a degree of freedom and its thermal bath as the work of the thermal noise and damping: $\boldsymbol{dW_X/dt} =< (b_X\dot{x}_X - \xi_X)\dot{x}_X >$ [260] . We first study the effect of the cantilever thermal bath's temperature T_W. Increasing T_W increases the energy transferred between T_H and T_W (Fig 4.4a). This corresponds to an effective negative thermal conductivity. In addition, the system is able to transfer energy between the thermal baths T_H and T_W even when T_W is increased above T_H. This observation, which seems to defy the second law of thermodynamics, is made possible by the fact that x_M is at a lower temperature than x_H, and absorbs the excess entropy extracted from ξ_H. Figure 4.4c presents the efficiency of the thermal machine as a function of the ratio between T_H and T_C. The machine attains a maximum efficiency of approximately 30% of the maximal Carnot efficiency using our experimental, unoptimized parameters. In the Supplementary Information, we present

alternative designs that attain efficiencies up to 50% of the theoretical maximum. When the temperature ratio T_H/T_C is close to 1, the energy flow between T_H and T_C reverses, and the machine acts as a refrigerator [251]. The refrigerator regime requires a constant supply of energy to the cantilever. This energy can be provided by externally prescribing the cantilever displacement, or by increasing T_W to introduce large amplitude thermal motion in the cantilever. In the latter case, the main ribbon is cooled through the addition of heat to the system, which behaves as an absorption refrigerator [253, 261-264]. Figure 4d presents the efficiency of the refrigerator operation.

This work has demonstrated that a mechanical system consisting of two ribbons and a cantilever has the ability to act as a heat engine or refrigerator, and presents the unusual property of negative thermal conductivity. Traditionally, Brownian motion has been seen as an inconvenience when present in mechanical systems, e.g., by limiting the precision of nanomechanical sensors[265]. Our work demonstrates that this thermal noise may be a source of energy and a tool to study thermodynamics in both macro and micro scale systems.

Supplementary: Alternative heat engines

In the main paper it was demonstrated that a mechanical system can act as a stochastic heat engine by exploiting nonlinearity and resonance. The generality of this fundamental concept is explored in this section. We briefly discuss two alternative arrangements of masses and nonlinear springs that also function as heat engines.

Main-Cold engine

We first consider an engine similar to the engine that was discussed in the main paper (Fig. 4.S1a). The only difference is that the hot thermal bath is applied to the main ribbon instead of the secondary ribbon. For the engine to operate, the resonance frequency of the main ribbon must be above the natural frequency of the secondary, cold ribbon (Fig. 4.S1b).

The engine is described by the system of equations:

$$m_C\ddot{x}_C + b_C\dot{x}_C + k_C x_C + k_{CM}(x_C - x_M) + \mu x_C^3 = \xi_C$$
$$m_M\ddot{x}_M + b_M\dot{x}_M + (k_M - 2\gamma x_W)x_M + k_{CM}(x_M - x_C) + \mu x_M^3 = \xi_H \qquad \text{Eq. S1}$$
$$m_W\ddot{x}_W + b_W\dot{x}_W + k_W x_W - \gamma x_M^2 = \xi_W \qquad \text{A-C}$$

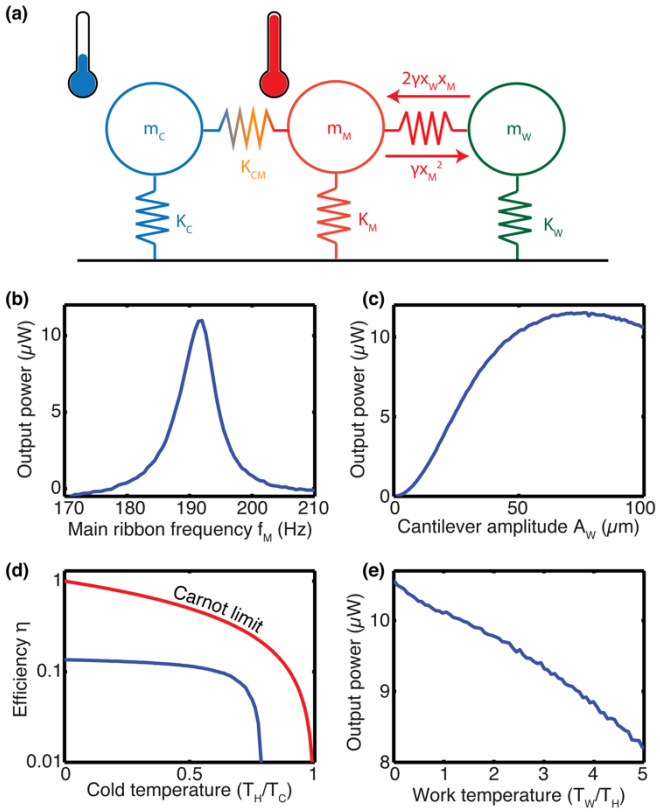

FIG. 4.S1: *Main-Cold engine* **(a)** Mass-spring diagram of the engine. **(b)** Output power as a function of the main ribbon's frequency, for a prescribed cantilever vibration amplitude of $50\ \mu m$. **(c)** Engine power as a function of the work amplitude ($dW/dt = < -\gamma x_M^2 \dot{x}_W >$). **(d)** Energy efficiency and comparison with the Carnot limit. **e** Power output as a function of the temperature acting on the cantilever. The parameters used in this simulation: $f_M = 190.8\ Hz, f_C = 165.37\ Hz, f_W = 26.87\ Hz,$ $m_M = m_C = 0.207g, m_W = 1.27\ Kg,\quad Q_C = 59.41,\quad Q_M = 167.78,\quad k_{CM} = 0.0381 \cdot k_C,\quad \gamma = 513\ kNm^{-2},\ \mu = 16.9\ MNm^{-3},\ T_H = 2 \cdot 10^{18}K,\ T_M = T_C = 0,\ A_W = 50\ \mu m$ (unless otherwise indicated).

The efficiency and output power of this engine are similar to those obtained in the main paper (Fig. 4.S1 c-d), where the hot bath was applied to the secondary ribbon. This engine is also capable of pumping energy from a cold thermal bath to a hot thermal bath (Fig. 4.S1e).

However, in contrast with the engine presented in the main paper, in this case an increase in the cantilever temperature decreases the power transferred to x_W.

Hot-Main-Cold engine

We can build engines with higher efficiency and output power by adding an additional ribbon (Fig. 4.S2a). In this case, the main ribbon (x_M) is attached to two ribbons. One of them (x_H) is in contact with the hot thermal bath, while the other (x_C) is in contact with the cold thermal bath. For maximum efficiency, the hot ribbon's natural frequency should be tuned above the frequency of the main ribbon, while the cold ribbon's natural frequency has to be set below the frequency of the main ribbon (Fig. 4.S2b). This system is described by the system of equations:

$$\begin{gathered} m_H\ddot{x}_H + b_H\dot{x}_H + k_H x_H + k_{HM}(x_H - x_M) + \mu x_H^3 = \xi_H \\ m_C\ddot{x}_C + b_C\dot{x}_C + k_C x_C + k_{CM}(x_C - x_M) + \mu x_C^3 = \xi_C \\ m_M\ddot{x}_M + b_M\dot{x}_M + (k_M - 2\gamma x_W)x_M + k_{CM}(x_M - x_C) + k_{HM}(x_M - x_H) + \mu x_M^3 = \xi_M \\ m_W\ddot{x}_W + b_W\dot{x}_W + k_W x_W - \gamma x_M^2 = \xi_W \end{gathered} \qquad \text{Eq. S2 A-D}$$

Figure 4.S2c shows the power output ($\dot{W} =< F\dot{x} >=< -\gamma x_M^2 \dot{x}_W >$) as a function of the prescribed cantilever vibration amplitude. The relation between cantilever amplitude and output power is similar to that obtained for the Cold-Main engine of the previous section and the Hot-Main engine of the main paper, where a nonlinear increase in output power is observed. In this case, however, the saturation occurs at higher amplitudes, and the output power is larger by a factor of more than two (Compare Figs 4.S1c and 4.S2c).

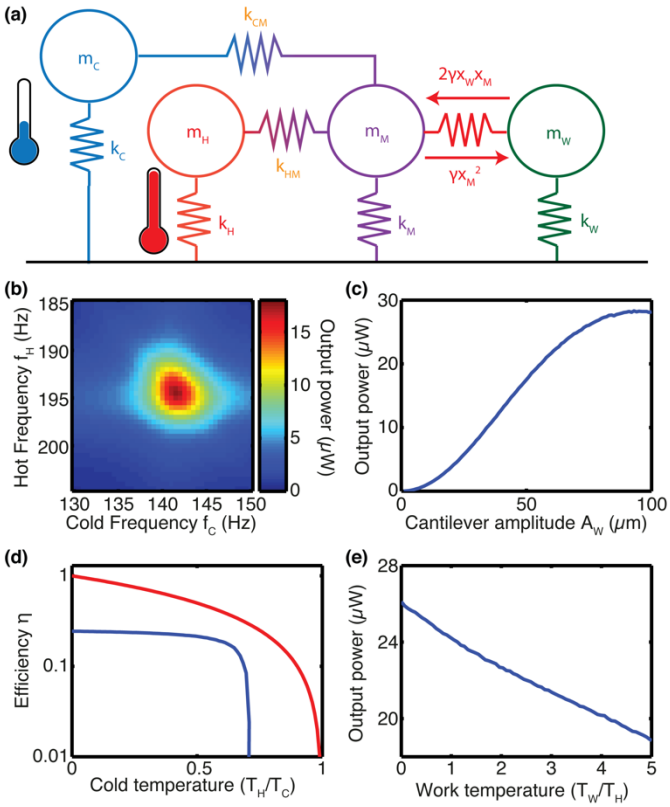

FIG. 4.S2: Hot-Main-Cold engine. **(a)** Mass-spring diagram of the engine. **(b)** Engine efficiency as a function of the cold spring stiffness. **(c)** Engine power as a function of the work amplitude. **(d)** Energy transfer as a function of the work temperature. **(e)** Efficiency in the nonautonomous limit. The parameters used in this simulation are: $f_H = 194.5\ Hz$, $f_M = 165.37\ Hz$, $f_C = 141.5\ Hz$, $f_W = 26.87\ Hz$, $m_H = m_M = m_C = 0.207g, m_W = 1.27\ Kg$, $Q_H = Q_C = 59.41$, $Q_M = 1000$, $k_{CM} = k_{HM} = 0.0381 \cdot k_C$, $\gamma = 513\ kNm^{-2}$, $\mu = 16.9\ MNm^{-3}$, $T_H = 2 \cdot 10^{18}K$, $T_M = T_C = 0$, $A_W = 50\ \mu m$ (unless otherwise indicated).

In addition to an increase in power, this design also brings an increase in efficiency (Figs. 4.S2c and d). This efficiency reaches a maximum of 47% of the Carnot limit, which is significantly higher than the efficiency of the two-ribbon engines (about 30%). As in the previous two cases, the engine is able to transfer energy from cold to hot temperatures (Fig 4.S2e).

Supplementary: Equations of motion for the ribbon-cantilever system

Our system consists of two pieces of metal ribbon (x_M and x_H) and a cantilever (x_W). In this section we derive the coupled equations of motion for the system (Eq. 1 of the main paper) as a function of the geometry.

Cantilever equation

The motion of the cantilever can be described by considering only the first bending mode of vibration. This is a consequence of the fact that higher modes of vibration are much stiffer and therefore vibrate at smaller amplitudes. This assumption is confirmed experimentally by inspecting the Fourier transform of the cantilever motion (Fig 4.3f of the main paper). Under this assumption, the dynamics of the cantilever are described by a damped-driven harmonic oscillator:

$$m_W \ddot{x}_W + b_W \dot{x}_W + k_W x_W = T\,(x_M) \qquad \text{Eq. S3}$$

where m_W, b_W and k_W are the effective mass, damping and stiffness, respectively, of the normal mode with position x_W. The right hand side sums the external forces acting on the mode. In our experimental system, the only external force acting on the cantilever is the ribbon tension, which we represent by T. The value of T is a function of the ribbon's in-plane vibrational displacement x_M (We will obtain an expression for $T(x_M)$ in the *Ribbon equation* section). The variable x_W represents the position of the normal mode at a particular instant of time. As such, it can be defined in different ways depending on the mode's normalization. In this derivation, we set the mode normalization that makes the modal coordinate x_W coincide with the displacement of the cantilever at the point where the ribbon is attached. We calculate the effective mass and stiffness using the commercial Finite Element Method (FEM) package Comsol Multiphysics®. The motion of the cantilever must take into account the longitudinal stiffness of the ribbon. We use a value of $31.55\ kN/m$ that correctly reproduces the measured cantilever frequency, as described in the section *Experimental determination of the quality factors, frequencies and coupling constant,* where we will also determine the damping constant b_W.

The effective mass is defined as the integral $\int_V \rho(x,y,z)(u^2+v^2+w^2)dV$ where u, v and w represent the displacements of the mode along the directions x, y and z respectively, while ρ is the density of the cantilever material. This provides us with a cantilever mass of $1.27 \pm 0.04\ kg$, where the uncertainty originates from tolerances in the geometry measurement. The effective stiffness can be calculated from the eigenfrequency using the equation $k = m\omega^2$.

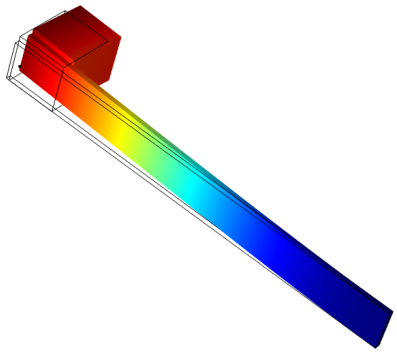

FIG. 4.S3: *Cantilever's first normal mode of vibration.* We use this mode profile to calculate the effective mass of the cantilever (m_w in our system of equations). The cantilever has a length of 40.6 cm, a height of 4 cm and a thickness of 5 mm. The block mass at the cantilever's end has dimensions of 5x5x6 cm. The cantilever is made of steel with a Young's modulus $E = 200\ GPa$, a Poisson ratio $\nu = 0.33$ and a density $\rho = 7850\ Kg/m^3$.

Ribbon equation

The motion for a beam-like resonator can be approximated by the Woinowski-Krieger equation[266]. This equation is a modified Euler-Bernoulli equation that takes into account the effect of the vibration-induced tension. The Woinowski-Krieger equation for a slender beam of length L takes the form:

$$EI\frac{\partial^4 w}{\partial y^2} - \frac{EA}{L}\left(\Delta y + \Delta y_0 + \frac{1}{2}\int_0^L \left(\frac{\partial w}{\partial y}\right)^2 dy\right)\frac{\partial^2 w}{\partial y^2} + \rho A\frac{\partial^2 w}{\partial t^2} - f(y,t) = 0 \qquad \text{Eq. S4}$$

Here, ρ is the density of the ribbon, A is the cross-section area, I is the bending moment of inertia, and E is the Young's modulus. The y axis corresponds to the direction along the length of the ribbon, and w is the deflection. Δy_0 is the elongation of the ribbon when the cantilever is at equilibrium. The displacement of the cantilever from its equilibrium position introduces a Δy change in the length of the ribbon.

At small amplitudes, the Woinowski-Krieger's nonlinear term (represented by the integral in Eq. S4) vanishes. In this regime, the system behaves like an Euler-Bernoulli beam in which case it would be reasonable to define a set of vibrational modes for the ribbon. It is possible to extend the range of validity of this picture to higher amplitudes by first performing a modal decomposition and then using the Galerkin method to account for the nonlinear effects[158]. This approach is valid as long as the amplitude is small enough to ensure that the mode profile is not significantly affected by the nonlinearity. Here we use this method to derive a nonlinear equation for the motion of the first mode of vibration for the ribbons. We follow the same approach as Postma et al. [158]. This approach consists in expressing the solution of Eq. S4 as a time-dependent linear combination of trial functions:

$$w(y,t) = \sum_{i}^{n} u_i(t)\phi_i(y) \qquad \text{Eq. S5}$$

In general, a finite set of trial functions will not be able to exactly satisfy Eq. S4. This implies that the left hand side of the equation will not be identically zero. Instead, there will be an error term $\epsilon(x,t)$:

$$EI\frac{\partial^4 w}{\partial y^2} - \frac{EA}{L}\left(\Delta y + \Delta y_0 + \frac{1}{2}\int_0^L \left(\frac{\partial w}{\partial y}\right)^2 dx\right)\frac{\partial^2 w}{\partial y^2} + \rho A\frac{\partial^2 w}{\partial t^2} - f(y,t) = \epsilon(y,t) \qquad \text{Eq. S6}$$

The Galerkin method imposes the condition that the error term should be orthogonal to each of the trial functions. Orthogonality between $\epsilon(x,t)$ and $\phi_i(x)$ is defined as:

$$\int_0^L \phi_i(t)\epsilon(y,t)\,dy = 0 \qquad \text{Eq. S7}$$

The system is completely determined because there are as many orthogonality conditions as unknown functions $u_i(t)$. We use the eigenmodes of the linear system as test functions $\phi_i(y)$, and we consider only the first normal mode of vibration. This assumption is reasonable since higher order modes are considerably stiffer, and therefore oscillate at much smaller amplitudes. Applying the orthogonality condition (Eq. S7) to Eq. S6 results in the following ordinary differential equation describing the time evolution of the mode coordinate u_1 (Henceforth referred to as u):

$$m\ddot{u} + ku + 2\gamma\Delta u + \mu u^3 = F(t) \qquad \text{Eq. S8}$$

The term $2\gamma\Delta u$ is responsible for the coupling between the cantilever and the ribbon. The parameters in Eq. S8 are given by:

$$m = \rho A \int_0^L \phi^2(y)dy \qquad k = EI \int_0^L \frac{\partial^4 \phi(y)}{\partial y^4}\phi(y)dy + 2\beta\Delta y_0 \qquad \text{Eq. S9 A-D}$$

$$2\gamma = -\frac{EA}{L}\int_0^L \frac{\partial^2 \phi(y)}{\partial y^2}\phi(y)dy \qquad \mu = \gamma \int_0^L \left(\frac{\partial \phi(y)}{\partial y}\right)^2 dy$$

In order to evaluate these expressions, we calculate the mode profile $\phi(y)$ using the pre-stressed eigenfrequency analysis function of Comsol Multiphysics® 5.0. We use the plate model to describe the dynamics of the ribbon. In the finite element simulation, we select an elongation $\Delta x_0 = 250\mu m$ that yields resonance frequencies that are comparable to the experimental values. The thickness of the beams is set to $16.25 \pm 1.83\ \mu m$ in order to reproduce the longitudinal stiffness of $31.55 \pm 1.04\ kN/m$ that yields the correct cantilever resonance frequency, assuming a density $\rho = 8500\ kg/m^3$ and a Young's modulus $E = 115 \pm 10\ GPa$. The integration in Eq. S9a-d is performed along the central axis of the beam. For convenience, we fix the normalization of the mode to be:

$$\int_0^L \phi^2(y)dy = L \qquad \text{Eq. S10}$$

This definition sets the effective mass $m = \rho AL$ equal to the physical mass of the ribbon. The values of the parameters corresponding to our experiment are given in Table S1:

Parameter	Value
m	$0.207 \pm 0.023\ g$
$\boldsymbol{\gamma}$	$513 \pm 56\ kN/m^2$
$\boldsymbol{\mu}$	$16.9 \pm 1.8\ MN/m^3$

Supplementary Table 1: Ribbon effective mass and nonlinear parameters.

We will calculate the value of Δy_0 and k from the frequency response in the section *Experimental determination of the quality factors, frequencies and coupling constant.*

Coupling between ribbons

The coupling between x_H and x_M is implemented by a small piece of ribbon placed between the two resonators. The coupling is assumed to be linear, and modeled with a term $F = k_{HM}(x_H - x_M)$. We will experimentally measure the value of k_{HM} in the following section.

Supplementary: Experimental determination of the quality factors, frequencies and coupling constant

The previous section describes a model for the system that is based on analytical and finite element simulations. These methods are adequate to predict several of the system parameters. In this section we experimentally measure the remaining system parameters that cannot be accurately predicted with theoretical models.

Cantilever frequency and quality factor

We measure the cantilever by exciting it using a harmonic signal and measuring the frequency response. The excitation is provided by a solenoid that induces a force on a small magnet attached to the cantilever. The frequency response is extracted using a Lock-In amplifier that receives the signal from a Laser Doppler Vibrometer. Figure 4.S4 shows the measured

frequency response and the corresponding fit using the MATLAB® state space parameter estimation function. The fit yields a cantilever resonance at 26.87 ± 0.01 Hz with a quality factor of 964 ± 41.

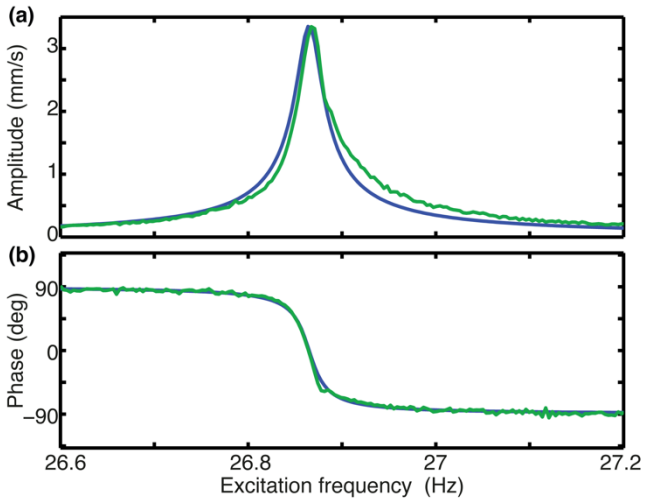

FIG. 4.S4: *Cantilever's frequency response.* **(a)** Amplitude of the cantilever's velocity as a function of the excitation frequency. **(b)** Phase of the cantilever's velocity as a function of the excitation frequency. The green lines represent measured values, while the blue lines represent the fitted response.

Ribbon's resonance frequencies, couplings and damping

In this section, we determine the experimental quality factor, frequency and coupling stiffness for the ribbons. We accomplish this by measuring the frequency response of the ribbon when excited by a harmonic signal of variable frequency. The results are fitted using MATLAB® state space parameter estimation.

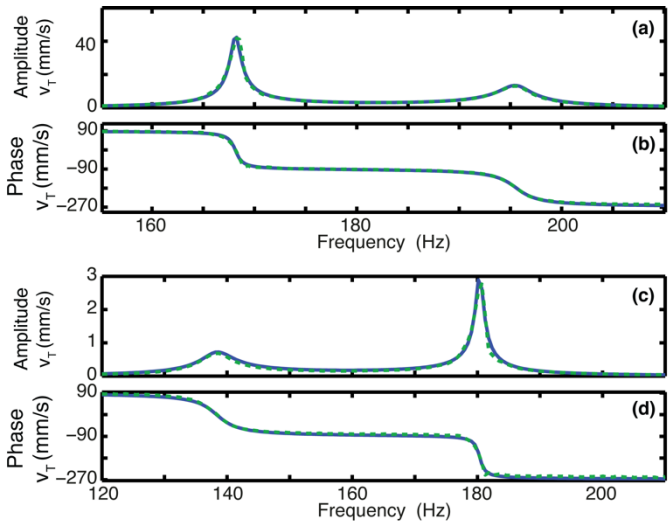

FIG. 4.S5: *Ribbon frequency response measurement.* **(a) and (b):** Ribbon amplitude (**a**) and phase (**b**) as a function of the excitation frequency, for the case where the ribbon tensions are tuned to result in thermal machine operation (Fig. 4.3 **a**, **b**, **d**, **e** in the main paper). **(c) and (d):** Amplitude **(c)** and phase **(d)** as a function of the excitation amplitude for the case where the ribbon are detuned so thermal machine operation does not occur (Fig. 4.3 **c**, **d** in the main paper). In all four panels, the dashed green line represents the experimental data and the solid blue line represents the fitted response.

The state space parameter estimation results are given in Table S2.

Parameter	Value (Tuned)	Value (Detuned)
f_H	$192.55 \pm 0.02\ Hz$	$134.32 \pm 0.04\ Hz$
f_M	$165.37 \pm 0.02\ Hz$	$176.67 \pm 0.02\ Hz$
Q_H	59.3 ± 1.8	26.9 ± 1.2
Q_M	167.8 ± 3.0	151.7 ± 2.0
k_{HT}/k_M	0.0381 ± 0.0059	0.0381 ± 0.0060

Supplementary Table 2: Ribbon parameters.

We attribute the large differences between Q_H and Q_M this to eddy current losses in the ribbon due to the large magnetic fields used for excitation.

Supplementary: Methods

Numerical methods

We simulate the system by expressing the equations of motion in Itô form:

$$
\begin{aligned}
dx_H &= v_H \cdot dt + 0 \cdot dW_1 \\
dx_M &= v_M \cdot dt + 0 \cdot dW_2 \\
dx_W &= v_W \cdot dt + 0 \cdot dW_3 \\
dv_H &= -\frac{1}{m_H}\left(b_H v_H + k_H x_H + k_{HM}(x_H - x_M)\right) \cdot dt + \sqrt{2k_B b_H T_H} \cdot dW_4 \\
dv_M &= -\frac{1}{m_M}\left(b_M v_M + (k_M - 2\gamma x_W)x_M + k_{HM}(x_M - x_H)\right) \cdot dt + \sqrt{2k_B b_M T_M} \cdot dW_5 \\
dv_W &= -\frac{1}{m_M}(b_W v_W + k_W x_W - \gamma x_M^2) \cdot dt + \sqrt{2k_B b_W T_W} \cdot dW_6
\end{aligned}
\qquad \text{Eq. S11 A-F}
$$

In this system, the terms m_H, m_M, m_W, k_H, k_M, k_W, k_{HM}, b_H, b_M, b_W and γ have the same meaning as in Eq. S1 in the main paper. The excitation temperature in the simulations was fitted in order to reproduce the experimental results. This also required adjusting the natural frequency of the secondary ribbon by $+0.5\,Hz$. The vector dW represents the thermomechanically induced velocity change incurred during the time interval dt, and has a Gaussian distribution.

The Gaussian-distributed random numbers were obtained using a Mersenne-Twister uniform random number generator and the Beasley-Springer-Moro inversion formula. We simulated the time evolution of the system using a stochastic Runge-Kutta algorithm with strong order 1.5[195] implemented in C++, which ran on the ETH Euler cluster. Statistical quantities such as the RMS velocities were averaged over an interval of 5000 s, using a time step of $3\ \mu s$ for all the figures except the microscopic engine. The microscopic simulations use a time step of $60\ ps$ and an averaging time of $0.1\ s$.

Experimental materials and methods

We measured the cantilever motion using a Polytec Laser Doppler Vibrometer (LDV), model OFV-503 with a decoder model OFV-3001 placed at an angle of 45° (Fig. 4.S6a). For the ribbon, we used a Polytec LDV model OFV-505 with a decoder model OFV-5000, pointing at $L =$

$14.1\ cm$ along the length of the ribbon. We calculated the modal amplitude from the measured velocity by using the mode profile function obtained from finite element simulation. The sensitivity of the lasers was set to $125\ mms^{-1}V^{-1}$ for the cantilever and $200\ mms^{-1}V^{-1}$ for the ribbon. We digitized the signal from the lasers for a length of 2000s of $2.5\ ksamples/s$ using a Tektronix™ oscilloscope model DPO-3034 in high-resolution mode. We calculated the displacements of the cantilever and ribbon by low-passing the velocity signal to remove any DC component and then integrating the resulting signal using the MATLAB® cumtrapz function. The cutoff frequencies for the high-pass filter were selected at 5 Hz for the cantilever and 60 Hz for the ribbons.

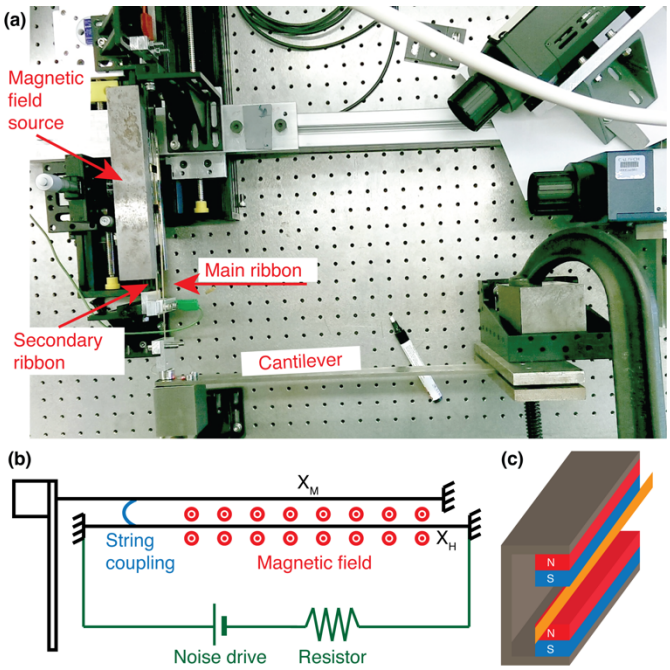

FIG. 4.S6: *Experimental setup.* **(a)** Picture of the experimental setup with the two ribbons and the cantilever. **(b)** Schematic diagram of the experimental setup including the noise excitation. **c** Steel structure and magnets used to apply a noise excitation to the secondary ribbon.

We implemented the ribbons by cutting a sheet of brass obtained from Brütsch-Rügger™ (Catalog number 162950.0110) with a nominal thickness of $20 \pm 2\ \mu m$ into two stripes of height $H = 5\ mm$ and length $L = 50\ cm$. The free length the ribbons (after clamping) was $L_R = 30\ cm$. We placed the two ribbons at a distance of $8\ mm$ and introduced a coupling between them by soldering an additional strip of brass at both ribbons at length $L_C = 6\ cm$ along their length (Fig. 4.S6b).

We introduced the noise excitation on the secondary ribbon by placing it under a magnetic field implemented with 12 neodymium magnets from Supermagnete™ catalog number Q-40-10-05-N enclosed in a C-shaped steel bar (Fig. 4.S6c). We circulated the noise current across the ribbon by driving both ends from a Topping TP22 amplifier in series with a 5.5 Ohm power resistor. The noise signal driving the ribbon was obtained by generating a sequence of normally distributed random numbers, which was subsequently lowpassed using an 8^{th} order Low-Pass filter with a cutoff frequency of 10 KHz. The electrical signal was generated with the sound card of a MacBook laptop using Apple™ CoreAudio library. The Fourier transform of the amplified signal revealed that the noise spectrum was flat on the region of interest between 50 Hz and 300 Hz.

Determination of statistical quantities and errors

We calculated the histograms in Figure 4.2d and Figure 4.3 a-d by binning the time series data from the numerical simulations into a two-dimensional histogram with 128x128 bins. We calculated the entropies from the histograms using the definition:

$$H = \int_{\Gamma} \rho(x_W, p_W) \log \rho(x_W, p_W)\, dx_W dp_W \qquad \text{Eq. S12}$$

Where Γ is the phase space of the cantilever, x_W is the cantilever position and p_W is the cantilever momentum. The statistical uncertainties associated to each time series measurement were calculated by dividing the measured time series in 8 sub-sequences of equal length. We then evaluated the variance of the measured quantities in the 8 sub-sequences and utilized this value to extrapolate the uncertainty of our measurement.

Supplementary: Microscopic heat engine operating on thermal fluctuations

The experimental thermal engine that we have presented in this paper requires an external noise source to simulate a large temperature and therefore obtain significant amounts of Brownian motion. This is a consequence of the engine's macroscopic size, since Brownian motion in a meter-sized steel structure is extremely small. The goal of this section is to demonstrate that it is possible to implement engines producing measurable amounts of work at experimentally accessible temperatures (~200ºC) by miniaturizing the ribbons and the cantilever. The dimensions of our microscopic engine are experimentally feasible, and we base our simulations in parameters obtained from the literature, corresponding to actual experimental devices.

We model the cantilever using a diamond (Young's modulus $E_C = 960\ GPa$ and density $\rho_C = 3500\ Kg/m^3$) beam of length $L_C = 20\ \mu m,$ width $w_C = 880\ nm$ and height $h_C = 370\ nm$, with a quality factor $Q_C = 47800$ (See [267] for details on the geometry, quality factor and fabrication process). The ribbons are made with graphene and have a length $L_R = 2.7\ \mu m$, width $w_R = 20\ nm$, thickness $t_R = 3\ nm$ and quality factor $Q_R = 35$. Graphene ribbons with this geometry can be modeled using conventional finite element theory or beam theory (See Fig. 2d in Ref. [268]), using a Young's modulus of $E_R = 1\ TPa$ and a density $\rho_R = 2200\ kg/m^3$.

The main ribbon is attached to the cantilever at a distance $x_a = 2.9\ \mu m$ from the cantilever's supporting end (Fig. 4.S7a). This is because the longitudinal stiffness of the ribbon is very high and would place an excessive load to the cantilever if it were attached at the end. The equations of motion for the microscopic system are:

$$\begin{aligned} m_H\ddot{x}_H + b_H\dot{x}_H + k_H x_H + k_{HT}(x_H - x_T) + \mu x_H^3 &= \xi_H \\ m_M\ddot{x}_M + b_M\dot{x}_M + (k_M - 2\gamma_0\phi(x_A)x_W)x_M + k_{HM}(x_M - x_W) + \mu x_C^3 &= \xi_C \\ m_W\ddot{x}_W + b_W\dot{x}_W + k_W x_W - \gamma_0\phi(x_A)x_M^2 &= \xi_W \end{aligned} \qquad \begin{matrix} \text{Eq. S13} \\ \text{A-C} \end{matrix}$$

Where x_W represents the displacement of the cantilever at $x = L_C$, $\phi(x_a)$ is the cantilever's first bending mode profile, evaluated at the attachment point of the ribbon. The ribbon's

nonlinear parameter γ_0 can be computed using Eq. S9, and all the other symbols have the same meaning as in Eq. 1 of the main text. Equation S13 can in fact be reduced to Eq. 1 by defining $\gamma = \gamma_0 \phi(x_A)$. This definition provides us with a mechanism to adjust the value of γ when designing a device.

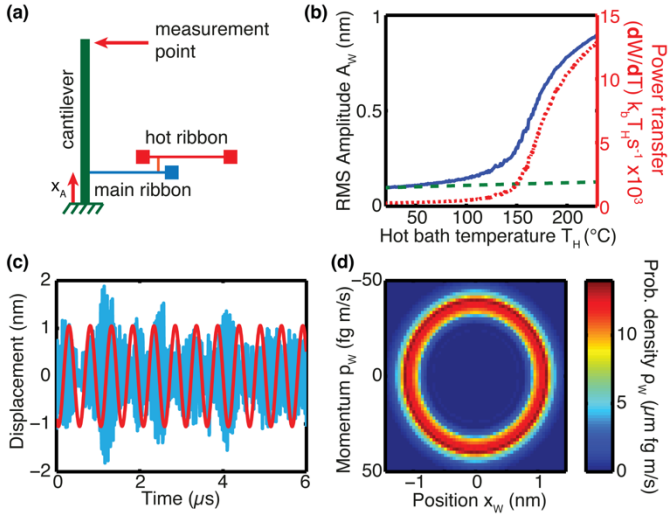

FIG 4.S7: *Microscopic engine.* **(a)** Schematic diagram of the engine, with the hot ribbon attached at a distance x_A from the cantilever's support. **(b)** Cantilever's vibration amplitude as a function of the hot thermal bath temperature T_H (blue, solid) compared to the thermomechanical amplitude of the cantilever at T_H (green, dahsed). The red dotted line is the output power, which reaches a maximum value of $12810\ k_B T_H s^{-1}$ at 230 °C. **(c)** Example of a cantilever's trajectory (red) and a graphene nanoribbon's trajectory (light blue). **(d)** Phase space probability distribution for the cantilever, showing a distinctively nonpassive circular shape.

Figure 4.S7b presents a simulation of the thermal machine's cantilever amplitude as a function of the hot thermal bath temperature. In all simulations, both the cold bath temperature T_C and the cantilever's temperature T_W are set to 20 °C. The RMS value of the cantilever's displacement x_W is much larger than it can be attributed to thermomechanical noise. If the cantilever's temperature were to raise to $T_H = 180$°C due to direct conduction from the cold bath, the thermomechanical noise would still be more than 6 times smaller than the simulated vibration amplitude. At a temperature $T_W = 180$°C, the cantilever reaches a peak amplitude of $1\ nm$ (Fig 4.7c). This motion can be measured experimentally at very high resolution (See Fig. 3 in Ref. [267]). Therefore, the thermal machine effect should be observable in a system of these dimensions. Due to its high operating frequency, the

proposed engine is capable of producing an output power orders of magnitude above that of prior works.

We have shown that a microscopic autonomous thermal engine can produce a detectable amount of power. Our calculations use realistic parameters obtained from the literature. However, constructing a device with these properties is challenging and our description omits some technical aspects: Precisely controlling the attachment point of a graphene ribbon is a hard nanofabrication problem. In addition, the device requires a mechanism to heat the hot ribbon, and to tune the frequency response. The heating can be accomplished by passing a current through the ribbon, or by utilizing thermally conductive electrodes. The frequency tuning may be accomplished by imposing a static deflection on the cantilever by means of an electrostatic potential. Finally, the required quality factors are high. This latter aspect can be mitigated by numerically optimizing the design (Or switching to a more powerful alternate engine such as the one discussed in Fig. 4.S2). Increasing the temperature while decreasing the operating amplitude and stiffness of the cantilever will also result in a relaxed quality factor requirement.

System parameters

The parameters used for the numerical simulations of the microscopic engine are given in Table S3.

Parameter	Value
f_M	$27.203\ MHz$
f_M	$30.195\ MHz$
γ	$4.47 \cdot 10^7\ N/m^2$
μ	$1.8 \cdot 10^{14}\ N/m^3$
$m_H = m_M$	$3.56 \cdot 10^{-19}\ Kg$
m_W	$2.85 \cdot 10^{-15}\ Kg$
k_{HM}	$0.0938\ k_M$
Q_W	47800
$Q_H = Q_M$	35

Supplementary Table 3: Microscopic engine parameters.

These parameters have been obtained using the same procedure that we described in the section *Equations of motion for the ribbon-cantilever system*. The FEM simulations on the cantilever account for the stiffness of the ribbon by using a spring foundation at the ribbon attachment point. The ribbon's frequencies require a tension of $2.2\ nN$ for the main ribbon and $2.9\ nN$ for the hot ribbon.

Designing perturbative metamaterials from discrete models: From Veselago lenses to topological insulators

Kathryn Matlack[+], Marc Serra-Garcia[+*], Sebastian D. Huber, Chiara Daraio.

+The authors contributed equally to the work
*e-mail: sermarc@ethz.ch

This work is currently under review in Nature Materials.
Copyright will be owned by the publisher upon acceptance.

Abstract

Discrete models provide concise descriptions of complex physical phenomena, such as negative refraction, topological insulators, and Anderson localization. While there are multiple tools to obtain discrete models that demonstrate particular phenomena, it remains a challenge to find metamaterial designs that replicate the behavior of desired nontrivial discrete models. Here we solve this problem by introducing a new class of metamaterial, which we term "perturbative metamaterial", consisting of weakly interacting unit cells. The weak interaction allows us to associate each element of the discrete model (individual masses and springs) to individual geometric features of the metamaterial, thereby enabling a systematic design process. We demonstrate our approach by designing 2D mechanical metamaterials that realize Veselago lenses, zero-dispersion bands, and topological insulators. While our selected examples are within the mechanical domain, the same design principle can be applied to acoustic, thermal, and photonic metamaterials composed of weakly interacting unit cells.

Introduction

Metamaterials utilize sub-wavelength structures to control wave propagation, achieving extreme functionalities such as focusing beyond the diffraction limit[4, 269-272], performing mathematical operations with light[273], or cloaking objects[8, 274]. While the potential of metamaterials is well established, we lack systematic approaches to metamaterial discovery, which is currently based on intuition, trial and error, or unguided searches of large design spaces. Data-driven design approaches[275-277] have been successful in engineering quasi-static material performance, but extending them to dynamics requires taking into account the interactions between multiple vibrational modes of the unit cell. A promising approach towards metamaterial design in the dynamic regime draws inspiration from the field of electronics[204, 278, 279], where complex devices are designed by combining discrete "lumped" elements, such as capacitors or inductors. These lumped elements are able to capture the intended behavior independently of the implementation details of the elements, which greatly simplifies the design process. Once a phenomenon has been described as a lumped element model, it can be easily implemented in different domains. In the mechanical domain the capacitors and inductors can be replaced by masses and springs, and implemented in platforms as diverse as pendulum arrays[31] or networks of piezoelectric resonators[280]. While it is possible to implement lumped models by combining discrete masses, springs, capacitors or inductors, there is currently no systematic design process to convert these models to metamaterials. This is because the space of possible designs is extremely large, and the relationship between a structure and its dynamical properties is highly non-trivial.

We propose a generic tool to solve this inverse problem: we map building blocks of a metamaterial to components of a mass-spring model, and determine the metamaterial design by searching the space of possible combinations of building blocks. In order for this approach to be successful, we need to address two key challenges. First, we need an efficient algorithm to extract a reduced order model from the metamaterial design. Second, we need a system where changes to different parts of the design do not interfere with each other, such that the design elements are additive in their effect. This additive property allows us to divide

the search space into much smaller independent sub-spaces, resulting in an exponential speedup of the search process.

In this paper we successfully address these two challenges with "perturbative metamaterials": systems consisting of unit cells with a spectrum of linear normal modes that weakly interact with modes of neighboring unit cells. We obtain reduced-order models for our metamaterial through a method adapted from quantum material science: we use the Schrieffer-Wolff transformation[19, 281] to isolate modes in the frequency range of interest. The purpose of extracting reduced order models is to efficiently quantify how design changes affect the material's dynamic properties. We then catalogue these changes for various geometries, and optimize the configuration of the metamaterial's components to obtain the target mass-spring model. We show that with a suitable series expansion of the Schrieffer-Wolff transformation, we can explore a space containing on the order of 10^{30} design configurations, which is impossible to do using optimization methods with current computational power. We demonstrate this in a system of plates connected by soft beams, which achieves the additive property essential for an effective algorithm.

We show the potential of our generic scheme on three key examples: a Veselago lens, a zero group velocity material, and a topological insulator, each with increasing complexity in their unit cell designs.

Extracting a reduced order model from a perturbative metamaterial

Here we present a method to extract a reduced order model for a given metamaterial design (e.g., Fig. 5.1a), which is a pre-requisite for our design procedure. The method works for arbitrary unit cells as long as they interact weakly. We start by selecting the frequency range where the model will be valid. Each unit cell mode that falls within that range (Fig. 5.1b) translates to a degree of freedom in the reduced-order model. Our reduced order model calculation (Fig. 5.1a-c) differs from existing reduction techniques[282-284] [285-288] in that it constructs an approximation of a complex metamaterial geometry by combining results obtained by considering geometric features individually. This property is crucial when

designing metamaterials from discrete models. We explain our method using a system of square lattice of steel plates (10mm x 10mm x 0.5mm) weakly interacting through soft, polymer beams. The plates can also contain holes that tune the local resonance frequencies. We emphasize that this system is chosen as an example, and our method can be applied to any metamaterial that satisfies the weak interaction condition.

The reduced-order models are based on a local modal expansion and consist of local resonators coupled through springs. Each local resonator corresponds to a plate mode that falls within our frequency range of interest, and the springs account for the coupling introduced by the beams. We refer to a system of plates without beams as "uncoupled", and a system of plates connected with beams as "coupled" (Fig. 5.1b,c). For clarity, we define two separate coupling terms: V is the coupling between modes in the full physical system, V^R is the coupling in the reduced-order model that we extract.

Assuming the beams are short enough such that we can consider their effect as instantaneous and neglect their internal degrees of freedom (DOFs), the equation of motion of the coupled system is:

$$\ddot{u} + ([M + \Delta M]^{-1}[K + \Delta K])u = 0\,, \tag{1}$$

where u is the displacement, M and K represent the effective mass and effective stiffness of the plates, and ΔM and ΔK represent the contributions of the beams. Since we have weakly interacting unit cells, we can neglect higher powers of ΔK and ΔM, such that:

$$\ddot{u} + (H_0 + V)u = 0\,. \tag{2}$$

Here, $H_0 = M^{-1}K$ is the diagonalized dynamical matrix of the uncoupled system, $(H_0 + V)$ the dynamical matrix of the coupled system, and $V = M^{-1}(\Delta K) - M^{-1}(\Delta M)M^{-1}K$ a perturbation on the uncoupled system. In general, the perturbation V couples each mode of the unit cell to each mode of neighboring unit cells. This prevents us from restricting our description to modes that only lie in our frequency range of interest, i.e. $H_0 + V$ is not block-diagonal, but instead contains coupling terms between our modes of interest and irrelevant

modes. To remove the coupling between relevant and irrelevant spaces, we perform a suitable rotation, called the Schrieffer-Wolff (SW) transformation, of the dynamical matrix. Originally developed in the context of the Anderson model of magnetic impurities in metals[17][281], the SW transformation is the rotation matrix U such that $U(H_0 + V)U^T$ is block diagonal[19]. This model reduction is a staple in quantum information and condensed matter physics[289, 290]; here we use it to analyze dynamics of mechanical metamaterials.

The SW transformation can be calculated perturbatively, with the expansion parameter[19]

$$\epsilon = \frac{V_{ij}}{E_i - E_j}, \tag{3}$$

where E_i are E_j are eigenvalues of the uncoupled system, and V_{ij} is the coupling between modes i and j. This expansion parameter can be interpreted as the strength of the coupling relative to the spectral gap between the mode of interest and other modes. For small coupling values, the first-order term provides a satisfactory approximation (Fig 5.1e). This first-order term is linear, which means the contributions of the individual geometric elements (beams and holes in the plate system) are additive, which is of crucial importance for our algorithm. Higher orders of the SW transformation provide a more accurate reduced-order description of the system in the presence of stronger couplings (Fig 5.1f, g), but contain long-range interactions, i.e., stiffness terms that couple plates not physically connected by beams (*Supplementary Information*).

In this work, we extract the reduced-order coupling matrix V_{ij}^R from a finite element (FE) simulation (*Methods*). To determine the effect of the beams, we first calculate a large number of modes for a system of two coupled plates (Fig 5.1b). Then, we express these coupled modes as a linear combination of uncoupled plate modes, by using a least-squares approximation of the plate's displacement within a test area (Fig 5.1c). We use this representation to determine the dynamical matrix of the coupled system, by inverting the eigenvalue problem, $D = P^{-1}(H_0 + V)P$. Here, D is the matrix whose diagonal contains the eigenvalues of the coupled system and P is a matrix whose columns contain the modal displacements of the coupled system expressed as a linear combination of uncoupled plate modes. We determine the

perturbation introduced by the holes by following an analogous procedure: We calculate the modes for a plate with holes, express these as a linear combination of unperturbed plate modes and invert the eigenvalue problem. By summing the contribution of the beams and holes, we determine V_{ij}, which is finally SW-transformed resulting in the reduced-order model V_{ij}^{R}.

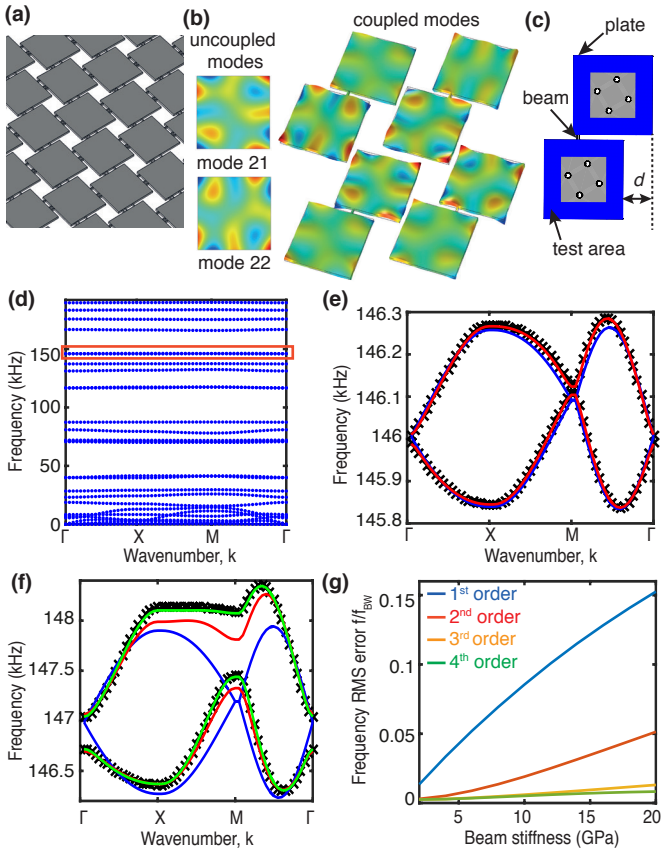

FIG. 5.1: *Method of extracting a reduced-order model.* **(a)**. Test material, made of steel plates connected with polymer beams. **(b)**. Uncoupled degenerate plate modes (left) and modes of the coupled plate system (right). **(c)**. Two plates coupled with one beam and multiple holes to adjust the plate's local stiffness. The displacement is sampled in the blue area and used for the coupling stiffness calculation. **(d)**. Example 2D band structure for a plate-beam metamaterial and frequency range of interest, around 145 kHz encompassing 2 plate modes. Dispersion relation for FE simulation (black data points) and reduced order model for: **(e)**. system with soft couplings (beams with Young's modulus of 4 GPa) compared with first and second order SW transformation, and **(f)**. system with larger coupling strength (beams with Young's modulus of 20 GPa) compared with first, second, and fourth order SW transformations. **(g)**. Error in the frequency relative to the bandwidth frequency (f_{BW}) predicted by the SW transformation, for increasing coupling strengths.

Metamaterial design from a discrete model

We apply the reduced-order modeling method to design a metamaterial, by finding the optimal configuration of plates, beams, and holes to match the target mass-spring model, whose coupling matrix is denoted V^T. We limit the beam stiffness to small values, such that the first order SW transform provides a good first approximation. As a consequence, we can assume changes in our design are additive in their effect (*Supplementary Information*). This means we can easily explore a large space of possible configurations (containing up to 10^{30} elements), by optimizing different parts of the design separately (each design subspace containing less than 10^{10} elements), and by adding combinations of calculated responses from a few FE simulations (~10^2) of different beam and hole parameters. The design examples illustrate this concept.

The first step of our method is to map the discrete model's DOFs into plate modes, taking into account that a single plate can map to multiple DOFs by utilizing multiple plate modes, e.g., degenerate modes (as in the "zero group velocity material" and "topological insulator" design examples). This mapping is done manually, and there are multiple acceptable ways to accomplish it.

The second step is to introduce the desired inter-plate couplings, by determining the beam parameters: location and thickness, and in some cases the angle (e.g., in the "topological insulator" example). To do this, we pre-compute a table of coupling stiffnesses for different beam locations and plate alignments (*d* in Fig. 5.1c). We then perform a combinatorial search, exploiting the additivity of the first-order SW transformation, to find a set of beams that add up to the desired coupling (*Methods*). Finally, we perform a gradient-based optimization to compensate for second-order effects due to the finite beam stiffness. This optimization is seeded by the approximate solution from the combinatorial search and is done on a test system containing two plates (Fig. 5.1c).

The third step is to tune each plate's local response, i.e., each mode's frequency and the couplings between different modes of the same plate. This tuning corrects for the local effect of the beams, which shift the plate frequencies and introduce couplings between different

modes of the same plate. We first add up the local contribution of all beams connected to a plate and then determine the necessary adjustment to match the desired local properties. This adjustment is obtained by introducing holes in the plate. Since the plate modes have different displacement profiles, holes in different locations will have different effects in each of the modes. We determine the hole radii and locations by the same procedure that we used with the beams: (1) create a table of the hole's effect in different locations, (2) perform a combinatorial search on the hole table, and (3) perform a gradient-based optimization on the results of the combinatorial search.

As a fourth and final step, we perform a final gradient-based optimization on a system containing multiple unit cells. This optimization includes all holes and beams, and therefore is able to compensate for second-order effects that arise due to the interactions of beams and holes as well as long-range couplings (*Supplementary Information*).

Design examples

Phononic Veselago lens

We first design a classical Veselago lens[33] metamaterial as an example to demonstrate how our design method works. We choose this example because the Veselago lens is a well-understood system that has been demonstrated in optical[4] and acoustic[272] systems.

In the phononic Veselago lens, a double negative medium, i.e., a medium with negative effective modulus ($-K$) and effective density, is embedded in a conventional medium of equal but positive modulus ($+K$) and effective density (Fig. 5.2a). We create a mass-spring system that approximates the lens in a square lattice. The basic unit cell consists of a single resonator connected by springs to its 4 nearest neighbors (Fig. 5.2b).

The target coupling stiffness between unit cells is either $+K$ or $-K$. The effective masses are obtained by shifting the local resonance frequencies of the sites inside and outside the lens region. The normalized effective mass of a harmonic oscillator at a particular frequency is

$M_{eff}(\omega) = \left(1 - \frac{\omega_0^2}{\omega^2}\right)$, where ω_0 is the resonance frequency of the mode and ω is the lens' frequency of operation. The Veselago lens requires $M_{lens}(\omega) = -M_{medium}(\omega)$. The relation between the local resonance frequency of the sites inside and outside the lens region is thus:

$$\omega_{lens}^2 = 2\omega^2 - \omega_{medium}^2. \quad (4)$$

We choose the plate mode 24 to couple between unit cells, which has a high enough stiffness compared to the beams, and is well separated from neighboring modes. Since the mode profiles at the boundaries have 90° rotational symmetry, if the plates are perfectly aligned, couplings of only one sign are possible. To overcome this limitation, we offset the plates so we can find beam positions to design both positive and negative couplings (Fig. 5.2c). We choose the beam parameters that give a positive or negative coupling based on the pre-computed coupling stiffnesses (Fig. 5.2d). We then choose the hole parameters that compensate for the local stiffness introduced by the beams, such that the unit cells inside and outside the lens have the required local resonance frequencies from equation (4) (Fig. 5.2e).

We analyze the resulting metamaterial lens using FE simulations (*Methods*). The results clearly illustrate the Veselago lens effect (Fig. 5.2f), and show excellent agreement with the results of the mass-spring model (Fig. 5.2g).

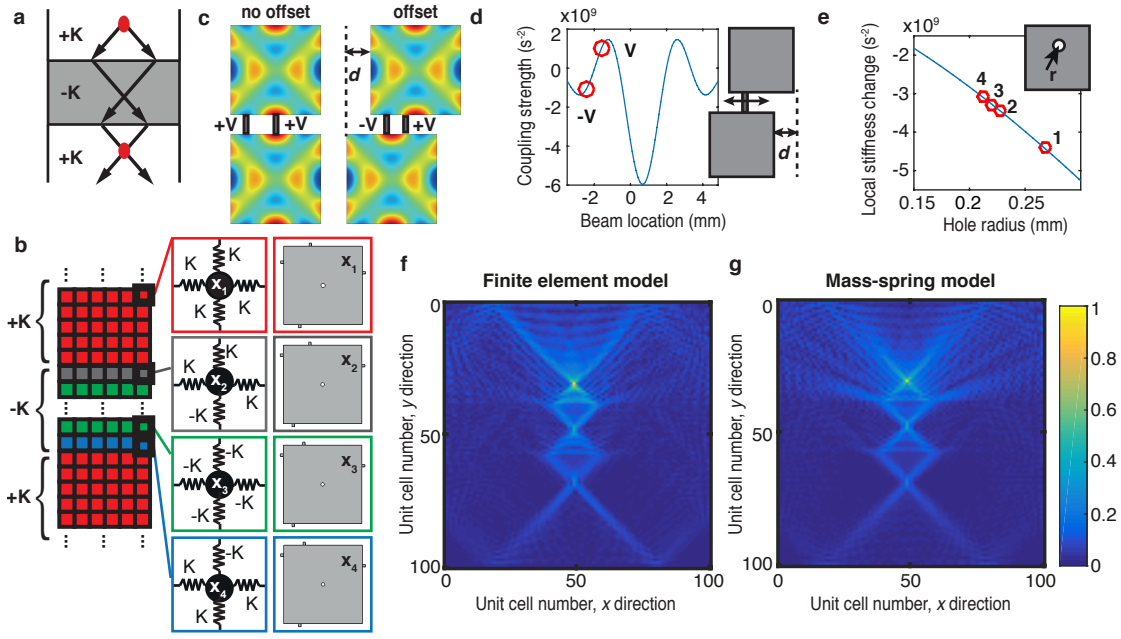

FIG 5.2: *Veselago lens metamaterial example.* **(a)**. A schematic of focusing in the Veselago lens. **(b)**. Mass-spring model of the lens, showing construction of the four different unit cells and their corresponding metamaterial design: a unit cell with all positive springs (red), a unit cell with all negative springs (green), and two interface unit cells with a combination of positive and negative springs (gray and blue). Lattice sites (x_1, x_2, x_3, x_4) are local resonators with their own mass and spring. The mass-spring model contains 100x100 unit cells, where the double negative region consists of nineteen rows in the center. **(c)**. Illustration of plate offset concept with mode 24: when plates are aligned (left), only couplings of one sign are possible. If plates are offset by distance *d,* both positive and negative couplings are possible. **(d)**. Calculated coupling stiffness for different beam locations at a given offset, where data points show locations of the beams to achieve positive and negatives stiffness. **(e)**. Calculated local stiffness change for different hole radii, where data points show the radii in each of the four unit cells for the intra-plate coupling compensations. **(f)**. Results of metamaterial lens from FE simulations, at 175.284 kHz. g. Results of mass-spring model lens, at 175.204 kHz. The color bar applies to both f and g, and indicates the normalized amplitude of the RMS displacement.

Zero group velocity material

We now design a zero group velocity (c_g) material, which has a flat band within a lattice with 1D periodicity, as a way to demonstrate the use of multiple and degenerate modes of a single plate in our design method. The zero c_g material is analogous to a quasi-1D Lieb lattice, and is of interest as it is a perfectly periodic configuration that leads to a flat band without using defects. Such localized states have been explored recently in photonic waveguides[291, 292], and could have applications for slow phonon modes in elastic metamaterials.

In this example, the target unit cell consists of three equal resonators in an "L" configuration (Fig. 5.3a). We start by mapping every DOF (x_1, x_2, y_1) to a plate mode. We choose a unit cell design consisting of two plates (P1 and P2). We map x_1 and y_1 to a pair of degenerate plate modes (21, 22) in P1, and x_2 to one mode in P2, within the same degenerate pair. This leaves us with an extra mode within our frequency range of interest, y_2 (Fig. 5.3b), which we remove from the dynamics by shifting its frequency outside the range of interest, through the introduction of holes in the plate. We point out that this mode assignment is not unique and we could, e.g., use non-degenerate modes and a three-plate unit cell design. We choose to use degenerate modes to illustrate how we can exploit them, which is crucial in the next design example, the topological insulator.

The equation of motion of the system in Fig. 5.3b is: $\ddot{u}_i = V_{i\mathrm{mod}2}^T\, u_i + V_m^T u_{(i+1)} + V_m^T u_{(i-1)}$. The vector *u* contains the two DOFs *x* and *y*, and *i* is the index of the unit cell. The target coupling matrices for the inter-plate couplings (V_m^T), and the intra-couplings (V_0^T, V_1^T) are:

$$V_m^T = \begin{bmatrix} \alpha & 0 \\ 0 & 0 \end{bmatrix},\ V_1^T = \begin{bmatrix} \beta & \alpha \\ \alpha & \beta \end{bmatrix},\ V_0^T = \begin{bmatrix} \beta & 0 \\ 0 & \beta + \Delta \end{bmatrix} \tag{5}$$

where α is the coupling strength, β is the local stiffness of the plate, $\alpha \ll \beta$, and Δ is the compensation for the extra mode.

In this metamaterial design, we illustrate the concept of using one plate to implement multiple DOFs (Fig. 5.3b,c). We chose the degenerate plate modes 21 and 22 (Fig. 5.1b), which is motivated by the following requirements: (1) there is good separation between the degenerate pair of interest and neighboring modes; and (2) the mode profiles at the boundary exhibit a complex structure that enable a wide variety of coupling stiffness.

We do a combinatorial search to determine the plate offset, and thickness and position of the beams, finding that three-beam combinations can satisfy the target coupling stiffness matrix V_m^T. We then find the plate hole locations to satisfy the target matrices V_1^T and V_0^T. We

perform an additional gradient-based optimization on multiple unit cells to reduce the second order error between the metamaterial and target stiffness (*Supplementary Information*).

The dispersion relation for the zero c_g metamaterial compared to the mass-spring model is shown in Figure 5.3d. The metamaterial dispersion shows excellent correspondence to the mass-spring system. While there is some slight non-zero group velocity in the flat band from long-range couplings (*Supplementary Information*), our metamaterial approaches the desired the mass-spring model with very good precision.

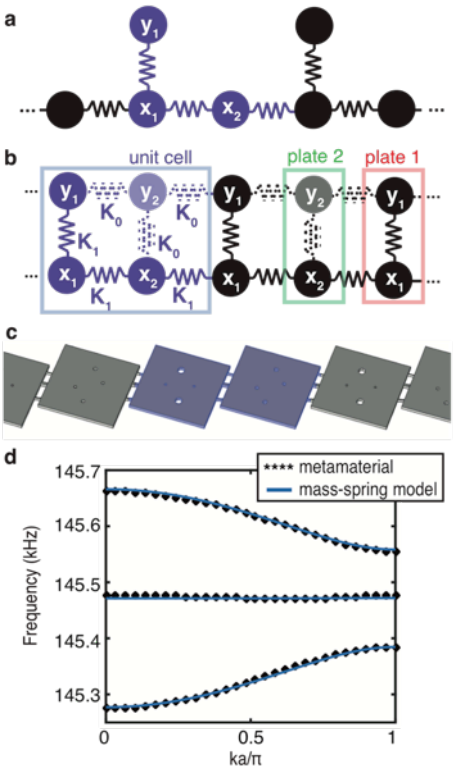

FIG. 5.3: *Zero group velocity metamaterial.* **(a)** Zero c_g material mass-spring model. **(b)** Mass-spring model used for metamaterial design, where each vertical column of two masses *x* and *y* represents two degenerate modes of one plate in the metamaterial. The metamaterial is optimized to separate mode y_2 in plate 2 from the other modes, and to push K_0 to 0. **(c)** Design of the zero c_g metamaterial, with unit cell highlighted in purple. **(d)** Dispersion curves for the zero c_g material mass-spring model compared to the designed metamaterial. Only the three energy bands of interest are shown for clarity.

Topological insulator

Topological insulators are a unique class of materials that are electrically insulating in the bulk, yet conductive on the surface, and whose surface states are immune to back-scattering and defects[293-295]. These materials have inspired a new class of mechanical systems that mimic these topological insulator properties in the elastic domain[31, 61, 280, 296-299]. Researchers have developed a mapping between topological spin-orbit systems and discrete mechanical lattices[76, 300], which are highly complex. Here, we focus on the mass-spring model proposed in ref. 15, which contains 6 DOFs per unit cell that interact nontrivially with neighboring unit cells. While this mass-spring model was realized with a discrete system of pendula[31], the implementation of such models in metamaterials is an open research problem, which our method is able to solve.

The mass-spring model unit cell for this topological insulator consists of three 2-DOFs lattice sites[31] (Fig. 5.4a). The equation of motion is $\ddot{u}_{ij} = V_L^T\, u_{ij} + V_0^T u_{(i+1)j} + V_0^T u_{(i-1)j} + V_{i\mathrm{mod}3}^T u_{i(j+1)} + V_{i\mathrm{mod}3}^T u_{i(j-1)}$. The vector *u* contains the two DOFs *x* and *y*, and *i* and *j* are the row and column indices of the unit cells in Fig. 5.4a. The target inter-plate coupling matrices are:

$$V_n^T = \alpha \begin{bmatrix} \cos(2\pi n/3) & \sin(2\pi n/3) \\ -\sin(2\pi n/3) & \cos(2\pi n/3) \end{bmatrix} \tag{6}$$

where n is an integer that spans from 0 to 2. The intra-plate coupling matrix is $V_L^T = I_2\beta$, where I_2 is the identity matrix, and β and α are as defined above.

The designed metamaterial translates each 2-DOF site into a single plate, by using the degenerate plate modes 21 and 22. Thus the unit cell consists of 3 plates coupled with beams (Fig. 5.4b), which are optimized to match the required V_0^T, V_1^T, and V_2^T matrices. By performing separate combinatorial optimizations for each coupling, we reduce the problem to three searches on a space of 10^{10} configurations instead of a single search on a space of 10^{30} configuration. Our method cannot obtain a solution for all three couplings at a single offset,

so we introduce a third beam parameter: an angle. A non-zero beam angle allows for different plate alignments using the same offset for the three different couplings (Fig. 5.4b).

We calculate the band structure of the metamaterial with 1D periodicity (*Methods*). The dispersion relation (Fig. 5.4c) shows the expected three bands of bulk modes, separated by two counter-propagating edge modes that cross at $\pi/3$ and $2\pi/3$. We then model a finite 7x7 plate system and calculate the eigenmodes with a FE simulation, and the results clearly show edge modes (Fig. 5.4d). The metamaterial shows excellent agreement to the target mass-spring model (*Supplementary Information*). The designed metamaterial also illustrates the stability of topologically protected modes against defects. We explore this by introducing a defect in the metamaterial, which we model as three fixed plates. The edge mode still persists, and propagates around the defect (Fig. 5.4e).

Micro-fabrication of these composite metamaterials should result in high-speed devices with advanced signal processing capabilities, and benefit engineering applications in communication systems, ultrasonic imaging, and filtering for surface acoustic waves. Further exploration should aim to increase the bandwidth and reduce constraints in the material parameters, as well as to deliberately introduce nonlinearity. The same design method that we have presented here can be applied to electromagnetic systems[278, 301], enabling the design of arbitrary photonic circuits with extreme computing capabilities[273].

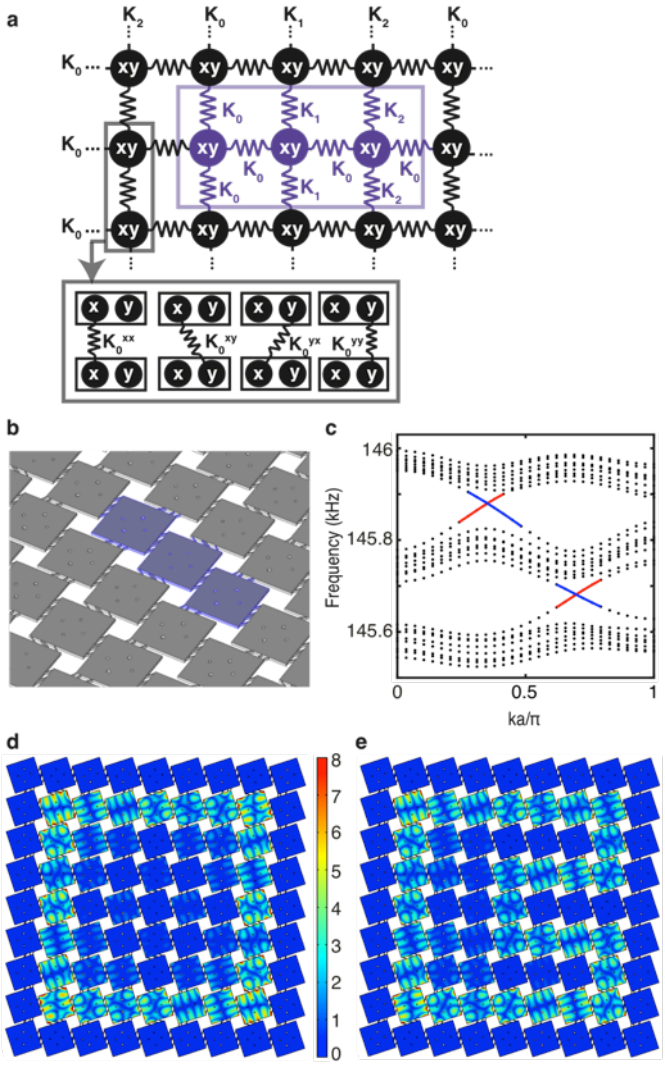

FIG 5.1: *Topological insulator metamaterial.* **(a)** Mass-spring model for topological insulator[15], where each mass x and y represents two degenerate modes of a plate in the metamaterial. Inset shows construction of the couplings between neighboring pairs of DOF *x* and *y*. **(b)** Metamaterial designed from topological insulator mass-spring model. **(c)** Dispersion curves for the metamaterial, with periodicity in one direction and finite in the other, showing three bulk bands, indicated by the black points, separated by the two sets of counter-propagating edge modes, indicated by the red and blue solid lines. **(d)** Example edge mode of the metamaterial. **(e)** Edge mode propagation around a defect (3 fixed plates) in the metamaterial. In **d** and **e**, the outer edge plates are fixed, and the color bar indicates the amplitudes of both plots, in terms of total modal displacements with arbitrary normalized units.

Methods

The results presented in this paper have been calculated by using COMSOL Multiphysics® for the finite element simulations and MATLAB for the linear algebra calculations (except otherwise indicated). The two programs can communicate through the LiveLink® interface

provided by COMSOL. The simulations were performed in ETH Euler cluster nodes and accessed up to 400 GB of RAM.

In all simulations we have used a linear elastic model with material parameters from epoxy resin for the beams (Young's modulus $E_B = 4.02$ GPa, Poisson ratio $\nu_B = 0.22$ and density $\rho_B = 1190\ kg/m^3$) and steel for the plates ($E_P = 193$ GPa, $\nu_P = 0.3$ and $\rho_P = 8050$).

Coupling Matrix Extraction

We extract the coupling matrices by calculating the first 80 eigenmodes for a system of two plates coupled by beams (Fig 5.1c). The eigenmodes are calculated using COMSOL Multiphysics® 3D linear elasticity solver, with a highly refined mesh containing 964k elements. This fine mesh is required since the frequency shift introduced by the beams is much smaller than the resonance frequency of the plates, and therefore small imprecisions in the plate eigenfrequencies result in large errors in the calculated coupling matrix.

We then sample the x, y and z components of each eigenmode's displacement. The sampling is done at 2268 points at each plate, distributed over a test area extending 2 mm from the sides of the plate (Fig 5.1c). The sampled displacements for the 80 relevant eigenmodes are stored in a matrix, whose i-th column U_j^i contains the *x*, *y* and *z* displacement for the i-th eigenmode: $U_j^i = \left(x_1^i, x_2^i, \dots x_{2268}^i, y_1^i, y_2^i, \dots, y_{2268}^i, z_1^i, z_2^i, \dots, z_{2268}^i\right)^T$. The subindex j is used to distinguish between the two plates.

We express the displacement of the coupled-plate system in terms of a basis containing the first 40 normal modes of a free plate. Since our finite basis consists of a limited number of modes, it is incapable of exactly reproducing the coupled vibration profiles. For this reason, we use the Moore-Penrose pseudoinverse, which provides a least-square approximation to the solution. This approximation is given by $P_j = (A^T A)^{-1} A^T U_j$ where *A* is a matrix whose i-th column contains the displacement of the i-th free-plate eigenmode, sampled over the test area and organized in the same layout as U_j. We use 80 eigenmodes of the coupled system and 40 eigenmodes for the free plate. The mode selection must take into account several aspects: the number of eigenmodes for the two-plate coupled system should be twice the

number of modes for the individual system, the coupled modes should not include any beam resonances, and families of degenerate modes should be either completely included or completely excluded. Once the matrix P_j has been calculated, we assemble the matrix:

$$P = \begin{pmatrix} P_1 \\ P_2 \end{pmatrix},$$

and calculate the coupling matrix as $V = PDP^{-1} - H_0$ where D is an 80x80 square matrix whose diagonal elements contain the eigenvalues of the coupled system, $D_{ij} = (2\pi f_i)^2 \delta_{ij}$ and H_0 contains the eigenvalues of an unperturbed single plate:

$$H_0 = \begin{pmatrix} D^0 & 0 \\ 0 & D^0 \end{pmatrix}$$

with $D_{ij}^0 = (2\pi f_i^0)^2 \delta_{ij}$ and f_i^0 the i-th eigenfrequency of an unperturbed plate.

The coupling matrix extraction method is equivalent to the first-order term of the Schrieffer-Wolff transformation, for a low-energy space spanning the first 40 eigenmodes of the unperturbed plate. This is because to first order, the Schrieffer-Wolff transformation is simply a restriction on the low-energy subspace, with the identity as a rotation matrix (see Supplementary Information). Once this first transformation has been performed, we calculate the higher orders to obtain the reduced-order model V^R containing only the required modes (see supplementary information).

Optimization Process

Combinatorial optimization

We identify the optimal beam locations by performing an exhaustive search on combinations of beam locations and thicknesses. In this step, we calculate the coupling matrix V_{ij}^R for a system containing multiple inter-plate coupling beams by adding together the coupling matrices of systems containing a single coupling beam. The validity of this approximation is examined in the Supplementary Information.

We first run the optimization code for different plate offsets in the range between 2 mm and 4 mm, with a spacing of 0.2 mm. We then assemble a table of coupling matrices V_{ij} as a function of the beam location, for a fixed beam width of 0.2 mm. The coupling matrices are

calculated using the finite element method described in the coupling matrix extraction section. The coupling matrices corresponding to beam widths other than 0.2 mm are calculated assuming a linear relation between beam width and coupling matrix, i.e. $V_{ij}(w) = [w/w_0]V_{ij}(w_0)$.

We then evaluate all combinations of beam locations (in steps of 0.1 mm) and beam widths (between 0.1 m and 0.5 mm in steps of 0.01 mm). We identify the optimal beam parameters by comparing the calculated coupling matrices to the objective coupling matrices. Before this comparison, the calculated and objective matrices V_{ij} are normalized using the Hilbert-Schmidt norm $|V| = \sqrt{Tr[V^T V]}$. This is done since the exact norm can be adjusted after the fact by finely scaling the beam widths. This can be done due to the approximately linear relation between beam width and coupling matrix. In this step, we discard beam combinations whose norm is more than 50% off the target value, since those would result in extreme beam dimensions after rescaling.

The exhaustive search code is written in C++ to maximize its speed. For every offset (We considered 10 of them), the code explores $10^9 - 10^{10}$ configurations and takes between 43s and 197s to run on a 2.5 GHz Intel™ Core i7® laptop.

Gradient optimization

The gradient optimization is performed after the exhaustive search, in order to refine the beam parameters and account for interactions between the beams. At every gradient iteration, the coupling matrix is evaluated for a reference configuration and for small variations around this configuration. For systems containing three beams (the topological insulator and zero-dispersion material), the configuration is represented by a vector of the form $s = (x_1, w_1, \theta_1, x_2, w_2, \theta_2, x_3, w_3, \theta_3)^T$ where x_i is the location of the i-th beam, w_i is the i-th beam width and θ_i is the i-th beam angle. Different numbers of beams can be accommodated by adding or removing components. The coupling matrix V_{ij}^R is also expressed in vector form $v = (V_{11}, V_{21}, V_{12}, V_{22})^T$. These definitions allow us to define a Jacobian matrix such as $v(s_0 + \Delta s) \approx v_0 + J\Delta s$ where the columns of J are calculated as $J_i = v(s_0 + S_i) - v(s_0)$, and S is a matrix where each column S_i represents a perturbation in the configuration

vector's i-th component. We use perturbations of 0.04 mm for the beam locations, 0.01 mm for the beam thickness and 2 degrees for the beam angles. The coupling matrix vector $v(s)$ is calculated using the coupling matrix extraction method described earlier.

The optimized state of the system after a gradient iteration is defined as $s_1 = s_0 + \alpha S J^T (JJ^T)^{-1} * e - Sk$, where e is the error vector $e = v - v_T$, v_T is the objective coupling matrix k expressed in vector form, α is a parameter controlling the gradient descent speed and k is a vector from the Jacobian's kernel, i.e. $Jk = (0 \quad 0 \quad 0 \quad 0)^T$. The value of α is set to 0.4 at the beginning of the optimization process and then increased to 1 when the modulus of the error vector e falls below 5% of the objective vector v_T's modulus.

The kernel vector k does not affect the coupling matrix and is chosen to minimize participation of unwanted modes. We observe that the addition of k reduces these unwanted modes by 30% to 50%. We determine the direction of k by first defining a scalar value ϵ that quantifies the participation of unwanted modes. The vector k is then given by the projection of the gradient of ϵ into the kernel of J. The gradient of ϵ is defined with respect to the changes in the geometry, so $k = \gamma \wp_{Kern(J)} * \nabla_S \epsilon$, where $(\nabla_S \epsilon) = \epsilon(s_0 + S_i) - \epsilon(s_0)$, and $\wp_{Kern(J)}$ is a projector into the kernel of J. The value of ϵ is defined as $\epsilon = \sqrt{\epsilon_1^2 + \epsilon_2^2 + \cdots + \epsilon_n^2}$ where n is the number of coupled modes within our frequency range of interest, and $\epsilon_i = \left|(I - P)U_i^{FEM}\right|$ is defined as the distance between the i-th coupled mode's displacement profile in the test area $U_i^{FEM} = \left(x_1^i, x_2^i, \ldots x_{2268}^i, y_1^i, y_2^i, \ldots, y_{2268}^i, z_1^i, z_2^i, \ldots, z_{2268}^i\right)^T$ and its projection into free-plate modes within the range of frequencies of interest, implemented with the projector $P = A(A^T A)^{-1} A^T$ where A is a vector whose columns contain the sampled displacements of the free-plate modes in the frequency range of interest, following the same layout as U_i^{FEM}. The errors in the two coupled plates are reduced to a single number as ϵ by taking the RMS value of the two errors. The norm of k is adjusted empirically between 0.5 and 2.

Finite Element Simulations

Veselago lens

Our model Veselago lens consists of 100x100 unit cells, each of them containing 141k elements. In order to solve this system, we follow a dynamic condensation approach[302]. We cut each unit cell at half along the length of the beams and define a transfer matrix that relates the displacements and forces acting on the boundary DOFS at the connection points, using 117 DOFs for every connecting beam cross section. We do this by first defining the unit cell dynamic force balance equation $-M\omega^2\ddot{x} + ib\omega Mx + Vx = F$, where M and V are the unit cell's mass and stiffness matrices obtained from COMSOL, $b = 33\ s^{-2}$ is a damping parameter. We then introduce the dynamic stiffness matrix $D = -M\omega^2 + ib\omega M + V$ and decompose the set of nodal forces and displacements into set associated with boundary (b) and interior (i) nodes. By prescribing zero force at the interior nodes, the interior displacements can be condensate as $x_i = -D_{ii}^{-1}(D_{ib}x_b)$. As a result, we obtain a condensed matrix $D_{con} = D_{bb} - D_{bi}(D_{ii}^{-1}D_{ib})$. We solve this system of equations using the PARDISO solver included in the Intel Math Kernel Library, which can solve systems with multiple right hand sides without repeating common steps such as the matrix factorization. Similarly, we define a conversion matrix $C = \begin{bmatrix} -D_{ii}^{-1}D_{ib} \\ I \end{bmatrix}$, that provides the values of the full displacement vector x as a function of the boundary DOF's x_B, $x = Cx_b$.

We then solve the force-balance problem for the full lens in terms of the boundary nodes. The force at each node is set to zero, except for those in the interface between the x=50 y=31 and x=50 y=32 which are driven with unit strength. After solving for the displacements in each step, we calculate the RMS amplitude of every unit cell by using the equation $x_{RMS} \propto \sqrt{E}$, where E is the total steady-state energy stored in a unit cell, calculated as $E = (1/2)x_B^{\dagger}C^{\dagger}(\omega^2 M + V)Cx_B$ where † denotes the Hermitian conjugate.

Zero c_g metamaterial and topological insulator

The zero group velocity metamaterial is simulated in COMSOL using a unit cell subject to Floquet boundary conditions at half the beam's length, using 1.02M elements per unit cell.

The topological insulator dispersion relation (Fig. 5.4c), we model 4 unit cells (3x1 plates) stacked in a column in the finite dimension, such that the modeled system consists of 12x1 plates coupled with beams. This simulation was done using 901k elements. Fixed boundary conditions were applied on both ends of the beams of the finite dimension, and Floquet boundary conditions were applied in the other dimension. To determine the polarization of the edge modes around the crossing points, we calculate on which side of the model, in the finite dimension, the stored energy density is localized. The exact locations of the edge mode crossing points depend on which plate within the 3-plate unit cell is connected to the fixed boundary. The finite-size topological insulator was simulated directly in COMSOL using 2.6M elements.

Supplementary: Calculation of the Schrieffer-Wolff transformation as a series expansion

We create a reduced order model for an infinite, periodic perturbative metamaterial by calculating a Schrieffer-Wolff transformation of the perturbation matrix V_{ij}. The Schrieffer-Wolff transformation is calculated as a series expansion up to order n. We refer to the resulting reduced matrix as V^R. We will also use H_0^R to refer to the unperturbed cells' dynamic matrix, restricted to the subspace of modes that lie in the frequency range of interest. The reduced matrices V^R and H_0^R describe the force acting on an arbitrary unit cell (we call it the center) as a function of the displacement of its neighbors. When calculating the SW transformation for order n, we must take into account interactions with neighbors that are up to n unit cells away from the center. Figure 5.S1 shows the system under consideration.

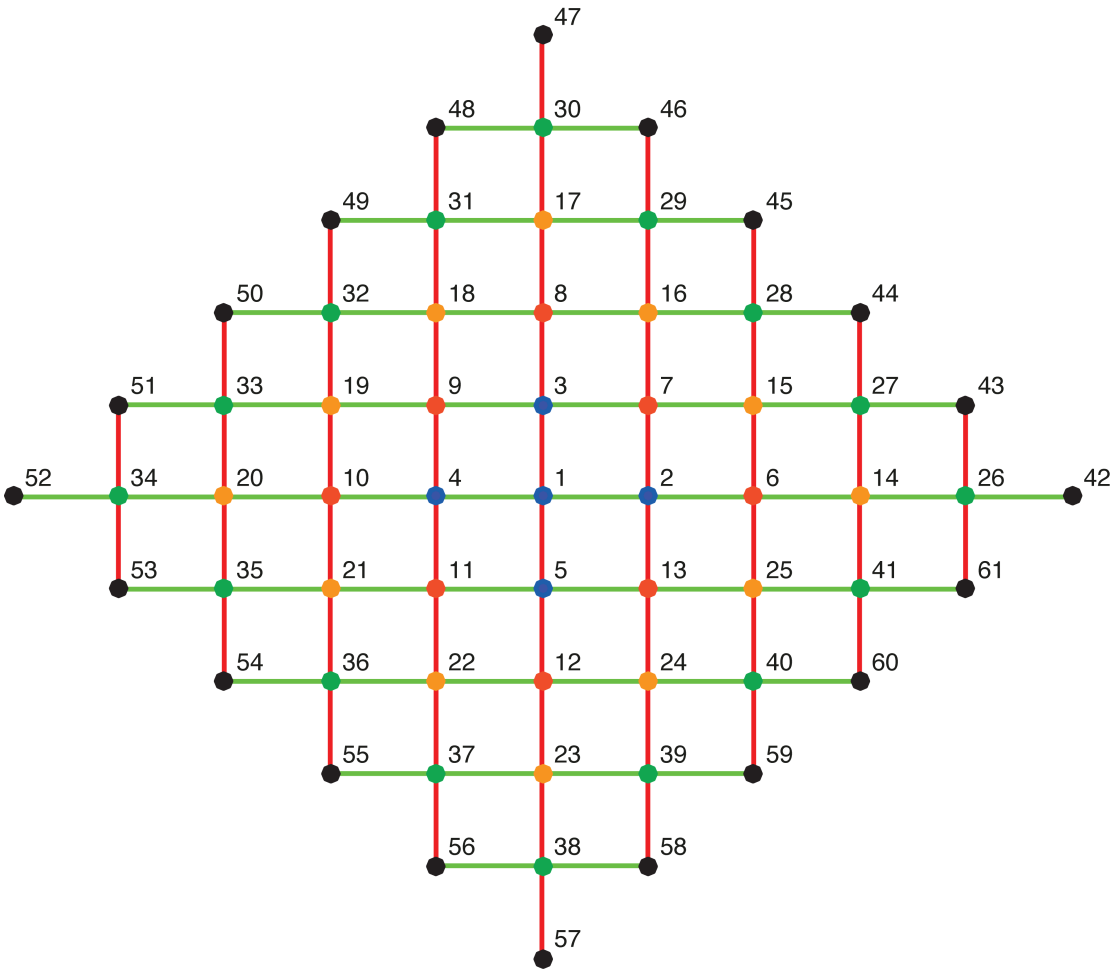

FIG. 5.S1: *Test system for the calculation of the Schrieffer-Wolff transformation.* The dots represent unit cells. For a first order calculation, only the blue dots are required. We then add the black dots (for second order), green dots (for third order), yellow dots (for fourth order) and red dots (for fifth order). The lines represent the coupling between a unit cell and its nearest neighbor in the x-direction (V^H, green) and y-direction (V^V, red).

We first proceed to assemble the matrices V and H_0 for the coupled system represented in Fig. 5.S1. These are $m \times m$ square matrices, where $m = l \times (number\ of\ cells)$, l being the number of local modes per unit cell. The number of local modes l refers to the full description obtained from finite elements (as described in the coupling matrix extraction part of the methods section), containing 40 modes per plate for cases described in our paper, and not to the final reduced model which contains 1-6 modes per unit cell.

The matrix assembly utilizes the matrices V^H(Describing the effect of the beams coupling horizontal plates), V^V (Describing the effect of the beams coupling vertical plates), V^{HOLE} (Describing the effect of the holes) and H_0^S (Describing the unperturbed modes of a single

plate). For unit cells containing multiple plates, additional matrices should be included to account for inter-plate couplings inside the unit cell. The matrices V^H and V^V are obtained by simulation of a two-plate system as described in the Coupling Matrix Extraction part of the Methods section. The horizontal two-plate simulation yields the coupling V^{LR} between horizontally neighboring plates. In addition, the plate on the left experiences a frequency shift V_{LL} due to having beams on the right, and the plate on the right experiences a shift V_{RR} due to having beams on the left. We obtain an analogous result for a system of vertical plates, with local frequency shifts given by V^{DD} and V^{UU}, and an inter-plate coupling given by V^{DU}. The matrices V^H and V^V, which summarize the effect of all 4 nearest neighbors, are structured as:

$$V^H = \begin{pmatrix} V^{LL} & V^{LR} \\ V^{RL} & V^{RR} \end{pmatrix} \qquad V^V = \begin{pmatrix} V^{DD} & V^{DU} \\ V^{UD} & V^{UU} \end{pmatrix}$$

Where the terms V^{LL}, V^{RR}, V^{UU} and V^{DD} represent local changes in the unit cell dynamics brought by the beams placed on the right, left, bottom and top of the plate respectively, and V^{LR}, V^{RL}, V^{UD}, V^{DU} represent the inter-plate couplings from the beams. The terms V^{LL}, V^{RR}, V^{UU} and V^{DD} are what we correct for with the introduction of holes in the plate. For a given unit cell number r, the matrix V describing the whole system in Fig. 5.S1 satisfies:

$$V_{i+(r-1)l,j+(r-1)l} = V_{ij}^{LL} + V_{ij}^{RR} + V_{ij}^{DD} + V_{ij}^{UU} + V_{ij}^{HOLE}$$

For a pair of adjacent unit cells r and t, with r being on the left of t, we have ($1 \leq i, j \leq l$):

$$V_{i+(r-1)l,j+(t-1)l} = V_{ij}^{LR}$$
$$V_{i+(t-1)l,j+(r-1)l} = V_{ij}^{RL}$$

For a pair of adjacent unit cells r and t, with r below t, we have ($1 \leq i, j \leq l$):

$$V_{i+(r-1)l,j+(t-1)l} = V_{ij}^{DU}$$
$$V_{i+(t-1)l,j+(r-1)l} = V_{ij}^{UD}$$

The term H_0 is the diagonalized, unperturbed (excluding effects of the beams and holes) dynamical matrix of the system depicted in Fig. 5.S1, contains as many diagonal copies of H_0^S as unit cells required for the desired order of approximation, and has the form:

$$H_0 = \begin{pmatrix} H_0^S & 0 & \dots & 0 \\ 0 & H_0^S & \dots & 0 \\ \dots & \dots & \dots & \dots \\ 0 & 0 & \dots & H_0^S \end{pmatrix}$$

After assembling the matrices, we proceed to compute the Schrieffer-Wolff transformation as a series expansion of order $n \leq 5$. The new effective dynamical matrix will be given by[19]:

$$H_{eff}^R = H_0^R + V^R = \wp^T \left[H_0 + \sum_{r=1}^{n} H_i \right] \wp$$

Where $\wp$ represents a projector into the subspace of relevant modes. As a consequence of this projection, the resulting system H_{eff}^R involves only the relevant modes. The first five terms H_i in the series expansion of the Schrieffer-Wolff transformation are given by:

$$H_1 = V$$
$$H_2 = (1/2)[S_1, \mathcal{O}(V)]$$
$$H_3 = (1/2)[S_2, \mathcal{O}(V)]$$
$$H_4 = (1/2)[S_3, \mathcal{O}(V)] - (1/24)\big[S_1, \big[S_1, [S_1, \mathcal{O}(V)]\big]\big]$$
$$H_5 = (1/2)[S_4, \mathcal{O}(V)] - (1/24)\big(\big[S_2, \big[S_1, [S_1, \mathcal{O}(V)]\big]\big] + \big[S_1, \big[S_2, [S_1, \mathcal{O}(V)]\big]\big] + \big[S_1, \big[S_1, [S_2, \mathcal{O}(V)]\big]\big]\big)$$

Where $\mathcal{O}(V)$ is a square matrix with the same size of V, but containing only block-off-diagonal terms, i.e. those that couple a relevant mode to an irrelevant mode, and having all the block-diagonal terms set to zero. The symbol $[A, B]$ represents a commutator: $[A, B] = AB - BA$. The terms S_1 to S_4 are given by:

$$S_1 = \mathcal{L}(V)$$
$$S_2 = -\mathcal{L}([\mathcal{D}(V), S_1])$$
$$S_3 = \mathcal{L}\big(-[\mathcal{D}(V), S_2] + (1/3)\big[S_1, [S_1, \mathcal{O}(V)]\big]\big)$$

$$S_4 = \mathcal{L}\left(-[\mathcal{D}(V), S_3] + (1/3)\left(\left[S_1, [S_2, \mathcal{O}(V)]\right] + \left[S_2, [S_1, \mathcal{O}(V)]\right]\right)\right)$$

Here, $\mathcal{D}(V)$ is a matrix the same size as V but with zeroes replacing all the terms coupling relevant-to-relevant or irrelevant-to-irrelevant modes. The function $\mathcal{L}$ is defined as:

$$[\mathcal{L}(A)]_{ij} = \begin{cases} \dfrac{A_{ij}}{(H_0)_{ii} - (H_0)_{jj}} & if\ (i,j)\ is\ block - off - diagonal \\ 0 & if\ (i,j)\ is\ block - diagonal \end{cases}$$

Supplementary: Additive Properties of Perturbative Metamaterials

The technique we presented in this paper allows us to design metamaterials based on complex mass-spring models, such as those with nontrivial topological properties. This ability to implement advanced functionality arises from the linear relation between the reduced order model and the metamaterial geometry, which is valid when the Schrieffer-Wolff transformation is evaluated to first order. A linear relation between material and model means that the springs in a mass-spring model corresponding to a system containing multiple inter-plate coupling beams will be the sum of the springs in the mass-spring models corresponding to systems containing each one of the beams (Fig. 5.S2a).

This linear approximation is valid as long as the first-order perturbative Schrieffer-Wolff transformation is accurate (Fig. 5.S2b). For the polymer beams that we use in this work ($E = 4.02$ GPa), the error in the stiffness matrix is below 5%. This low error allows us to evaluate vast design spaces (exceeding 10^{40} configurations for the beam locations and widths) without having to perform a full finite-element simulation for each design.

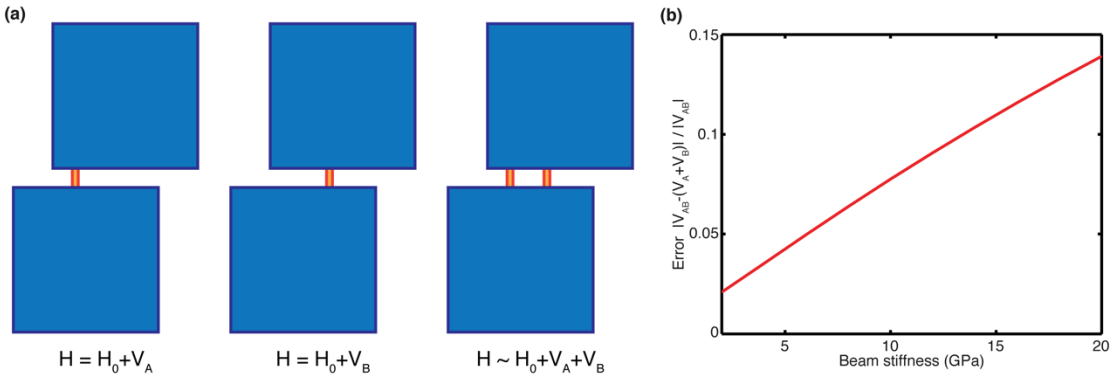

FIG 5.S2: Beam width linearity. **(a)** Two-plate system used to test the linear dependence between beam width and coupling matrix. **(b)** Error in the coupling matrix of a two-beam system obtained by adding single-beam solutions, as a function of the beam stiffness. Higher beam stiffness result in higher relative errors since the first-order Schrieffer-Wolff transformation becomes inaccurate at high coupling strengths.

Additionally, in the range of beam widths present in our design, the coupling matrix V (which describes the effect of the polymer beams) increases linearly with each beam's width w: $V \approx V_0 \left(\frac{w}{w_0}\right)$, where V_0 and w_0 are the coupling matrix and beam width for a reference configuration. This approximation is very accurate (Fig 5.S3a-c), with an error below 1.2% for the beam widths considered in this work.

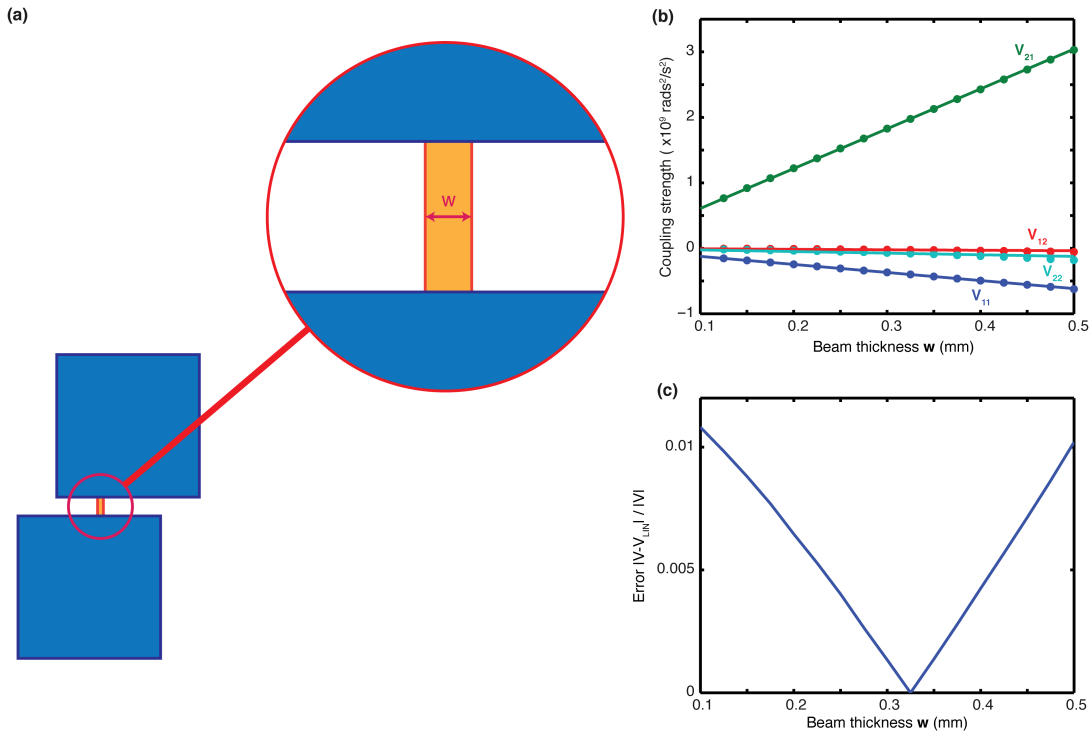

FIG 5.S3: Beam width linearity. **(a)** Two-plate system used to test the linear relation between beam width and coupling matrix. **(b)** Elements of the coupling matrix V_{ij}, describing the coupling between plate modes 21 and 22. The coupling matrices have been obtained by finite element simulation (dots) and by linear extrapolation from a single beam width (solid lines). **c.** Relative error of the coupling matrix as a function of the beam width. The result is exact when the beam width matches the reference width w_0.

The linear relation between beam width and geometry allows us to speed-up the optimization process by simulating a single beam width at every location, and extrapolating the coupling strength of different widths from this single finite element simulation.

Supplementary: Coupled optimization in the Zero Group Velocity lattice model

Our method for designing metamaterials by separately tuning the design parameters considers only the interaction between a unit cell and each neighbor, and neglects interactions between different perturbations. This treatment is exact if Schrieffer-Wolff transformation is truncated to the first (linear) term in its series expansion, but real systems

will have an error due to the finite coupling strength. In this section, we describe how we partially compensate for higher-order errors by performing an optimization in a larger system consisting of multiple coupled unit cells (Figure 5.S4a) subject to continuity boundary conditions, within the context of the zero group velocity material.

As an example, we consider a finite element model consisting of two unit cells of the zero group velocity material, where each unit cell is made of two plates (Fig. 5.3c). We use Comsol Multiphysics to determine the system's eigenmodes and eigenfrequencies at our frequency of interest. Since the system consists of four plates, and each plate contains two modes in that frequency range (Fig 5.S4b), the problem requires the computation of eight eigenmodes of the coupled structure. We then determine the coupling matrix between local modes by utilizing the same procedure as in the case with two plates: We first express the coupled eigenmodes in terms of our local basis (Fig 5.S4b), by probing the displacement field over the test area of each plate (Fig. 5.1c) and identifying the linear combination of the basis modes that provides the best least-square approximation of the displacement field in the test area (using a Moore-Penrose pseudoinverse). Then we combine the eigenfrequencies and eigenmodes in the local basis representation to determine the reduced-order coupling matrix V^R for the system.

To minimize the error in the system's reduced dynamical matrix (Fig 5.S3c), we utilize a gradient-based method. We parameterize our geometry by allowing the beam locations, thicknesses and angles, as well as the hole locations and radii to change. We then determine the coupling matrix for the original system and for modified systems where we introduce a small change (0.03 mm) in each of the system's parameters. This allows us to assemble a Jacobian matrix J that relates small changes in the geometry to small changes in the coupling matrix. The direction of maximum error descent is given by $\vec{g} = -\left(\vec{k} - \vec{k}_T\right)^T J$, where $\vec{k}$ is a 64-components column vector containing the elements of the coupling matrix V^R, while $\vec{k}_T$ contains the elements of the target matrix. We then identify the optimal amount of change in the direction of $\vec{g}$ by minimizing $\left|\vec{k} + J\alpha\vec{g} - \vec{k}_T\right|$ with respect to α. We then apply this change in the model and recompute the error. Since the Jacobian matrix does not change significantly between gradient iterations, we evaluate it only once at the beginning of the

optimization process. Due to the presence of long-range interactions, the optimization algorithm is not able to completely match the system's dynamical matrix V^R to the objective mass-spring model K_{Target} (Fig 5.S4d). This additional optimization step greatly improves the agreement between the metamaterial's response and the target model, reducing the root mean square error in the dispersion relation fourfold from 20.4 Hz (Fig 5.S4e) to 5.1 Hz (Fig 5.S4f).

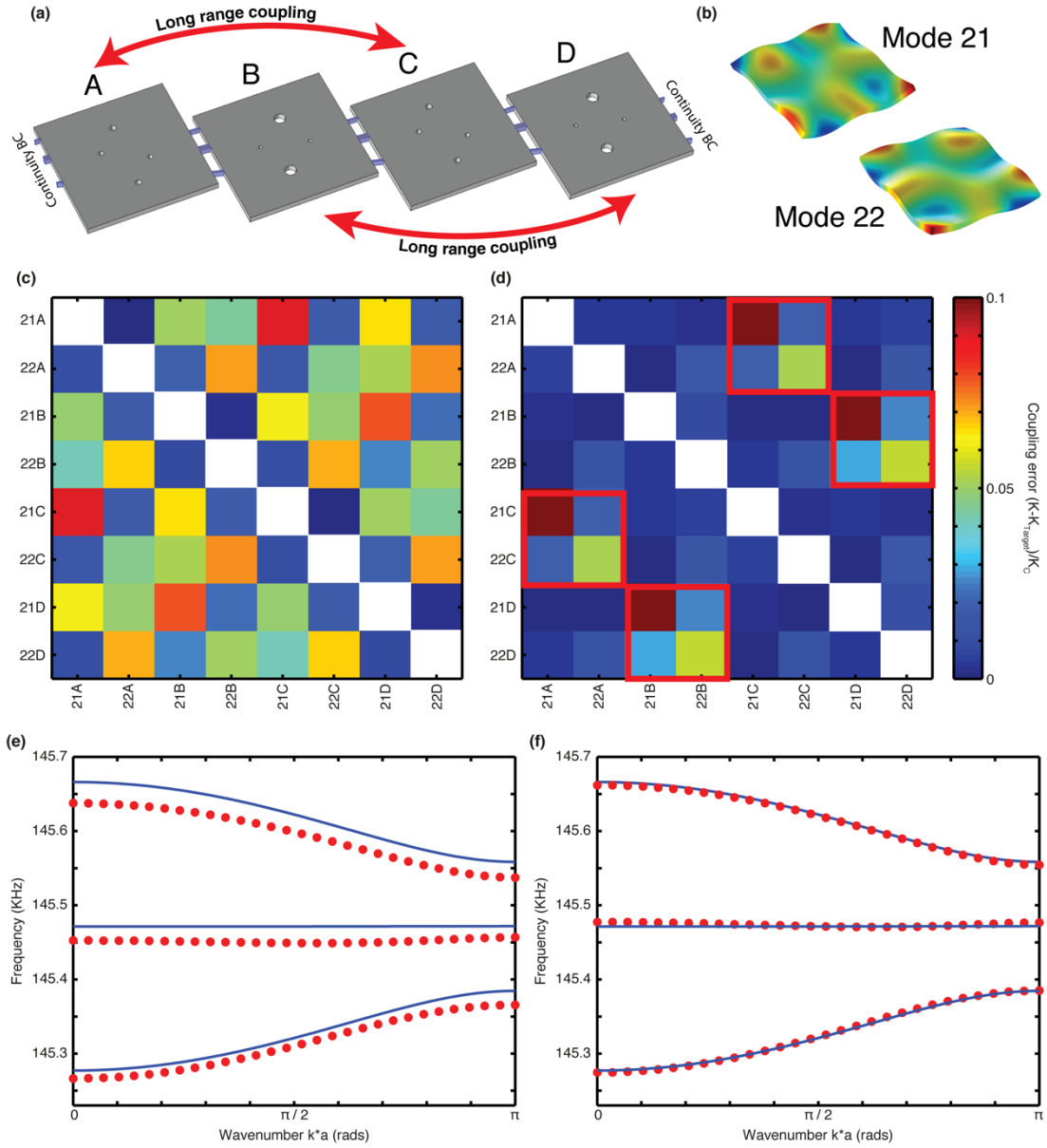

FIG. 5.S4: *Higher-order error compensation.* **(a)** Finite element model used in the coupled optimization scheme. The model consists of four plates (2 unit cells) subject to continuity boundary conditions. **(b)** Eigenmode basis used to describe the displacement of the coupled plates. The eigenmodes correspond to a free plate. **(c).** Magnitude of the error between the objective inter-modal coupling

stiffnesses and the coupling stiffnesses determined from the finite element model in panel **a**. **(d)** Magnitude of the coupling error after the optimization. The red squares indicate long-range interactions. **(e)** Band structure of the lattice before the optimization. **(f)** Band structure of the lattice after the optimization. In **e** and **f** the blue lines are the analytical predictions from the objective mass-spring model and the red dots correspond to the finite element simulation on the designed physical system.

Supplementary: Evaluation of the topological insulator design

To evaluate the behavior of the designed topological insulator metamaterial, we compare its modal properties to those of the mass-spring model. The eigenfrequency analysis of the physical system agrees well with the mass-spring analytical model (Fig. 5.S5a), and shows two bulk band gaps. This is confirmed by calculating the localization of each mode, defined as its strain energy summed over the unit cells on the edge, normalized by the total strain energy of the mode over the entire finite metamaterial. The localization of both the mass-spring model and designed metamaterial show almost complete localization on the boundary unit cells within the two bands identified in the eigenfrequency analysis. An example mode within the first bulk band gap of the mass-spring model clearly shows the edge mode (Fig. 5.S5b). Figure 5.S6 shows four other example modes within both bulk band gaps in the physical system. The designed topological insulator metamaterial overall shows excellent agreement with the behavior of the corresponding mass-spring model.

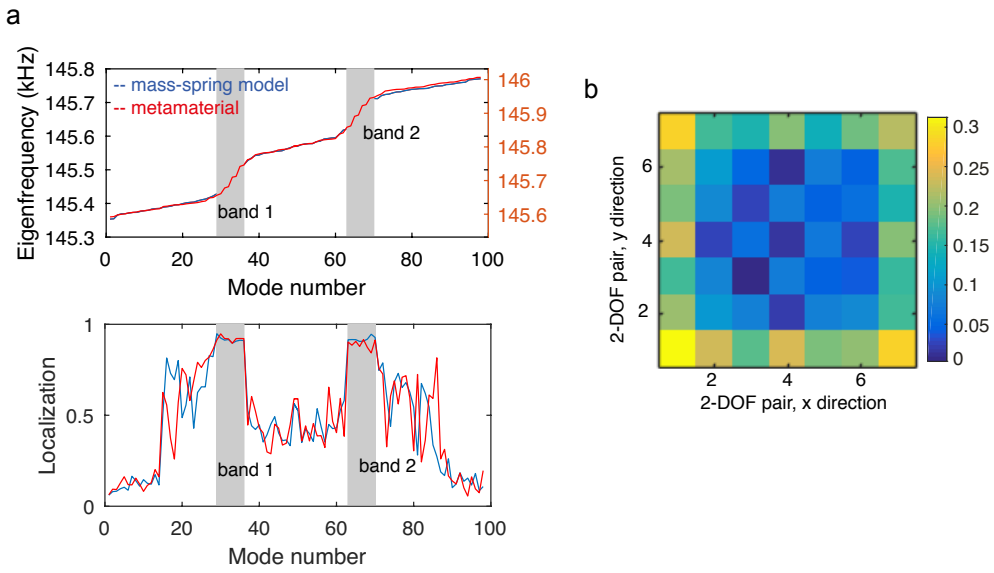

FIG. 5.S5: *Topological insulator mass-spring model compared to metamaterial.* **(a)** Eigenfrequency analysis and energy localization of mass-spring model compared to the designed metamaterial, both showing two bands of topologically protected edge modes. **(b)** Topologically protected edge mode of mass-spring model from Fig. 5.4a, within band 1. The same mode number is shown in the metamaterial results in Fig. 5.4d. Each pixel corresponds to a pair of degenerate modes.

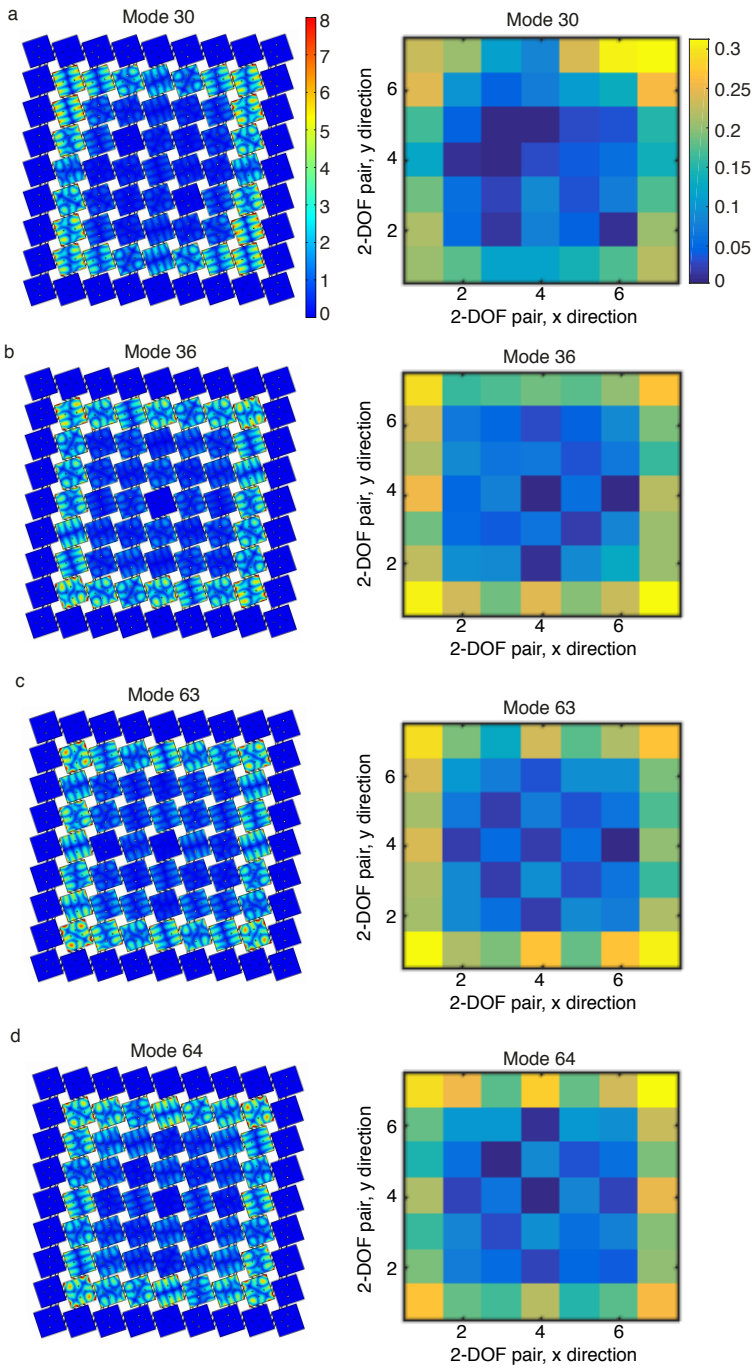

FIG 5.S6: *Four examples of topologically protected edge modes of the designed metamaterial (left) and mass-spring model* (right). **(a)** Mode 30 and **(b)** mode 36 are within the first topologically protected band, and **(c)** mode 63 and **(d)** mode 64 are within the second topologically protected band. The color bars shown in **a** apply to all plots, and are shown in arbitrary units of modal displacements.

Summary, conclusions and outlook

This thesis has investigated, theoretically and experimentally, the nonlinear dynamics of low-dimensional systems that act as models of energy-converting metamaterials. Here I present a brief review of the main conclusions, potential impact and proposed future work.

This work started by investigating the quasi-static and dynamic responses of nonlinear lattices subject to a localized harmonic excitation. In the quasi-static regime, it has been shown that applying an external harmonic excitation tunes the mechanical force-displacement response of the lattice. This mechanical response can reach extreme values, and include regions of negative, zero or infinite stiffness as well as present zero-frequency bands gaps and tunable damping. The harmonic excitation is characterized by two degrees of freedom: frequency and amplitude. This allows us to select which individual displacement region will be modified in the force-displacement relation, a degree of tunability that is not available in alternative stiffness tuning mechanisms. For certain types of interaction potentials, excitation forces above a threshold value result in energy transfer from the excited particle to an extended lattice mode, as it has been explored in Chapter 3. In this regime, our lattice's dynamics are analogous to an optomechanical system, and can be used to convert energy from one or multiple excitation sources into a single coherent oscillation of the lattice, with a tunable frequency and phase. The thesis has continued by investigating the response of this class of nonlinear systems under stochastic excitation. This work has been done on a different nonlinear system: a coupled string-cantilever structure, due quality factor requirements. Under appropriate conditions, the system behaves as a stochastic heat engine, producing work from a temperature difference, or as a refrigerator/heat pump, that transfers energy against a thermal gradient while consuming external work or heat. The thesis concludes with an algorithm to translate discrete models into material geometries, that can be used to implement a variety of systems such as plate wave lenses or topological insulators.

The results presented in this thesis offer significant potential for practical applications. The excitation-induced zero frequency band gaps demonstrated in driven nonlinear lattices can be used for vibration mitigation in the low range of the frequency spectrum, the hardest

region to filter. Frequency converting metamaterials can be used in vibration harvesting, to aggregate energy from multiple incoherent sources. The same type of nonlinear system, when subject to stochastic excitations, presents an ideal platform for the experimental study stochastic thermodynamics. However, in order to realize these applications, several issues must be addressed. First, the quasistatic stiffness changes presented in chapter 2 and the dynamic frequency conversion phenomena discussed in chapter 3 have been demonstrated in one-dimensional lattices containing a small number of particles. Practical devices would require a larger number of particles in order to have a significant usable displacement range for the tunable-stiffness system, or a significant output power in frequency converting and thermal engine systems. Increasing the size of the system may introduce emergent phenomena such as synchronization or phase transitions. These issues should be addressed in future work, since they are relevant for practical applications and may offer a peek into the transition between stochastic and conventional thermodynamics.

A separate issue that must be investigated is the cause of the low efficiency in the frequency converting processes described Chapter 3 and in the stochastic heat engine described in Chapter 4. Future studies need to identify the dependence of the conversion efficiency on the system's parameters, and particularly on the type of nonlinear interaction. An interesting fundamental question arising from this work is that of identifying which nonlinear interaction potentials give rise to nontrivial thermodynamic properties, and how the nonlinear dynamics and the thermodynamics are connected. This is relevant from a fundamental point of view, and may also inform the design of materials with novel thermodynamic performances.

Finally, the metamaterial geometry generation algorithm discussed in Chapter 5 leaves several issues for future work. First, the theoretical predictions should be validated experimentally. While the dimensions and features of the designed materials are within the range of conventional fabrication technologies, effects such as losses or manufacturing non-idealities may limit the performance of the resulting materials. Second, the design algorithm should be augmented to include nonlinear effects. The incorporation of a quadratic nonlinear term alone would enable the production of a dramatically larger variety of devices, including transistors, logic gates and energy converting systems such as those discussed in Chapters 3 and 4. Third, future studies should explore photonic equivalents of this algorithm. Photonic

systems are promising because, due to the extremely high frequency of light, they have the potential to enable ultra-fast information processing.

References

1. Seifert, U., *Stochastic thermodynamics, fluctuation theorems and molecular machines.* Reports on Progress in Physics, 2012. **75**(12): p. 126001.
2. Liu, Z., et al., *Locally Resonant Sonic Materials.* Science, 2000. **289**(5485): p. 1734-1736.
3. Brodt, M. and R. Lakes, *Composite materials which exhibit high stiffness and high viscoelastic damping.* Journal of Composite Materials, 1995. **29**(14): p. 1823-1833.
4. Pendry, J.B., *Negative Refraction Makes a Perfect Lens.* Physical Review Letters, 2000. **85**(18): p. 3966-3969.
5. Ma, H.F. and T.J. Cui, *Three-dimensional broadband and broad-angle transformation-optics lens.* Nature Communications, 2010. **1**: p. 124.
6. Kundtz, N. and D.R. Smith, *Extreme-angle broadband metamaterial lens.* Nat Mater, 2010. **9**(2): p. 129-132.
7. Do-Hoon, K. and H.W. Douglas, *Transformation optical designs for wave collimators, flat lenses and right-angle bends.* New Journal of Physics, 2008. **10**(11): p. 115023.
8. Schurig, D., et al., *Metamaterial Electromagnetic Cloak at Microwave Frequencies.* Science, 2006. **314**(5801): p. 977-980.
9. Ergin, T., et al., *Three-Dimensional Invisibility Cloak at Optical Wavelengths.* Science, 2010. **328**(5976): p. 337-339.
10. Li, J. and J.B. Pendry, *Hiding under the Carpet: A New Strategy for Cloaking.* Physical Review Letters, 2008. **101**(20): p. 203901.
11. Chen, H. and C.T. Chan, *Acoustic cloaking in three dimensions using acoustic metamaterials.* Applied Physics Letters, 2007. **91**(18): p. 183518.
12. Chen, Z., et al., *Metamaterials-based enhanced energy harvesting: A review.* Physica B: Condensed Matter, 2014. **438**: p. 1-8.
13. Carrara, M., et al., *Metamaterial Concepts for Structure-Borne Wave Energy Harvesting: Focusing, Funneling, and Localization.* 2012(45103): p. 891-896.
14. Porter, M.A., P.G. Kevrekidis, and C. Daraio, *Granular crystals: Nonlinear dynamics meets materials engineering.* Physics Today, 2015. **68**(11): p. 44-50.
15. Zia, R., E. Praestgaard, and O. Mouritsen, *Getting more from pushing less: Negative specific heat and conductivity in nonequilibrium steady states.* American Journal of Physics, 2002. **70**(4): p. 384-392.
16. Pusz, W. and S.L. Woronowicz, *Passive states and KMS states for general quantum systems.* 1978: p. 273-290.
17. Lenard, A., *Thermodynamical proof of the Gibbs formula for elementary quantum systems.* Journal of Statistical Physics, 1978. **19**(6): p. 575-586.
18. Skrzypczyk, P., R. Silva, and N. Brunner, *Passivity, complete passivity, and virtual temperatures.* Physical Review E, 2015. **91**(5): p. 052133.
19. Bravyi, S., D.P. DiVincenzo, and D. Loss, *Schrieffer–Wolff transformation for quantum many-body systems.* Annals of Physics, 2011. **326**(10): p. 2793-2826.
20. Florijn, B., C. Coulais, and M. van Hecke, *Programmable Mechanical Metamaterials.* Physical Review Letters, 2014. **113**(17): p. 175503.
21. Jaglinski, T., et al., *Composite Materials with Viscoelastic Stiffness Greater Than Diamond.* Science, 2007. **315**(5812): p. 620-622.

22. Majidi, C. and R.J. Wood, *Tunable elastic stiffness with microconfined magnetorheological domains at low magnetic field.* Applied Physics Letters, 2010. **97**(16): p. 164104.
23. Lee, C.M., V.N. Goverdovskiy, and A.I. Temnikov, *Design of springs with "negative" stiffness to improve vehicle driver vibration isolation.* Journal of Sound and Vibration, 2007. **302**(4–5): p. 865-874.
24. Gantzounis, G., et al., *Granular metamaterials for vibration mitigation.* Journal of Applied Physics, 2013. **114**(9): p. 093514.
25. Kippenberg, T.J. and K.J. Vahala, *Cavity Opto-Mechanics.* Optics Express, 2007. **15**(25): p. 17172-17205.
26. Aspelmeyer, M., T.J. Kippenberg, and F. Marquardt, *Cavity optomechanics.* Reviews of Modern Physics, 2014. **86**(4): p. 1391-1452.
27. He, M., et al., *Theoretical analysis for optomechanical all-optical transistor.* Frontiers of Optoelectronics, 2016. **9**(3): p. 406-411.
28. Zhang, K., F. Bariani, and P. Meystre, *Quantum Optomechanical Heat Engine.* Physical Review Letters, 2014. **112**(15): p. 150602.
29. Blickle, V. and C. Bechinger, *Realization of a micrometre-sized stochastic heat engine.* Nat Phys, 2012. **8**(2): p. 143-146.
30. Roßnagel, J., et al., *A single-atom heat engine.* Science, 2016. **352**(6283): p. 325-329.
31. Süsstrunk, R. and S.D. Huber, *Observation of phononic helical edge states in a mechanical topological insulator.* Science, 2015. **349**(6243): p. 47-50.
32. Lamb, H., *On Group - Velocity.* Proceedings of the London Mathematical Society, 1904. s**2-1**(1): p. 473-479.
33. Veselago, V.G., *The electrodynamics of substances with simultaneously negative values of and μ.* Soviet physics uspekhi, 1968. **10**(4): p. 509.
34. Kabashin, A.V., et al., *Plasmonic nanorod metamaterials for biosensing.* Nat Mater, 2009. **8**(11): p. 867-871.
35. Al-Naib, I.A.I., C. Jansen, and M. Koch, *Thin-film sensing with planar asymmetric metamaterial resonators.* Applied Physics Letters, 2008. **93**(8): p. 083507.
36. O'Hara, J.F., et al., *Thin-film sensing with planar terahertz metamaterials: sensitivity and limitations.* Optics Express, 2008. **16**(3): p. 1786-1795.
37. Wang, B., et al., *Experiments on wireless power transfer with metamaterials.* Applied Physics Letters, 2011. **98**(25): p. 254101.
38. Bingnan, W., T. Nishino, and T. Koon Hoo. *Wireless power transmission efficiency enhancement with metamaterials*. in *2010 IEEE International Conference on Wireless Information Technology and Systems*. 2010.
39. Choi, J. and C.H. Seo, *High-efficiency wireless energy transmission using magnetic resonance based on negative refractive index metamaterial.* Progress In Electromagnetics Research, 2010. **106**: p. 33-47.
40. Prat-Camps, J., C. Navau, and A. Sanchez, *A Magnetic Wormhole.* Scientific Reports, 2015. **5**: p. 12488.
41. Greenleaf, A., et al., *Cloaking Devices, Electromagnetic Wormholes, and Transformation Optics.* SIAM Review, 2009. **51**(1): p. 3-33.
42. Pendry, J.B., D. Schurig, and D.R. Smith, *Controlling Electromagnetic Fields.* Science, 2006. **312**(5781): p. 1780.

43. Moser, H.O., et al., *Terahertz Response of a Microfabricated Rod\char21{}Split-Ring-Resonator Electromagnetic Metamaterial.* Physical Review Letters, 2005. **94**(6): p. 063901.
44. Tao, H., et al., *Recent Progress in Electromagnetic Metamaterial Devices for Terahertz Applications.* IEEE Journal of Selected Topics in Quantum Electronics, 2011. **17**(1): p. 92-101.
45. Soukoulis, C.M. and M. Wegener, *Past achievements and future challenges in the development of three-dimensional photonic metamaterials.* Nat Photon, 2011. **5**(9): p. 523-530.
46. Liu, N., et al., *Three-dimensional photonic metamaterials at optical frequencies.* Nat Mater, 2008. **7**(1): p. 31-37.
47. Pendry, J., *Photonics: Metamaterials in the sunshine.* Nat Mater, 2006. **5**(8): p. 599-600.
48. Li, J. and C.T. Chan, *Double-negative acoustic metamaterial.* Physical Review E, 2004. **70**(5): p. 055602.
49. Liang, Z. and J. Li, *Extreme Acoustic Metamaterial by Coiling Up Space.* Physical Review Letters, 2012. **108**(11): p. 114301.
50. Daniel, T. and S.-D. José, *Acoustic metamaterials for new two-dimensional sonic devices.* New Journal of Physics, 2007. **9**(9): p. 323.
51. Zhang, S., L. Yin, and N. Fang, *Focusing Ultrasound with an Acoustic Metamaterial Network.* Physical Review Letters, 2009. **102**(19): p. 194301.
52. Fang, N., et al., *Ultrasonic metamaterials with negative modulus.* Nat Mater, 2006. **5**(6): p. 452-456.
53. Ding, Y., et al., *Metamaterial with Simultaneously Negative Bulk Modulus and Mass Density.* Physical Review Letters, 2007. **99**(9): p. 093904.
54. Liu, X.N., et al., *An elastic metamaterial with simultaneously negative mass density and bulk modulus.* Applied Physics Letters, 2011. **98**(25): p. 251907.
55. Rupin, M., et al., *Experimental Demonstration of Ordered and Disordered Multiresonant Metamaterials for Lamb Waves.* Physical Review Letters, 2014. **112**(23): p. 234301.
56. Yan, X., et al., *Focusing guided waves using surface bonded elastic metamaterials.* Applied Physics Letters, 2013. **103**(12): p. 121901.
57. Zhu, N.Q., X.Y. Shen, and J.P. Huang, *Converting the patterns of local heat flux via thermal illusion device.* AIP Advances, 2015. **5**(5): p. 053401.
58. Guenneau, S., C. Amra, and D. Veynante, *Transformation thermodynamics: cloaking and concentrating heat flux.* Optics Express, 2012. **20**(7): p. 8207-8218.
59. Moccia, M., et al., *Independent Manipulation of Heat and Electrical Current via Bifunctional Metamaterials.* Physical Review X, 2014. **4**(2): p. 021025.
60. Petiteau, D., et al., *Spectral effectiveness of engineered thermal cloaks in the frequency regime.* Scientific Reports, 2014. **4**: p. 7386.
61. Mousavi, S.H., A.B. Khanikaev, and Z. Wang, *Topologically protected elastic waves in phononic metamaterials.* Nature Communications, 2015. **6**: p. 8682.
62. Zhao, Y., et al., *Broadband diffusion metasurface based on a single anisotropic element and optimized by the Simulated Annealing algorithm.* Scientific Reports, 2016. **6**: p. 23896.
63. García-Chocano, V.M., et al., *Acoustic cloak for airborne sound by inverse design.* Applied Physics Letters, 2011. **99**(7): p. 074102.

64. Diaz, A.R. and O. Sigmund, *A topology optimization method for design of negative permeability metamaterials.* Structural and Multidisciplinary Optimization, 2010. **41**(2): p. 163-177.
65. Kern, D.J. and D.H. Werner, *A genetic algorithm approach to the design of ultra-thin electromagnetic bandgap absorbers.* Microwave and Optical Technology Letters, 2003. **38**(1): p. 61-64.
66. Della Giovampaola, C. and N. Engheta, *Digital metamaterials.* Nat Mater, 2014. **13**(12): p. 1115-1121.
67. Cui, T.J., et al., *Coding metamaterials, digital metamaterials and programmable metamaterials.* Light Sci Appl, 2014. **3**: p. e218.
68. Wang, J., et al., *Digital Metamaterials Using Graphene.* Plasmonics, 2015. **10**(5): p. 1141-1145.
69. Pendry, J.B., et al., *Transformation Optics and Subwavelength Control of Light.* Science, 2012. **337**(6094): p. 549-552.
70. Chen, H., C.T. Chan, and P. Sheng, *Transformation optics and metamaterials.* Nat Mater, 2010. **9**(5): p. 387-396.
71. Rahm, M., et al., *Design of electromagnetic cloaks and concentrators using form-invariant coordinate transformations of Maxwell's equations.* Photonics and Nanostructures - Fundamentals and Applications, 2008. **6**(1): p. 87-95.
72. Engheta, N., A. Salandrino, and A. Alù, *Circuit Elements at Optical Frequencies: Nanoinductors, Nanocapacitors, and Nanoresistors.* Physical Review Letters, 2005. **95**(9): p. 095504.
73. Engheta, N., *Circuits with Light at Nanoscales: Optical Nanocircuits Inspired by Metamaterials.* Science, 2007. **317**(5845): p. 1698-1702.
74. Alù, A., M.E. Young, and N. Engheta, *Design of nanofilters for optical nanocircuits.* Physical Review B, 2008. **77**(14): p. 144107.
75. Alù, A. and N. Engheta, *All Optical Metamaterial Circuit Board at the Nanoscale.* Physical Review Letters, 2009. **103**(14): p. 143902.
76. Süsstrunk, R. and S.D. Huber, *Classification of topological phonons in linear mechanical metamaterials.* Proceedings of the National Academy of Sciences, 2016. **113**(33): p. E4767-E4775.
77. Ramahi, O.M., et al., *Metamaterial particles for electromagnetic energy harvesting.* Applied Physics Letters, 2012. **101**(17): p. 173903.
78. Liu, X., et al., *Taming the Blackbody with Infrared Metamaterials as Selective Thermal Emitters.* Physical Review Letters, 2011. **107**(4): p. 045901.
79. Carrara, M., et al., *Metamaterial-inspired structures and concepts for elastoacoustic wave energy harvesting.* Smart Materials and Structures, 2013. **22**(6): p. 065004.
80. Wang, H., et al., *Highly efficient selective metamaterial absorber for high-temperature solar thermal energy harvesting.* Solar Energy Materials and Solar Cells, 2015. **137**: p. 235-242.
81. Hawkes, A.M., A.R. Katko, and S.A. Cummer, *A microwave metamaterial with integrated power harvesting functionality.* Applied Physics Letters, 2013. **103**(16): p. 163901.
82. Almoneef, T.S. and O.M. Ramahi, *Metamaterial electromagnetic energy harvester with near unity efficiency.* Applied Physics Letters, 2015. **106**(15): p. 153902.

83. Agarwal, K., et al. *Highly efficient wireless energy harvesting system using metamaterial based compact CP antenna*. in *2013 IEEE MTT-S International Microwave Symposium Digest (MTT)*. 2013.
84. Chihhui, W., et al., *Metamaterial-based integrated plasmonic absorber/emitter for solar thermo-photovoltaic systems.* Journal of Optics, 2012. **14**(2): p. 024005.
85. Boechler, N., et al., *Discrete Breathers in One-Dimensional Diatomic Granular Crystals.* Physical Review Letters, 2010. **104**(24): p. 244302.
86. Harne, R.L. and K.W. Wang, *A review of the recent research on vibration energy harvesting via bistable systems.* Smart Materials and Structures, 2013. **22**(2): p. 023001.
87. Quinn, D.D., A.F. Vakakis, and L.A. Bergman, *Vibration-Based Energy Harvesting With Essential Nonlinearities.* 2007(48027): p. 779-786.
88. Zheludev, N.I., *The Road Ahead for Metamaterials.* Science, 2010. **328**(5978): p. 582-583.
89. E. Fermi, J.P., S. Ulam, M. Tsingou, *Studies of nonlinear problems*, in *Los Alamos Scientific Laboratory Report*. 1955, Los Alamos.
90. Cugliandolo, L.F., *Out-of-equilibrium dynamics of classical and quantum complex systems.* Comptes Rendus Physique, 2013. **14**(8): p. 685-699.
91. Kevrekidis, P.G., *Non-linear waves in lattices: past, present, future.* IMA Journal of Applied Mathematics, 2011: p. hxr015.
92. Fordy, A.P. and J. Gibbons, *Integrable nonlinear Klein-Gordon equations and Toda lattices.* Communications in Mathematical Physics, 1980. **77**(1): p. 21-30.
93. Savin, A.V., Y. Zolotaryuk, and J.C. Eilbeck, *Moving kinks and nanopterons in the nonlinear Klein–Gordon lattice.* Physica D: Nonlinear Phenomena, 2000. **138**(3–4): p. 267-281.
94. Proville, L., *Biphonons in the Klein-Gordon lattice.* Physical Review B, 2005. **71**(10): p. 104306.
95. Kevrekidis, P., K. Rasmussen, and A. Bishop, *The discrete nonlinear Schrödinger equation: a survey of recent results.* International Journal of Modern Physics B, 2001. **15**(21): p. 2833-2900.
96. Kenkre, V. and D. Campbell, *Self-trapping on a dimer: time-dependent solutions of a discrete nonlinear Schrödinger equation.* Physical Review B, 1986. **34**(7): p. 4959.
97. Toda, M., *Vibration of a chain with nonlinear interaction.* Journal of the Physical Society of Japan, 1967. **22**(2): p. 431-436.
98. Nesterenko, V., *Propagation of nonlinear compression pulses in granular media.* Journal of Applied Mechanics and Technical Physics, 1983. **24**(5): p. 733-743.
99. Lazaridi, A. and V. Nesterenko, *Observation of a new type of solitary waves in a one-dimensional granular medium.* Journal of Applied Mechanics and Technical Physics, 1985. **26**(3): p. 405-408.
100. Nesterenko, V., *Dynamics of heterogeneous materials*. 2013: Springer Science & Business Media.
101. Sen, S., et al., *Solitary waves in the granular chain.* Physics Reports, 2008. **462**(2): p. 21-66.
102. Molerón, M., A. Leonard, and C. Daraio, *Solitary waves in a chain of repelling magnets.* Journal of Applied Physics, 2014. **115**(18): p. 184901.
103. Magyari, E., *Solitary waves along the compressible Heisenberg chain.* Journal of Physics C: Solid State Physics, 1982. **15**(32): p. L1159.

104. Yomosa, S., *Soliton excitations in deoxyribonucleic acid (DNA) double helices.* Physical Review A, 1983. **27**(4): p. 2120.
105. Daniel, M. and V. Vasumathi, *Perturbed soliton excitations in the DNA double helix.* Physica D: Nonlinear Phenomena, 2007. **231**(1): p. 10-29.
106. Scott, A.C., *Soliton oscillations in DNA.* Physical Review A, 1985. **31**(5): p. 3518.
107. Tchinang Tchameu, J.D., A.B. Togueu Motcheyo, and C. Tchawoua, *Mobility of discrete multibreathers in the exciton dynamics of the Davydov model with saturable nonlinearities.* Physical Review E, 2014. **90**(4): p. 043203.
108. Caspi, S. and E. Ben-Jacob, *Toy model studies of soliton-mediated protein folding and conformation changes.* EPL (Europhysics Letters), 1999. **47**(4): p. 522.
109. Pankov, A., *Gap solitons in periodic discrete nonlinear Schrodinger equations II: a generalized Nehari manifold approach.* Discrete and Continuous Dynamical Systems, 2007. **19**(2): p. 419.
110. Job, S., et al., *How Hertzian solitary waves interact with boundaries in a 1D granular medium.* Physical review letters, 2005. **94**(17): p. 178002.
111. Sen, S. and M. Manciu, *Discrete Hertzian chains and solitons.* Physica A: Statistical Mechanics and its Applications, 1999. **268**(3): p. 644-649.
112. Daraio, C., et al., *Strongly nonlinear waves in a chain of Teflon beads.* Physical Review E, 2005. **72**(1): p. 016603.
113. Daraio, C. and V.F. Nesterenko, *Strongly nonlinear wave dynamics in a chain of polymer coated beads.* Physical Review E, 2006. **73**(2): p. 026612.
114. Chong, C., et al., *Damped-driven granular chains: An ideal playground for dark breathers and multibreathers.* Physical Review E, 2014. **89**(3): p. 032924.
115. Cuevas–Maraver, J., P.G. Kevrekidis, and D.E. Pelinovsky, *Nonlinear Instabilities of Multi-Site Breathers in Klein–Gordon Lattices.* Studies in Applied Mathematics, 2015.
116. Theocharis, G., et al., *Intrinsic energy localization through discrete gap breathers in one-dimensional diatomic granular crystals.* Physical Review E, 2010. **82**(5): p. 056604.
117. Theocharis, G., et al., *Localized breathing modes in granular crystals with defects.* Physical Review E, 2009. **80**(6): p. 066601.
118. Boechler, N., et al., *Tunable vibrational band gaps in one-dimensional diatomic granular crystals with three-particle unit cells.* Journal of Applied Physics, 2011. **109**(7): p. 074906.
119. Chen, A.L. and Y.-S. Wang, *Study on band gaps of elastic waves propagating in one-dimensional disordered phononic crystals.* Physica B: Condensed Matter, 2007. **392**(1–2): p. 369-378.
120. Boechler, N., et al., *Tunable vibrational band gaps in one-dimensional diatomic granular crystals with three-particle unit cells.* Journal of Applied Physics, 2011. **109**(7): p. 074906.
121. Terraneo, M., M. Peyrard, and G. Casati, *Controlling the Energy Flow in Nonlinear Lattices: A Model for a Thermal Rectifier.* Physical Review Letters, 2002. **88**(9): p. 094302.
122. Li, X.-F., et al., *Tunable Unidirectional Sound Propagation through a Sonic-Crystal-Based Acoustic Diode.* Physical Review Letters, 2011. **106**(8): p. 084301.
123. Boechler, N., G. Theocharis, and C. Daraio, *Bifurcation-based acoustic switching and rectification.* Nat Mater, 2011. **10**(9): p. 665-668.
124. Yasuda, H., et al., *Shock and Rarefaction Waves in Generalized Hertzian Contact Models.* ArXiv, 2016.

125. Daraio, C., et al., *Energy Trapping and Shock Disintegration in a Composite Granular Medium.* Physical Review Letters, 2006. **96**(5): p. 058002.
126. Kevrekidis, P.G., et al., *Interaction of traveling waves with mass-with-mass defects within a Hertzian chain.* Physical Review E, 2013. **87**(4): p. 042911.
127. Hong, J., *Universal Power-Law Decay of the Impulse Energy in Granular Protectors.* Physical Review Letters, 2005. **94**(10): p. 108001.
128. Lydon, J., M. Serra-Garcia, and C. Daraio, *Local to Extended Transitions of Resonant Defect Modes.* Physical Review Letters, 2014. **113**(18): p. 185503.
129. Serra-Garcia, M., J. Lydon, and C. Daraio, *Extreme stiffness tunability through the excitation of nonlinear defect modes.* Physical Review E, 2016. **93**(1): p. 010901.
130. Allein, F., et al., *Tunable magneto-granular phononic crystals.* Applied Physics Letters, 2016. **108**(16): p. 161903.
131. Li, F., et al., *Tunable phononic crystals based on cylindrical Hertzian contact.* Applied Physics Letters, 2012. **101**(17): p. 171903.
132. Doney, R. and S. Sen, *Decorated, Tapered, and Highly Nonlinear Granular Chain.* Physical Review Letters, 2006. **97**(15): p. 155502.
133. Spadoni, A. and C. Daraio, *Generation and control of sound bullets with a nonlinear acoustic lens.* Proceedings of the National Academy of Sciences, 2010. **107**(16): p. 7230-7234.
134. Donahue, C.M., et al., *Experimental realization of a nonlinear acoustic lens with a tunable focus.* Applied Physics Letters, 2014. **104**(1): p. 014103.
135. Li, K. and P. Rizzo, *Energy harvesting using an array of granules.* Journal of Vibration and Acoustics, 2015. **137**(4): p. 041002.
136. Chong, C., et al., *Nonlinear vibrational-state excitation and piezoelectric energy conversion in harmonically driven granular chains.* Physical Review E, 2016. **93**(5): p. 052203.
137. Cabaret, J., V. Tournat, and P. Béquin, *Amplitude-dependent phononic processes in a diatomic granular chain in the weakly nonlinear regime.* Physical Review E, 2012. **86**(4): p. 041305.
138. Li, F., et al., *Granular acoustic switches and logic elements.* Nature Communications, 2014. **5**: p. 5311.
139. Man, Y., et al., *Defect modes in one-dimensional granular crystals.* Physical Review E, 2012. **85**(3): p. 037601.
140. Jarzynski, C., *Equalities and inequalities: irreversibility and the second law of thermodynamics at the nanoscale.* Annu. Rev. Condens. Matter Phys., 2011. **2**(1): p. 329-351.
141. Udo, S., *Stochastic thermodynamics, fluctuation theorems and molecular machines.* Reports on Progress in Physics, 2012. **75**(12): p. 126001.
142. Sekimoto, K., *Stochastic Energetics*. Lecture Notes In Physics, ed. Springer-Verlag. 2010, Heidelberg: Springer-Verlag.
143. Van den Broeck, C. and M. Esposito, *Ensemble and trajectory thermodynamics: A brief introduction.* Physica A: Statistical Mechanics and its Applications, 2015. **418**: p. 6-16.
144. Seifert, U., *Entropy Production along a Stochastic Trajectory and an Integral Fluctuation Theorem.* Physical Review Letters, 2005. **95**(4): p. 040602.
145. Brown, R., *XXVII. A brief account of microscopical observations made in the months of June, July and August 1827, on the particles contained in the pollen of plants; and on*

the general existence of active molecules in organic and inorganic bodies. Philosophical Magazine Series 2, 1828. **4**(21): p. 161-173.
146. Einstein, A., *Über die von der molekularkinetischen Theorie der Wärme geforderte Bewegung von in ruhenden Flüssigkeiten suspendierten Teilchen.* Annalen der Physik, 1905. **322**(8): p. 549-560.
147. Smoluchowski, M.v., *Experimentell nachweisbare, der ublichen thermodynamik widersprechende molekular-phanomene.* Physikalische Zeitschrift, 1912. **8**(84): p. 1069-1080.
148. Maxwell, J.C., *Theory of Heat*. 1871, London: Longmans, Green & Co.
149. Feynman, R.P., Leighton, R. B. and Sands, M, *The Feynman Lectures on Physics I*. 1963, Addison-Wesley: Reading, MA.
150. Berut, A., et al., *Experimental verification of Landauer/'s principle linking information and thermodynamics.* Nature, 2012. **483**(7388): p. 187-189.
151. Landauer, R., *Irreversibility and Heat Generation in the Computing Process.* IBM Journal of Research and Development, 1961. **5**(3): p. 183-191.
152. Parrondo, J.M.R., J.M. Horowitz, and T. Sagawa, *Thermodynamics of information.* Nat Phys, 2015. **11**(2): p. 131-139.
153. Deffner, S. and C. Jarzynski, *Information Processing and the Second Law of Thermodynamics: An Inclusive, Hamiltonian Approach.* Physical Review X, 2013. **3**(4): p. 041003.
154. Barato, A.C. and U. Seifert, *Stochastic thermodynamics with information reservoirs.* Physical Review E, 2014. **90**(4): p. 042150.
155. Toyabe, S., et al., *Experimental demonstration of information-to-energy conversion and validation of the generalized Jarzynski equality.* Nat Phys, 2010. **6**(12): p. 988-992.
156. Christian Van den, B., S. Shin-ichi, and S. Udo, *Focus on stochastic thermodynamics.* New Journal of Physics, 2016. **18**(2): p. 020401.
157. Evans, D.J., E.G.D. Cohen, and G.P. Morriss, *Probability of second law violations in shearing steady states.* Physical Review Letters, 1993. **71**(15): p. 2401-2404.
158. Postma, H.W.C., et al., *Dynamic range of nanotube- and nanowire-based electromechanical systems.* Applied Physics Letters, 2005. **86**(22): p. 223105.
159. Cleland, A.N., *Thermomechanical noise limits on parametric sensing with nanomechanical resonators.* New Journal of Physics, 2005. **7**(1): p. 235.
160. Hänggi, P. and F. Marchesoni, *Artificial Brownian motors: Controlling transport on the nanoscale.* Reviews of Modern Physics, 2009. **81**(1): p. 387-442.
161. Crooks, G.E., *Entropy production fluctuation theorem and the nonequilibrium work relation for free energy differences.* Physical Review E, 1999. **60**(3): p. 2721-2726.
162. Jarzynski, C., *Nonequilibrium Equality for Free Energy Differences.* Physical Review Letters, 1997. **78**(14): p. 2690-2693.
163. Hatano, T. and S.-i. Sasa, *Steady-State Thermodynamics of Langevin Systems.* Physical Review Letters, 2001. **86**(16): p. 3463-3466.
164. Neri, M. and K. Yariv, *Statistical properties of entropy production derived from fluctuation theorems.* Journal of Statistical Mechanics: Theory and Experiment, 2010. **2010**(12): p. P12022.
165. Cleuren, B., C. Van den Broeck, and R. Kawai, *Fluctuation and Dissipation of Work in a Joule Experiment.* Physical Review Letters, 2006. **96**(5): p. 050601.
166. Kurchan, J., *Fluctuation theorem for stochastic dynamics.* Journal of Physics A: Mathematical and General, 1998. **31**(16): p. 3719.

167. van Zon, R. and E.G.D. Cohen, *Extension of the Fluctuation Theorem.* Physical Review Letters, 2003. **91**(11): p. 110601.
168. Carberry, D.M., et al., *Fluctuations and Irreversibility: An Experimental Demonstration of a Second-Law-Like Theorem Using a Colloidal Particle Held in an Optical Trap.* Physical Review Letters, 2004. **92**(14): p. 140601.
169. Jarzynski, C., *Hamiltonian Derivation of a Detailed Fluctuation Theorem.* Journal of Statistical Physics, 2000. **98**(1): p. 77-102.
170. Mossa, A., et al., *Dynamic force spectroscopy of DNA hairpins: I. Force kinetics and free energy landscapes.* Journal of Statistical Mechanics: Theory and Experiment, 2009. **2009**(02): p. P02060.
171. Manosas, M., et al., *Dynamic force spectroscopy of DNA hairpins: II. Irreversibility and dissipation.* Journal of Statistical Mechanics: Theory and Experiment, 2009. **2009**(02): p. P02061.
172. Liphardt, J., et al., *Equilibrium Information from Nonequilibrium Measurements in an Experimental Test of Jarzynski's Equality.* Science, 2002. **296**(5574): p. 1832-1835.
173. Collin, D., et al., *Verification of the Crooks fluctuation theorem and recovery of RNA folding free energies.* Nature, 2005. **437**(7056): p. 231-234.
174. Gebhardt, J.C.M., T. Bornschlögl, and M. Rief, *Full distance-resolved folding energy landscape of one single protein molecule.* Proceedings of the National Academy of Sciences, 2010. **107**(5): p. 2013-2018.
175. Nome, R.A., et al., *Axis-dependent anisotropy in protein unfolding from integrated nonequilibrium single-molecule experiments, analysis, and simulation.* Proceedings of the National Academy of Sciences, 2007. **104**(52): p. 20799-20804.
176. Shank, E.A., et al., *The folding cooperativity of a protein is controlled by its chain topology.* Nature, 2010. **465**(7298): p. 637-640.
177. Gelbwaser-Klimovsky, D. and G. Kurizki, *Work extraction from heat-powered quantized optomechanical setups.* Scientific Reports, 2015. **5**: p. 7809.
178. Komatsu, T.S., et al., *Exact Equalities and Thermodynamic Relations for Nonequilibrium Steady States.* Journal of Statistical Physics, 2015. **159**(6): p. 1237-1285.
179. Benenti, G., K. Saito, and G. Casati, *Thermodynamic Bounds on Efficiency for Systems with Broken Time-Reversal Symmetry.* Physical Review Letters, 2011. **106**(23): p. 230602.
180. Esposito, M., et al., *Efficiency at Maximum Power of Low-Dissipation Carnot Engines.* Physical Review Letters, 2010. **105**(15): p. 150603.
181. Humphrey, T.E., et al., *Reversible Quantum Brownian Heat Engines for Electrons.* Physical Review Letters, 2002. **89**(11): p. 116801.
182. Martinez, I.A., et al., *Brownian Carnot engine.* Nat Phys, 2016. **12**(1): p. 67-70.
183. Martínez, I.A., et al., *Adiabatic Processes Realized with a Trapped Brownian Particle.* Physical Review Letters, 2015. **114**(12): p. 120601.
184. Koski, J.V., et al., *On-Chip Maxwell's Demon as an Information-Powered Refrigerator.* Physical Review Letters, 2015. **115**(26): p. 260602.
185. Roßnagel, J., et al., *Nanoscale Heat Engine Beyond the Carnot Limit.* Physical Review Letters, 2014. **112**(3): p. 030602.
186. Krishnamurthy, S., et al., *A micrometre-sized heat engine operating between bacterial reservoirs.* Nat Phys, 2016. **12**(12): p. 1134-1138.

187. Szilard, L., *Über die Entropieverminderung in einem thermodynamischen System bei Eingriffen intelligenter Wesen.* Zeitschrift für Physik, 1929. **53**(11-12): p. 840-856.
188. Szilard, L., *On the decrease of entropy in a thermodynamic system by the intervention of intelligent beings.* Systems Research and Behavioral Science, 1964. **9**(4): p. 301-310.
189. Wang, G.M., et al., *Experimental Demonstration of Violations of the Second Law of Thermodynamics for Small Systems and Short Time Scales.* Physical Review Letters, 2002. **89**(5): p. 050601.
190. Trepagnier, E.H., et al., *Experimental test of Hatano and Sasa's nonequilibrium steady-state equality.* Proceedings of the National Academy of Sciences of the United States of America, 2004. **101**(42): p. 15038-15041.
191. Blickle, V., et al., *Thermodynamics of a Colloidal Particle in a Time-Dependent Nonharmonic Potential.* Physical Review Letters, 2006. **96**(7): p. 070603.
192. Schmiedl, T. and U. Seifert, *Efficiency at maximum power: An analytically solvable model for stochastic heat engines.* EPL (Europhysics Letters), 2008. **81**(2): p. 20003.
193. Strasberg, P., et al., *Thermodynamics of a Physical Model Implementing a Maxwell Demon.* Physical Review Letters, 2013. **110**(4): p. 040601.
194. Press, W.H., et al., *Numerical recipes in C*. Vol. 2. 1982: Cambridge Univ Press.
195. Rößler, A., *Runge–Kutta Methods for the Strong Approximation of Solutions of Stochastic Differential Equations.* SIAM Journal on Numerical Analysis, 2010. **48**(3): p. 922-952.
196. Queisser, H.J. and E.E. Haller, *Defects in Semiconductors: Some Fatal, Some Vital.* Science, 1998. **281**(5379): p. 945-950.
197. Montroll, E.W. and R.B. Potts, *Effect of Defects on Lattice Vibrations.* Physical Review, 1955. **100**(2): p. 525-543.
198. Chen, J.-H., et al., *Intrinsic and extrinsic performance limits of graphene devices on SiO2.* Nat Nano, 2008. **3**(4): p. 206-209.
199. Balandin, A.A., *Thermal properties of graphene and nanostructured carbon materials.* Nat Mater, 2011. **10**(8): p. 569-581.
200. Wagner, M., *Influence of Localized Modes on Thermal Conductivity.* Physical Review, 1963. **131**(4): p. 1443-1455.
201. Gavartin, E., et al., *Optomechanical Coupling in a Two-Dimensional Photonic Crystal Defect Cavity.* Physical Review Letters, 2011. **106**(20): p. 203902.
202. Zhu, X., et al., *Acoustic Cloaking by a Superlens with Single-Negative Materials.* Physical Review Letters, 2011. **106**(1): p. 014301.
203. Graeme, W.M., *New metamaterials with macroscopic behavior outside that of continuum elastodynamics.* New Journal of Physics, 2007. **9**(10): p. 359.
204. Zhang, S., C. Xia, and N. Fang, *Broadband Acoustic Cloak for Ultrasound Waves.* Physical Review Letters, 2011. **106**(2): p. 024301.
205. Wojnar, C.S. and D.M. Kochmann, *A negative-stiffness phase in elastic composites can produce stable extreme effective dynamic but not static stiffness.* Philosophical Magazine, 2013. **94**(6): p. 532-555.
206. Lapine, M., et al., *Magnetoelastic metamaterials.* Nat Mater, 2012. **11**(1): p. 30-33.
207. Dong, L., D.S. Stone, and R.S. Lakes, *Broadband viscoelastic spectroscopy measurement of mechanical loss and modulus of polycrystalline BaTiO3 vs. temperature and frequency.* physica status solidi (b), 2008. **245**(11): p. 2422-2432.
208. Kittel, C., *Introduction to solid state physics*. 1996: Wiley.

209. Martin, P., A.D. Mehta, and A.J. Hudspeth, *Negative hair-bundle stiffness betrays a mechanism for mechanical amplification by the hair cell.* Proceedings of the National Academy of Sciences, 2000. **97**(22): p. 12026-12031.
210. Thompson, J.M.T., */`Paradoxical/' mechanics under fluid flow.* Nature, 1982. **296**(5853): p. 135-137.
211. Lakes, R., *Stable singular or negative stiffness systems in the presence of energy flux.* Philosophical Magazine Letters, 2012. **92**(5): p. 226-234.
212. Nayfeh, A.H. and D.T. Mook, *Nonlinear Oscillations*. 2008: Wiley.
213. Karabalin, R.B., et al., *Signal Amplification by Sensitive Control of Bifurcation Topology.* Physical Review Letters, 2011. **106**(9): p. 094102.
214. Ibrahim, R.A., *Recent advances in nonlinear passive vibration isolators.* Journal of Sound and Vibration, 2008. **314**(3–5): p. 371-452.
215. Wang, P., et al., *Harnessing Buckling to Design Tunable Locally Resonant Acoustic Metamaterials.* Physical Review Letters, 2014. **113**(1): p. 014301.
216. Larouche, S., et al., *Experimental determination of the quadratic nonlinear magnetic susceptibility of a varactor-loaded split ring resonator metamaterial.* Applied Physics Letters, 2010. **97**(1): p. 011109.
217. Huang, D., E. Poutrina, and D.R. Smith, *Analysis of the power dependent tuning of a varactor-loaded metamaterial at microwave frequencies.* Applied Physics Letters, 2010. **96**(10): p. 104104.
218. Maasch, M., et al. *Varactor loaded tunable split ring resonators with simple biasing network*. in *Microwave Conference (GeMIC), 2011 German*. 2011.
219. Wang, F., O. Sigmund, and J.S. Jensen, *Design of materials with prescribed nonlinear properties.* Journal of the Mechanics and Physics of Solids, 2014. **69**: p. 156-174.
220. Vaezi, M., H. Seitz, and S. Yang, *A review on 3D micro-additive manufacturing technologies.* The International Journal of Advanced Manufacturing Technology, 2013. **67**(5-8): p. 1721-1754.
221. Meyers, R.A., *Mathematics of Complexity and Dynamical Systems*. 2011, New York: Springer-Verlag. 1858.
222. Hertz, H., *Ueber die Berührung fester elastischer Körper*, in *Journal für die reine und angewandte Mathematik (Crelle's Journal)*. 1882. p. 156.
223. Franken, P.A., et al., *Generation of Optical Harmonics.* Physical Review Letters, 1961. **7**(4): p. 118-119.
224. Jung, S.-M. and K.-S. Yun, *Energy-harvesting device with mechanical frequency-up conversion mechanism for increased power efficiency and wideband operation.* Applied Physics Letters, 2010. **96**(11): p. 111906.
225. Rarity, J.G., et al., *Two-photon interference in a Mach-Zehnder interferometer.* Physical Review Letters, 1990. **65**(11): p. 1348-1351.
226. Stolen, R.H., J.E. Bjorkholm, and A. Ashkin, *Phase-matched three-wave mixing in silica fiber optical waveguides.* Applied Physics Letters, 1974. **24**(7): p. 308-310.
227. Chen, Y.C., H.G. Winful, and J.M. Liu, *Subharmonic bifurcations and irregular pulsing behavior of modulated semiconductor lasers.* Applied Physics Letters, 1985. **47**(3): p. 208-210.
228. Nayfeh, A.H., *Nonlinear oscillations / Ali Hasan Nayfeh, Dean T. Mook*. Pure and applied mathematics (Wiley), ed. D.T. Mook. 1979, New York: Wiley.
229. Malatkar, P. and A.H. Nayfeh, *On the Transfer of Energy between Widely Spaced Modes in Structures.* Nonlinear Dynamics, 2003. **31**(2): p. 225-242.

230. Oh, K. and A.H. Nayfeh, *Nonlinear combination resonances in cantilever composite plates.* Nonlinear Dynamics, 1996. **11**(2): p. 143-169.
231. Ford, J., *The Fermi-Pasta-Ulam problem: Paradox turns discovery.* Physics Reports, 1992. **213**(5): p. 271-310.
232. Toda, M., *Wave Propagation in Anharmonic Lattices.* Journal of the Physical Society of Japan, 1967. **23**(3): p. 501-506.
233. Nesterenko, V.F., *Propagation of nonlinear compression pulses in granular media.* Journal of Applied Mechanics and Technical Physics, 1983. **24**(5): p. 733-743.
234. Daraio, C., et al., *Strongly nonlinear waves in a chain of Teflon beads.* Physical Review E, 2005. **72**(1): p. 016603.
235. Mankowsky, R., et al., *Nonlinear lattice dynamics as a basis for enhanced superconductivity in YBa2Cu3O6.5.* Nature, 2014. **516**(7529): p. 71-73.
236. Serra-Garcia, M., et al., *Mechanical Autonomous Stochastic Heat Engine.* Physical Review Letters, 2016. **117**(1): p. 010602.
237. Hossein-Zadeh, M. and K.J. Vahala, *An Optomechanical Oscillator on a Silicon Chip.* IEEE Journal of Selected Topics in Quantum Electronics, 2010. **16**(1): p. 276-287.
238. Carmon, T., et al., *Temporal Behavior of Radiation-Pressure-Induced Vibrations of an Optical Microcavity Phonon Mode.* Physical Review Letters, 2005. **94**(22): p. 223902.
239. Rokhsari, H., et al., *Radiation-pressure-driven micro-mechanical oscillator.* Optics Express, 2005. **13**(14): p. 5293-5301.
240. Ozyuzer, L., et al., *Emission of Coherent THz Radiation from Superconductors.* Science, 2007. **318**(5854): p. 1291-1293.
241. Komatsu, T., et al., *Exact Equalities and Thermodynamic Relations for Nonequilibrium Steady States.* Journal of Statistical Physics, 2015. **159**(6): p. 1237-1285.
242. Martinez, I.A., et al., *Brownian Carnot engine.* Nat Phys, 2015. **advance online publication**.
243. Mandal, D. and C. Jarzynski, *Work and information processing in a solvable model of Maxwell's demon.* Proceedings of the National Academy of Sciences of the United States of America, 2012. **109**(29): p. 11641-11645.
244. Zhiyue Lu, D.M., Christopher Jarzynski, *Engineering Maxwell's demon.* Physics Today, 2014: p. 60.
245. Strasberg, P., et al., *Second laws for an information driven current through a spin valve.* Physical Review E, 2014. **90**(6): p. 062107.
246. Utsumi, Y. and T. Taniguchi, *Fluctuation Theorem for a Small Engine and Magnetization Switching by Spin Torque.* Physical Review Letters, 2015. **114**(18): p. 186601.
247. Horowitz, J.M. and M. Esposito, *Thermodynamics with Continuous Information Flow.* Physical Review X, 2014. **4**(3): p. 031015.
248. Bennett, C., *The thermodynamics of computation—a review.* International Journal of Theoretical Physics, 1982. **21**(12): p. 905-940.
249. Hoppenau, J. and A. Engel, *On the energetics of information exchange.* EPL (Europhysics Letters), 2014. **105**(5): p. 50002.
250. Viktor, H., *An exactly solvable model of a stochastic heat engine: optimization of power, power fluctuations and efficiency.* Journal of Statistical Mechanics: Theory and Experiment, 2014. **2014**(5): p. P05022.

251. Esposito, M., et al., *Stochastically driven single-level quantum dot: A nanoscale finite-time thermodynamic machine and its various operational modes.* Physical Review E, 2012. **85**(3).
252. Newland, D.E., *Calculation of power flow between coupled oscillators.* Journal of Sound and Vibration, 1966. **3**(3): p. 262-276.
253. Mari, A. and J. Eisert, *Cooling by Heating: Very Hot Thermal Light Can Significantly Cool Quantum Systems.* Physical Review Letters, 2012. **108**(12): p. 120602.
254. Mari, A., A. Farace, and V. Giovannetti, *Quantum optomechanical piston engines powered by heat.* Journal of Physics B: Atomic, Molecular and Optical Physics, 2015. **48**(17): p. 175501.
255. Ebeling, W., Sokolov, I., *Statistical thermodynamics and stochastic theory of nonequilibrium systems*. 2005, Singapore: World Scientific.
256. Ciliberto, S., et al., *Heat Flux and Entropy Produced by Thermal Fluctuations.* Physical Review Letters, 2013. **110**(18): p. 180601.
257. Simon, M.S., J.M. Sancho, and K. Lindenberg, *Transport and diffusion of underdamped Brownian particles in random potentials.* European Physical Journal B, 2014. **87**(9): p. 10.
258. Langevin, P., *Sur la theorie du mouvement brownien.* C. R. Acad. Sci. (Paris), 1908. **146**: p. 530-533.
259. Lemons, D.S. and A. Gythiel, *Paul Langevin's 1908 paper "On the Theory of Brownian Motion" ["Sur la théorie du mouvement brownien," C. R. Acad. Sci. (Paris) 146, 530–533 (1908)].* American Journal of Physics, 1997. **65**(11): p. 1079-1081.
260. Sekimoto, K., *Langevin Equation and Thermodynamics.* Progress of Theoretical Physics Supplement, 1998. **130**: p. 17-27.
261. Linden, N., S. Popescu, and P. Skrzypczyk, *How Small Can Thermal Machines Be? The Smallest Possible Refrigerator.* Physical Review Letters, 2010. **105**(13): p. 4.
262. Levy, A. and R. Kosloff, *Quantum Absorption Refrigerator.* Physical Review Letters, 2012. **108**(7): p. 5.
263. Correa, L.A., et al., *Quantum-enhanced absorption refrigerators.* Scientific Reports, 2014. **4**: p. 3949.
264. Silva, R., P. Skrzypczyk, and N. Brunner, *Small quantum absorption refrigerator with reversed couplings.* Physical Review E, 2015. **92**(1): p. 6.
265. Ekinci, K.L., Y.T. Yang, and M.L. Roukes, *Ultimate limits to inertial mass sensing based upon nanoelectromechanical systems.* Journal of Applied Physics, 2004. **95**(5): p. 2682-2689.
266. Woinowski-Krieger, S., *The effect of axial force on the vibration of hinged bars.* J. Appl. Mech., 1950(17): p. 35-36.
267. Burek, M.J., et al., *Nanomechanical resonant structures in single-crystal diamond.* Applied Physics Letters, 2013. **103**(13): p. 131904.
268. Garcia-Sanchez, D., et al., *Imaging Mechanical Vibrations in Suspended Graphene Sheets.* Nano Letters, 2008. **8**(5): p. 1399-1403.
269. Grbic, A. and G.V. Eleftheriades, *Overcoming the Diffraction Limit with a Planar Left-Handed Transmission-Line Lens.* Physical Review Letters, 2004. **92**(11): p. 117403.
270. Liu, Z., et al., *Far-Field Optical Hyperlens Magnifying Sub-Diffraction-Limited Objects.* Science, 2007. **315**(5819): p. 1686-1686.
271. Li, J., et al., *Experimental demonstration of an acoustic magnifying hyperlens.* Nat Mater, 2009. **8**(12): p. 931-934.

272. Kaina, N., et al., *Negative refractive index and acoustic superlens from multiple scattering in single negative metamaterials.* Nature, 2015. **525**(7567): p. 77-81.
273. Silva, A., et al., *Performing Mathematical Operations with Metamaterials.* Science, 2014. **343**(6167): p. 160-163.
274. Bückmann, T., et al., *An elasto-mechanical unfeelability cloak made of pentamode metamaterials.* Nature Communications, 2014. **5**: p. 4130.
275. Reis, P.M., H.M. Jaeger, and M. van Hecke, *Designer Matter: A perspective.* Extreme Mechanics Letters, 2015. **5**: p. 25-29.
276. Coulais, C., et al., *Combinatorial design of textured mechanical metamaterials.* Nature, 2016. **535**(7613): p. 529-532.
277. Kalinin, S.V., B.G. Sumpter, and R.K. Archibald, *Big-deep-smart data in imaging for guiding materials design.* Nat Mater, 2015. **14**(10): p. 973-980.
278. Sun, Y., et al., *Experimental realization of optical lumped nanocircuits at infrared wavelengths.* Nat Mater, 2012. **11**(3): p. 208-212.
279. Li, Y., et al., *Waveguide metatronics: Lumped circuitry based on structural dispersion.* Science Advances, 2016. **2**(6).
280. McHugh, S., *Topological Insulator Realized with Piezoelectric Resonators.* Physical Review Applied, 2016. **6**(1): p. 014008.
281. Schrieffer, J.R. and P.A. Wolff, *Relation between the Anderson and Kondo Hamiltonians.* Physical Review, 1966. **149**(2): p. 491-492.
282. Bampton, M.C. and J. CRAIG, Roy R, *Coupling of substructures for dynamic analyses.* AIAA J., 1968. **6**(7): p. 1313-1319.
283. Hussein, M.I., *Reduced Bloch mode expansion for periodic media band structure calculations.* Proceedings of the Royal Society A: Mathematical, Physical and Engineering Science, 2009. **465**(2109): p. 2825-2848.
284. Krattiger, D. and M.I. Hussein, *Bloch mode synthesis: Ultrafast methodology for elastic band-structure calculations.* Physical Review E, 2014. **90**(6): p. 063306.
285. Palermo, A. and A. Marzani, *Extended bloch mode synthesis: Ultrafast method for the computation of complex band structures in phononic media.* International Journal of Solids and Structures, 2016. **100–101**: p. 29-40.
286. Jensen, J.S., *Phononic band gaps and vibrations in one- and two-dimensional mass–spring structures.* Journal of Sound and Vibration, 2003. **266**(5): p. 1053-1078.
287. Zhou, X., X. Liu, and G. Hu, *Elastic metamaterials with local resonances: an overview.* Theoretical and Applied Mechanics Letters, 2012. **2**(4): p. Article 041001.
288. Huang, H.H. and C.T. Sun, *Wave attenuation mechanism in an acoustic metamaterial with negative effective mass density.* New Journal of Physics, 2009. **11**(1): p. 013003.
289. Winkler, R., et al., *Spin-Orbit Coupling in Two-Dimensional Electron and Hole Systems*. Vol. 41. 2003: Springer.
290. Wagner, M., *Unitary transformations in solid state physics.* 1986.
291. Mukherjee, S., et al., *Observation of a Localized Flat-Band State in a Photonic Lieb Lattice.* Physical Review Letters, 2015. **114**(24): p. 245504.
292. Vicencio, R.A., et al., *Observation of Localized States in Lieb Photonic Lattices.* Physical Review Letters, 2015. **114**(24): p. 245503.
293. Haldane, F.D.M., *Model for a Quantum Hall Effect without Landau Levels: Condensed-Matter Realization of the "Parity Anomaly".* Physical Review Letters, 1988. **61**(18): p. 2015-2018.

294. Hasan, M.Z. and C.L. Kane, *Colloquium.* Reviews of Modern Physics, 2010. **82**(4): p. 3045-3067.
295. Qi, X.-L. and S.-C. Zhang, *Topological insulators and superconductors.* Reviews of Modern Physics, 2011. **83**(4): p. 1057-1110.
296. Nash, L.M., et al., *Topological mechanics of gyroscopic metamaterials.* Proceedings of the National Academy of Sciences, 2015. **112**(47): p. 14495-14500.
297. Wang, P., L. Lu, and K. Bertoldi, *Topological Phononic Crystals with One-Way Elastic Edge Waves.* Physical Review Letters, 2015. **115**(10): p. 104302.
298. Fleury, R., et al., *Sound Isolation and Giant Linear Nonreciprocity in a Compact Acoustic Circulator.* Science, 2014. **343**(6170): p. 516-519.
299. Khanikaev, A.B., et al., *Topologically robust sound propagation in an angular-momentum-biased graphene-like resonator lattice.* Nature Communications, 2015. **6**: p. 8260.
300. Pal, R.K., M. Schaeffer, and M. Ruzzene, *Helical edge states and topological phase transitions in phononic systems using bi-layered lattices.* Journal of Applied Physics, 2016. **119**(8): p. 084305.
301. Lin, Z., et al., *Enhanced Spontaneous Emission at Third-Order Dirac Exceptional Points in Inverse-Designed Photonic Crystals.* Physical Review Letters, 2016. **117**(10): p. 107402.
302. Petyt, M., *Introduction to finite element vibration analysis*. 2010: Cambridge university press.

Appendix 1: Code for stochastic simulation

```
#include <iostream>
#include <fstream>
#include <cstdlib>
#include <cmath>
#include <random>
#include <chrono>

#define NUM_VARS 14
#define integration_type double
#define SQRT3INV 0.57735026919
#define PI 3.14159265359
#define K_BOLTZMANN (1.3806488e-23)

// Butcher tableau
const integration_type srkC0[4] = { 0, 1, 0.5, 0 };
const integration_type srkC1[4] = { 0, 0.25, 1.0, 0.25 };
const integration_type srkAlpha[4] = { 1.0/6, 1.0/6, 2.0/3.0, 0 };
const integration_type srkBeta1[4] = { -1, 4.0/3.0, 2.0/3.0, 0 };
const integration_type srkBeta2[4] = { 1, -4.0/3.0, 1.0/3.0, 0 };
const integration_type srkBeta3[4] = { 2.0, -4.0/3.0, -2.0/3.0, 0 };
const integration_type srkBeta4[4] = { -2, 5.0/3.0, -2.0/3.0, 1.0 };
const integration_type srkA0[4][4] = { {0,0,0,0}, {1.0, 0, 0, 0}, {0.25, 0.25, 0, 0},
{0, 0, 0, 0} };
const integration_type srkA1[4][4] = { {0,0,0,0}, {0.25, 0, 0, 0}, {1.0, 0, 0, 0}, {0,
0, 0.25, 0} };
const integration_type srkB0[4][4] = { {0,0,0,0}, {0, 0, 0, 0}, {1.0, 0.5, 0, 0}, {0, 0,
0, 0} };
const integration_type srkB1[4][4] = { {0,0,0,0}, {-0.5, 0, 0, 0}, {1.0, 0, 0, 0}, {2.0,
-1.0, 0.5, 0} };

// Factors to interpolate gaussian cumulative distribution
#define BSM_A0 2.50662823884
#define BSM_A1 -18.61500062529
#define BSM_A2 41.39119773534
#define BSM_A3 -25.44106049637

#define BSM_B0 -8.47351093090
#define BSM_B1 23.08336743743
#define BSM_B2 -21.06224101826
#define BSM_B3 3.13082909833

#define BSM_C0 0.3374754822726147
#define BSM_C1 0.9761690190917186
#define BSM_C2 0.1607979714918209
#define BSM_C3 0.0276438810333863
#define BSM_C4 0.0038405729373609
#define BSM_C5 0.0003951896511919
#define BSM_C6 0.0000321767881768
#define BSM_C7 0.0000002888167364
#define BSM_C8 0.0000003960315187


// Variables for runge-kutta
integration_type y[NUM_VARS];
integration_type h0[4][NUM_VARS];
integration_type h1[4][NUM_VARS];
integration_type noiseVariables;
integration_type noiseDerivatives;

//Result caching
integration_type evaluatedDerivatives[4][NUM_VARS];
integration_type evaluatedNoise[4][NUM_VARS];
integration_type driveTermIk[NUM_VARS];
integration_type driveTermIk0[NUM_VARS];
integration_type driveTermIkk[NUM_VARS];
integration_type driveTermIkkk[NUM_VARS];
```

```
integration_type diffStage[NUM_VARS];

const bool stochasticMask[NUM_VARS] = {false, true, false, true, false, true, false,
false, false, false, false, false, false, false};

integration_type t;
integration_type h;
integration_type sqH;
integration_type invH;
integration_type invSqH;

unsigned seed = std::chrono::system_clock::now().time_since_epoch().count();
std::mt19937* generator;
std::mt19937* generator2;

// System specific section 1 starts here:
integration_type fh, fc, fw;
integration_type mh, mc, mw; // Effective masses
integration_type qh, qc, qw;
integration_type kh, kc, kw; // Effective stiffness
integration_type bh, bc, bw; // Dampings
integration_type th, tc, tw; // Noise temperatures
integration_type nh, nc, nw; // Noise multiplicative factors
integration_type mu, lambda, khc; // Nonlinear term, nonlinear coupling and linear
coupling
integration_type filterInvTau;

integration_type cosWork, sinWork;

integration_type excitationAmplitude;

// This function needs to be parameterized for sweeping
void setDefaultParameters(double sweepParam) {
    double factor = 0.8125;
    //excitationAmplitude = (1e-6)*sweepParam;
    mh = 0.000275406*factor;
    mc = 0.000275406*factor;
    mw = 1.27;

    qh = 59.41;
    qc = 167.78;
    qw = 960;

    fh = 165.3692*1.154;
    fc = 165.3692;
    fw = 26.87;

    th = 2.0e18;
    tc = th*0;
    tw = sweepParam*th;

    kh = mh*(2.0*PI*fh)*(2.0*PI*fh);
    kc = mc*(2.0*PI*fc)*(2.0*PI*fc);
    kw = mw*(2.0*PI*fw)*(2.0*PI*fw);

    bh = mh*2.0*PI*fh/qh;
    bc = mc*2.0*PI*fc/qc;
    bw = mw*2.0*PI*fw/qw;

    nh = sqrt(2.0*th*K_BOLTZMANN*bh)/mh;
    nc = sqrt(2.0*tc*K_BOLTZMANN*bc)/mc;
    nw = sqrt(2.0*tw*K_BOLTZMANN*bw)/mw;

    khc = 0.0381*kc;
    filterInvTau = 1.0/5000;

    lambda = factor*(631.45e3);
    mu = factor*20.8e6;
}
```

```
inline void updateNonautonomousTerms(double ct) {
    sinWork = (excitationAmplitude)*sin(2.0*PI*fw*ct);
    cosWork = (excitationAmplitude)*cos(2.0*PI*fw*ct);
}

inline void fourthOrderLowPass(integration_type *variables, integration_type*
derivatives, integration_type value, int offset, integration_type invTau) {
    derivatives[offset] = (value-variables[offset])*invTau;
    derivatives[offset+1] = (variables[offset]-variables[offset+1])*invTau;
    derivatives[offset+2] = (variables[offset+1]-variables[offset+2])*invTau;
    derivatives[offset+3] = (variables[offset+2]-variables[offset+3])*invTau;
}

inline void derivatives(integration_type *variables, integration_type* derivatives,
double t) {
   // updateNonautonomousTerms(t);
    derivatives[0] = variables[1];
    derivatives[1] = (-kh*variables[0]-bh*variables[1]-
mu*((variables[0])*(variables[0])*(variables[0]))+khc*(variables[2]-variables[0]))/mh;

    derivatives[2] = variables[3];
    derivatives[3] = (-(kc+2.0*lambda*variables[4])*variables[2]-
mu*((variables[2])*(variables[2])*(variables[2]))-bc*variables[3]+khc*(variables[0]-
variables[2]))/mc;
    //derivatives[3] = (-(kc+2.0*lambda*cosWork)*variables[2]-bc*variables[3]-
mu*((variables[2])*(variables[2])*(variables[2]))+khc*(variables[0]-variables[2]))/mc;

    derivatives[4] = variables[5];
    derivatives[5] = (-kw*variables[4]-bw*variables[5]-
lambda*((variables[2])*(variables[2])))/mw;

    fourthOrderLowPass(variables, derivatives, variables[3]*khc*(variables[0]-
variables[2]), 6, filterInvTau);
    fourthOrderLowPass(variables, derivatives,
variables[5]*lambda*((variables[2])*(variables[2])), 10, filterInvTau);
}

inline void noiseFunction(integration_type *variables, integration_type* derivatives,
double t) {
    derivatives[0] = 0;
    derivatives[1] = nh;
    derivatives[2] = 0;
    derivatives[3] = nc;
    derivatives[4] = 0;
    derivatives[5] = nw;
    derivatives[6] = 0;
    derivatives[7] = 0;
    derivatives[8] = 0;
    derivatives[9] = 0;
    derivatives[10] = 0;
    derivatives[11] = 0;
    derivatives[12] = 0;
    derivatives[13] = 0;
}

// System specific section 1 ends here

void setH(integration_type newH) {
    h = newH;
    sqH = sqrt(newH);
    invH = 1.0/newH;
    invSqH = 1.0/sqH;
}

//
bool whichGenerator;
inline integration_type getUniformRandomNumber01() {
    int64_t a,b;
    if(true) {
```

```
        a = (*generator)();
        b = (*generator).max();
    } else {
        a = (*generator2)();
        b = (*generator2).max();
    }
    return ((integration_type)a)/((integration_type)b);
}

// Generates gaussian distributed number pair with zero mean and variance h N(0,H)
inline void boxMuller(integration_type *_firstNumber, integration_type *_secondNumber) {
    integration_type firstNumber;
    integration_type secondNumber;
    firstNumber = getUniformRandomNumber01();
    if(firstNumber < 1e-9) firstNumber = 1e-9;
    firstNumber = -2.0 * log(firstNumber);
    secondNumber = getUniformRandomNumber01() * (2.0*PI);
    firstNumber = sqrt(h*firstNumber);
    *_firstNumber = firstNumber*cos(secondNumber);
    *_secondNumber = firstNumber*sin(secondNumber);
}

integration_type beasleySpringerMoro(integration_type _vl = -1) {
       if(_vl < 0)
              _vl = getUniformRandomNumber01();
       if(_vl < 0.5) return -beasleySpringerMoro(1.0-_vl);
       if(_vl <= 0.92) {
              integration_type v2 = _vl-0.5;
              integration_type v22 = v2*v2;

       return  sqH*v2*(BSM_A0+v22*(BSM_A1+v22*(BSM_A2+v22*BSM_A3)))/(1+v22*(BSM_B0+v22*(
BSM_B1+v22*(BSM_B2+v22*BSM_B3))));
       }
       if(_vl > 0.999999999) _vl = 0.999999999;
       integration_type vx = log(-log(1.0-_vl));
       return sqH*(BSM_C0 +
vx*(BSM_C1+vx*(BSM_C2+vx*(BSM_C3+vx*(BSM_C4+vx*(BSM_C5+vx*(BSM_C6+vx*(BSM_C7+BSM_C8*vx))
))))));
}

void generateRandomValues() {
    integration_type firstNumber, secondNumber, zeroTerm;
    //boxMuller(&zeroTerm, &secondNumber);
    zeroTerm = beasleySpringerMoro();
    whichGenerator = false;
    for(int i=0;i<NUM_VARS;i++) {
        if(stochasticMask[i]) {
            //boxMuller(&firstNumber, &secondNumber);
           firstNumber = beasleySpringerMoro();
           secondNumber = beasleySpringerMoro();
            driveTermIk[i] = firstNumber;
            driveTermIk0[i] = 0.5*h*(firstNumber+SQRT3INV*secondNumber);
            driveTermIkk[i] = 0.5*(firstNumber*firstNumber-h);
            driveTermIkkk[i] = (1.0/6.0)*(firstNumber*firstNumber*firstNumber-
3.0*zeroTerm*firstNumber);
            whichGenerator = !whichGenerator;
        }
    }
}

void zeroVariables() {
    for(int i=0;i<NUM_VARS;i++) {
        driveTermIk[i] = 0;
        driveTermIk0[i] = 0;
        driveTermIkk[i] = 0;
        driveTermIkkk[i] = 0;
        y[i]=0;
    }
}
```

```
void stochasticRungeKuttaStep() {
    generateRandomValues();
    for(int i=0;i<NUM_VARS;i++) {
        h0[0][i] = y[i]; h1[0][i] = y[i];
        h0[1][i] = y[i]; h1[1][i] = y[i];
        h0[2][i] = y[i]; h1[2][i] = y[i];
        h0[3][i] = y[i]; h1[3][i] = y[i];
    }
    for(int i=0;i<4;i++) {
        for(int j=0;j<i;j++) {
            for(int k=0;k<NUM_VARS;k++) {
                h0[i][k] += srkA0[i][j]*evaluatedDerivatives[j][k]*h +
srkB0[i][j]*evaluatedNoise[j][k]*driveTermIk0[k]*invH;
                h1[i][k] += srkA1[i][j]*evaluatedDerivatives[j][k]*h +
srkB1[i][j]*evaluatedNoise[j][k]*sqH;
            }
        }
        derivatives(h0[i],evaluatedDerivatives[i],t+srkC0[i]*h);
        noiseFunction(h1[i],evaluatedNoise[i],t+srkC1[i]*h);
    }
    for(int i=0;i<NUM_VARS;i++) diffStage[i]=0;
    for(int i=0;i<4;i++) {
        for(int k=0;k<NUM_VARS;k++) {
            diffStage[k] += srkAlpha[i]*evaluatedDerivatives[i][k]*h;
            diffStage[k] +=
(srkBeta1[i]*driveTermIk[k]+srkBeta2[i]*driveTermIkk[k]*invSqH+srkBeta3[i]*driveTermIk0[
k]*invH+srkBeta4[i]*driveTermIkkk[k]*invH)*evaluatedNoise[i][k];
        }
    }
    for(int i=0;i<NUM_VARS;i++) y[i] += diffStage[i];
    t += h;
}

void performIntegration(integration_type newH, int64_t num_steps)
{
    setH(newH);
    for(int64_t i=0;i<num_steps;i++) {
        stochasticRungeKuttaStep();
    }
}

double get_sweep_var()
{
       std::ifstream rd; rd.open("sweepvar",std::ios_base::binary);
       rd.seekg(0,std::ios::beg);
       double a;
       void *b = &a;
       rd.read((char*)b,8);
       rd.close();
       return a;
}

int main(void) {
    unsigned seed = std::chrono::system_clock::now().time_since_epoch().count();
    generator2 = new std::mt19937(seed+8913432);
    generator = new std::mt19937(seed);
    integration_type kineticEnergy = 0;
    integration_type potentialEnergy = 0;
    integration_type n = 0;
    integration_type sigma_T=0;
    integration_type sigma_V=0;
    std::ofstream frequencySweep("results_0.txt");
    zeroVariables();
    y[4] = 35e-5;
    integration_type currentSweep = get_sweep_var();
    setDefaultParameters(currentSweep);
    performIntegration(5e-6,((int64_t)130*1000*5*10*10*2)*((int64_t)2*2*2*2*10));
    frequencySweep << currentSweep << '\t' << y[9] << '\t' << y[13] << '\t' <<
y[13]/y[9] << '\n';
    frequencySweep.close();
```

```
    std::cout << "RMS amplitude TH: " << sqrt(y[9]) << '\n';
    std::cout << "Power transfer: " << y[13] << '\n';
    return 0;
}
```

Appendix 2: Images of the experimental setups

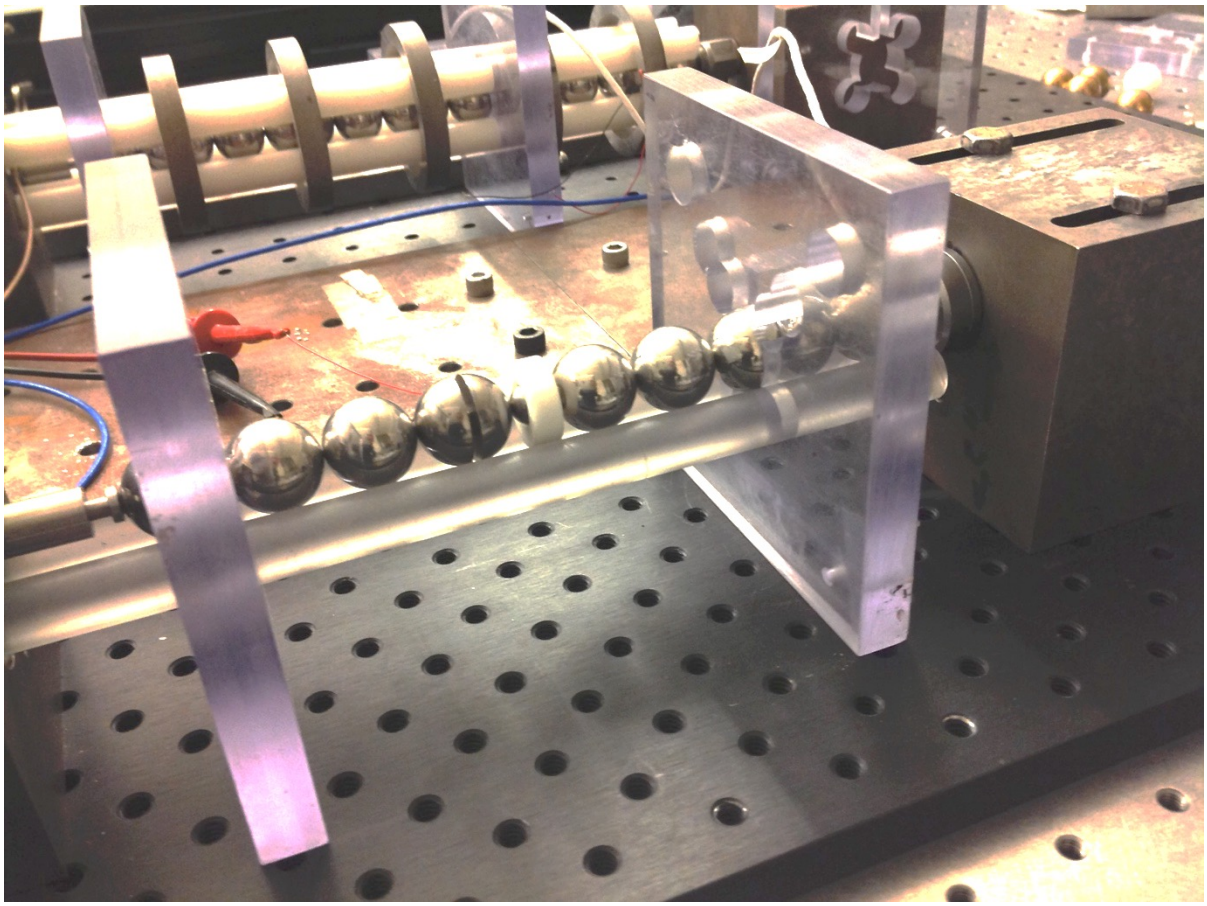

FIG A2.1: *Granular chain utilized in early experiments demonstrating the extreme stiffness tunability phenomenon discussed in Chapter 2.* On the left, a piezoelectric actuator compresses the chain, while on the right, a strain gauge measures the chain's force response. Here, the defect is driven by a split-bead actuator that proved to be unstable against buckling.

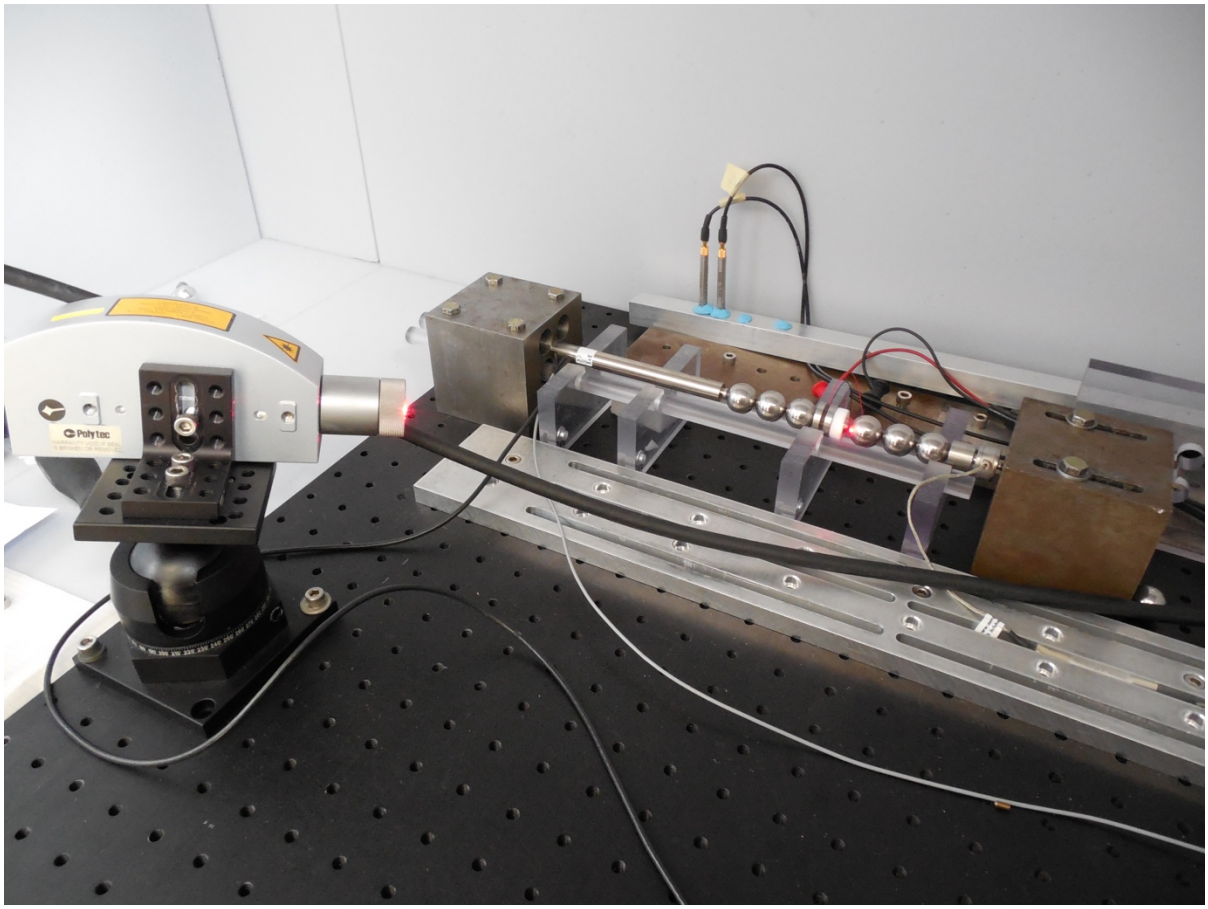

FIG A2.2: *Granular chain measured in the stiffness tunability experiments reported in Chapter 2.* This final setup differs from Fig. A2.1 in the use of a cylindrical actuator instead of a split bead, which improves the chain stability against buckling. Also, this setup includes a Polytec Laser Doppler Vibrometer allowing the simultaneous measurement of the defect's vibration.

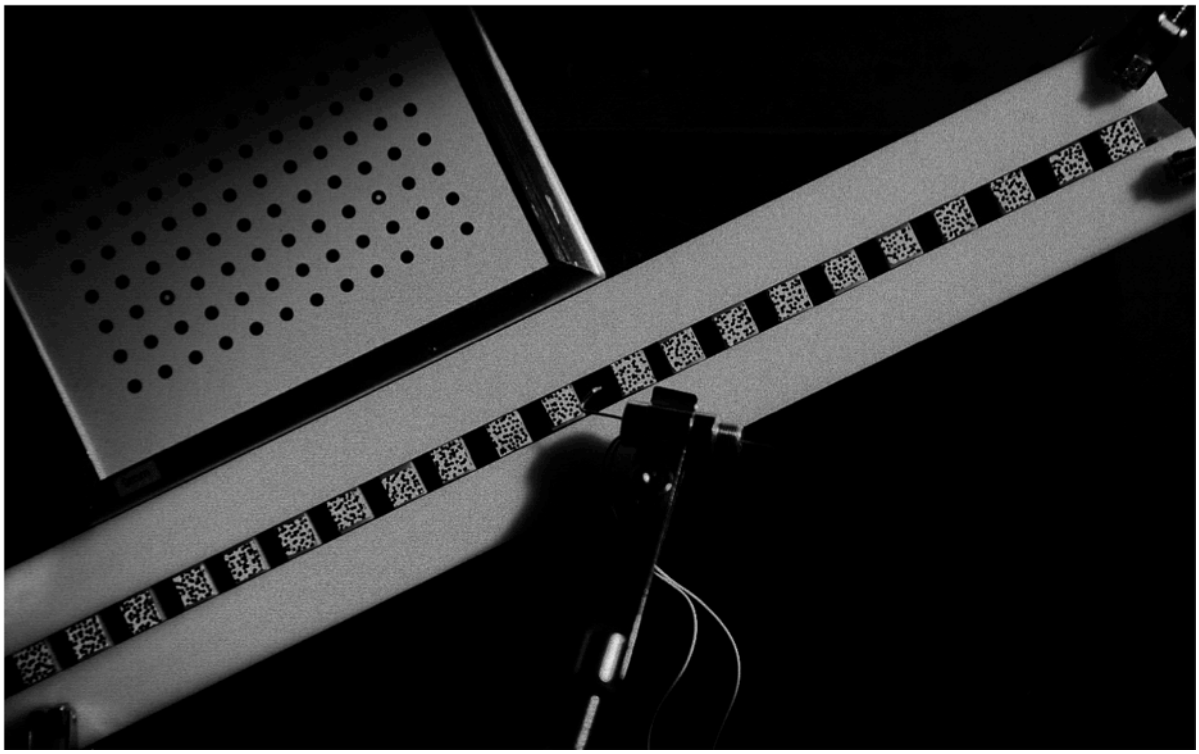

FIG A2.3: *Magnet chain demonstrating synchronized frequency conversion as reported in Chapter 3.* The image shows a chain of magnetic particles constrained between two polymer rods. Each particle has a visible speckle pattern that facilitates its tracking by digital image correlation. The central particle is driven by an electromagnetic actuator. This image was obtained with the same computer vision camera utilized to track the displacements of the particles.

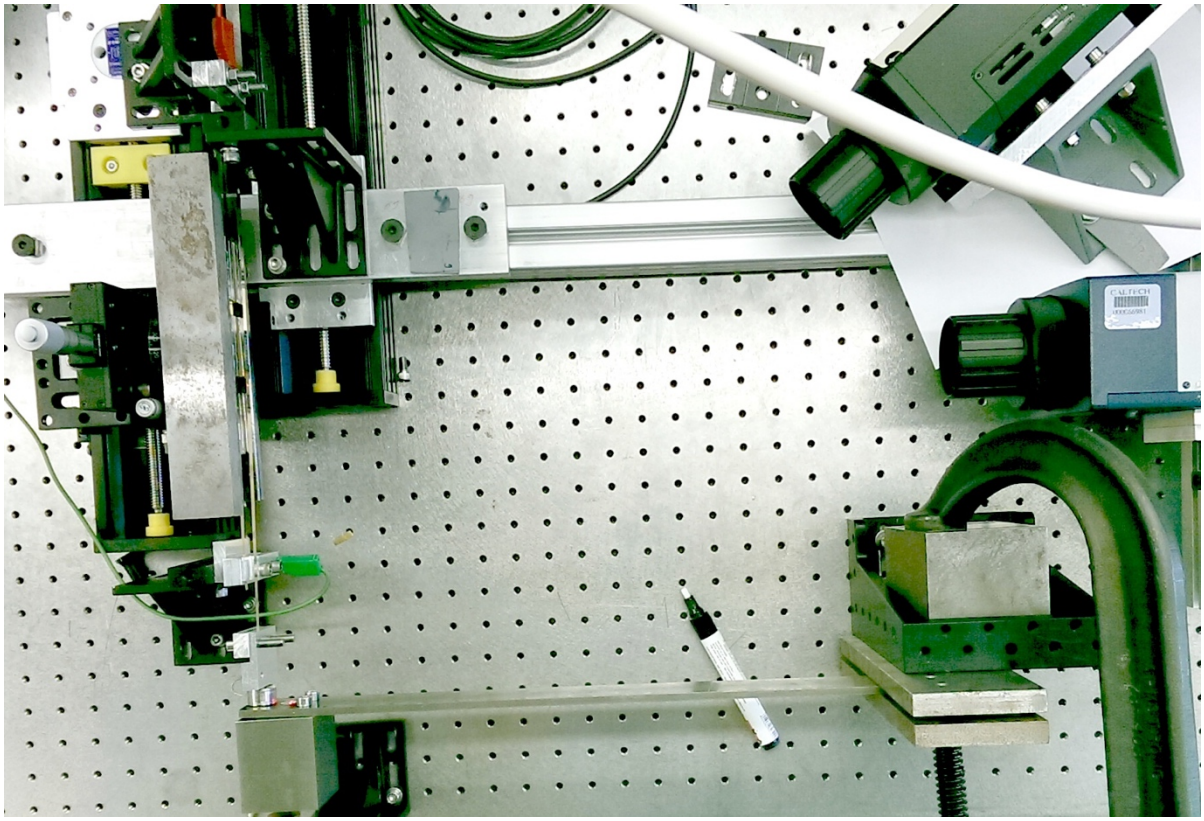

FIG A2.4: *Mechanical autonomous stochastic heat engine.* The left of the image contains the two ribbons that are subject to simulated thermal baths at different temperatures. The bottom shows the cantilever that acts as output of the engine, while the top-right corner contains the two Polytec Laser Doppler Vibrometers utilized to monitor the ribbon and cantilever motions during thermal engine operation.